Physics Potential and Feasibility of UNO

June 2001

UNO Proto-collaboration

UNO Theoretical Advisory Committee

and

Other Contributors and Interested Observers

Front Cover: The expected ratio of the observed atmospheric neutrino induced muon rate in UNO to the non-oscillation expectation as a function of L/E (upper right). Three displays of a $p \rightarrow e^+\pi^0$ event simulated in UNO assuming 40% photocathode. The event is displayed using an exploded view of a cubical module(center), displayed using a Mercator projection (lower right), and transformed on to a unit sphere (upper left).

Back Cover: An image of the remnant of Supernova 1987A as seen by the Hubble Space Telescope (upper right). An image of the sun as seen in solar neutrinos using the Super-Kamiokande detector (lower left), and the sensitivity region of UNO for $\sin^2\theta_{13}$ using a low energy muon neutrino beam.

The editors
(D. Casper, C.K. Jung, C. McGrew and C. Yanagisawa)
would like to present this work in honor of our friend and colleague
Maurice Goldhaber,
on the occasion of his 90^{th} birthday.

The UNO Proto-collaboration

ANL, Argonne, Illinois, U.S.A.
Maury Goodman

BNL, Upton, New York, U.S.A.
M. Goldhaber, M. Diwan, R. Hahn, B. Viren

University of California, Davis, Davis, California, U.S.A.
D. Ferenc

University of California, Irvine, Irvine, California, U.S.A.
S. Barwick, D. Casper, W. Gajewski, W. R. Kropp, S. Mine, M. Smy, H. Sobel, M. R. Vagins, G. Yodh

GRPHE/UHA, Mulhouse, France
Y. Benhammou

Indiana University, Bloomington, Indianna, U.S.A.
R. Van Kooten

University of Kansas, Lawrence, Kansas, U.S.A.
P. Baringer, D. Besson

LANL, Los Alamos, New Mexico, U.S.A.
T. J. Haines

Louisiana State University, Baton Rouge, Louisiana, U.S.A.
R. C. Svoboda

University of Minnesota, Duluth, Minnesota, U.S.A.
A. Habig

University of Minnesota, Minneapolis, Minnesota, U.S.A.
M. Marshak, J. Nelson, E. Peterson

University of Nebraska, Lincoln, Nebraska, U.S.A.
D. Claes

National High Magnetic Field Laboratory, Tallahassee, Florida, U.S.A.
J. Miller

University of New Mexico, Albuquerque, New Mexico, U.S.A.
S. Seidel

Northwestern University, Evanston, Illionois, U.S.A.
H. Schellman

State University of New York at Stony Brook, Stony Brook, New York, U.S.A.
M. Ackerman, J. Hill, C. K. Jung, T. Kato, R. McCarthy, C. McGrew, M. Rijssenbeek, C. Yanagisawa

University of Rochester, Rochester, New York, U.S.A.
A. Bodek, K. McFarland

Institute de Récherches Subatomiques/ULP, Strasbourg, France
C. Racca, J. M. Brom

Tufts University, Medford, Massachusetts, U.S.A.
T. Kafka, T. Mann

University of Utah, Salt Lake City, Utah, U.S.A.
K. Martens

Warsaw University, Warsaw, Poland
D. Kielczewska

University of Washington, Seattle, Washington, U.S.A.
J. Wilkes

Waste Isolation Pilot Plant, Carlsbad, New Mexico, U.S.A.
R. Nelson, W. Thompson

The UNO Theoretical Advisory Committee

University of Arizona, Tuscon, Arizona, U.S.A.
A. Burrows

BNL, Upton, New York, U.S.A.
W. Marciano

FNAL, Batavia, Illinois, U.S.A.
J. Beacom

Institute for Advanced Study, Princeton, New Jersey, U.S.A.
J.N. Bahcall

University of Maryland, College Park, Maryland, U.S.A.
J. Pati

Massachusetts Institute of Technology, Cambridge, Massachusetts, U.S.A.
F. Wilczek

State University of New York at Stony Brook, Stony Brook, New York, U.S.A.
J. Lattimer, R. Shrock

Other Contributors and Interested Observers

Boston University, Boston, Massachusetts, U.S.A.
E. Kearns, L. R. Sulak, C. W. Walter

BNL, Upton, New York, U.S.A.
J. C. Gallardo

CEA/Saclay, Gif-sur-Yvette Cedex, France
M. Spiro

CERN, Geneva, Switzerland
P. Hernández

FNAL, Batavia, Illinois, U.S.A.
F. DeJongh, S. Geer, D. Harris, J. Yu

Université de Genève, Geneva, Switzerland
A. Blondel

ICRR, University of Tokyo, Tokyo, Japan
T. Kajita, M. Shiozawa, Y. Suzuki

IHEP, Beijing, P.R. China
Y. Wang

INFN, Napoli, Italy
V. Palladino

INFN, Padova, Italy
M. Mezzetto

KEK, Tsukuba, Japan
K. Nakamura

Kyoto University, Kyoto, Japan
T. Nakaya, K. Nishikawa

LBL, Berkeley, California, U.S.A.
A. M. Sessler

Louisiana State University, Baton Rouge, Louisiana, U.S.A.
W. Metcalf

Massachusetts Institute of Technology, Cambridge, Massachusetts, U.S.A.
K. Scholberg

University of Michigan, Ann Arbor, Michigan, U.S.A.
K. Riles

State University of New York at Stony Brook, Stony Brook, New York, U.S.A.
I. Mocioiu, R. A.M.J. Wijers

University of Pennsylvania, Philadelphia, Pennsylvania, U.S.A.
K. Lande

Pacific Northwest National Laboratory, Richland, Washington, U.S.A.
R. T. Kouzes

Queen's University, Kingston, Ontario, Canada
M.C. Chen

SNO Institute, Canada
Canadian SNO Collaboration

Universidad de Valencia, Valencia, Spain
J. Burguet-Castell, J.J. Gomez-Cádenas

Contents

Chapter 1

Introduction

Over the past two decades, large underground water Cherenkov experiments — Super-Kamiokande and its predecessors IMB and Kamiokande — have established a remarkable record of success. Their more notable accomplishments include:

- Exclusion of the minimal SU(5) Grand Unified Theory (GUT),
- First real time, directional measurement of solar neutrinos,
- Confirmation of the solar neutrino flux deficit,
- Discovery of atmospheric neutrino oscillation and neutrino mass,
- First detection of accelerator-produced neutrinos at ∼100 km baseline,
- Observation of neutrinos from Supernova 1987A, and
- Establishment of the world's best limits on nucleon decay.

Although originally designed to search for nucleon decay, the above resumé highlights the versatility of these detectors. While, as yet, no unambiguous nucleon decay signal has been identified, the evidence for neutrino oscillation (now firmly established by Super-Kamiokande's atmospheric neutrino data) represents a watershed in particle physics [1]. This breakthrough demonstrates that neutrino masses are very small indeed (if we assume no degeneracy in mass eigenstates), which in turn strongly suggests a new, very high-energy mass scale which generates these small neutrino masses via the "See-saw" mechanism [2].

Many theoretical models predict nucleon decay, which is a generic consequence of most GUT models. A specific example of such models can be found in Refs. [3, 4, 5, 6], which lay out in detail the connections between neutrino masses, nucleon decay and other Standard Model observables in the G(2,2,4) and SO(10) frameworks. This model predicts proton decay rates within reach of Super-Kamiokande, especially in SUSY-favored decay modes such as $p \to \overline{\nu} K^+$. These predictions, along with those of other models, encourage us to extend the search for nucleon decay to even greater sensitivity.

The motivation for redoubled effort in the search for nucleon decay has recently been strengthened by theoretical and experimental advances in other domains, namely:

- an improved calculation of the hadronic nucleon decay matrix element, β_H, based on lattice QCD,
- a smaller value of the strong coupling constant $\alpha_s(m_Z)$ inferred from LEP data, which consequently lowers the unification scale, and
- a larger value of the ratio of Higgs vacuum expectation values $\tan\beta$ in SUSY models, suggested by both LEP data and recent measurements of the muon anomalous magnetic moment, $g-2$.

All of these factors increase the expected rate of nucleon decay with respect to earlier predictions, making its detection appear to be an attainable goal.

Discovery of nucleon decay would provide direct evidence that a simpler, yet more fundamental, description of physics lies hidden within the Standard Model. The centuries-old notion of "unification" in physics, that is, reduction of apparently unrelated phenomena to more general laws, traces its origin from Newton's discovery of a single, universal law which could account for both terrestrial gravitation and celestial mechanics. It reappeared in Maxwell's formulation of electromagnetism, and later in the Glashow-Weinberg-Salaam electroweak theory which, together with QCD, forms the basis of today's Standard Model of particle physics. For two decades, nucleon decay has been the crucible in which attempts at still greater (or "grand") unification are tested; to date, none have proven equal to the challenge. Observation of nucleon decay would be far more than a mere "existence proof" for a Grand Unified Theory—it would give us direct experimental clues about precisely *which* theory nature has chosen. In this respect, the search for nucleon decay is the ultimate experiment at the "energy frontier": probing physics at a scale ($\sim 10^{16}$ GeV) far beyond the reach of any imaginable accelerator. In the absence of a signal, five years of UNO data will extend the lifetime limit for two "benchmark" decay modes ($p \to e^+\pi^0$ and $p \to \bar{\nu}K^+$) by roughly an order of magnitude over present Super-Kamiokande limits: to $\sim 5 \times 10^{34}$ yr and $\sim 10^{34}$ yr, respectively. The expected limit for $p \to e^+\pi^0$ reaches 10^{35} yr after a 13-year UNO exposure.

The unrivaled flexibility of the water Cherenkov technique permits us to follow up past breakthroughs even while pursuing new ones: we are fortunate to live in interesting times. In several years, the "discovery" phase of neutrino flavor physics, which was initiated by ground-breaking measurements of solar and atmospheric neutrinos, will be drawing to a close even as the "precision measurement" era is dawning. We may hope that in the interim, the solar neutrino puzzle can be resolved by existing or approved experiments such as Super-Kamiokande, SNO, KamLAND and Borexino, and that the dominant channel of ν_μ oscillation will be well-characterized by long-baseline experiments such as K2K and MINOS. Should the MiniBOONE experiment confirm the puzzling LSND effect, the discovery potential of the neutrino sector will multiply considerably. But regardless, even in the most optimistic scenarios, large gaps will remain in our understanding of the neutrino mass hierarchy and leptonic mixing matrix, and direct observation of the oscillatory nature of neutrino flavor violation and ν_τ appearance may remain elusive.

The sinusoidal pattern expected from neutrino oscillation can be established conclusively by measurements of atmospheric neutrinos in a larger detector. Although Super-Kamiokande's directional and hadronic energy resolution are more than sufficient, that detector's dimensions are too small to efficiently contain muons with energies above a few GeV. A larger detector will remedy this "Achilles Heel"; the resulting gain in L_ν/E_ν resolution, together with a corresponding increase in event rate, will unambiguously establish whether oscillation or some more exotic phenomenon is at work and allow high-precision measurements of the parameters involved.

Probing the subdominant mixing angle θ_{13} and possible CP-violating terms in the leptonic mixing matrix will require a new generation of neutrino sources and detectors. Two possible types of neutrino sources are presently under intensive study: a muon storage ring (or "neutrino factory"), or more conventional ("Super-") beams, both fed by very powerful proton drivers. An extremely massive water Cherenkov detector, sensitive to neutrinos over 6 decades of energy, is well-suited to serve as the distant target for any conceivable future high-intensity neutrino source. With a beam of few hundred MeV from a distance of $\sim$100 km, θ_{13} sensitivity of 10^{-3} is achievable and CP-violating effects can be observed without complication by matter effects in a variety of plausible scenarios. For a high-energy beam from a muon storage ring, with the addition of internal or external magnets, a water detector's sensitivity to wrong-sign muon appearance is comparable to that of proposed iron spectrometers and liquid detectors, while also offering a much broader complementary program of nucleon decay and particle astrophysics measurements.

Neutrinos from stellar collapse provide a window on neutron star and black hole formation, the supernova explosion mechanism, and heavy element production mechanisms at the very heart of a doomed star, but only 20 such neutrinos have been measured. A much larger detector can increase the chance of future observations by extending the range of detection to a much larger population of stars (the Andromeda Galaxy), *and* extract much more precise and detailed information from any burst which does occur in our own galaxy. Millisecond timing structure in the collapse is visible if $\sim$100,000 neutrino interactions are observed. A detector with roughly 20 times the fiducial mass of Super-Kamiokande can collect such a sample from a supernova at the galactic center, and see a clear (if modest) signal even at a distance of 1 Mpc. Such a detector can also search for astrophysical point sources of neutrinos, and dark matter, in an energy range difficult for larger, more coarse-grained undersea and under-ice detectors to cover.

To relentlessly pursue the quest for evidence of grand unification, to unlock the fundamental secrets of neutrino oscillation, and to advance a diverse program of particle astrophysics, we have studied the physics potential and feasibility of a much larger next-generation nucleon decay and neutrino detector. This detector, sited underground and using the robust, versatile and economical water Cherenkov technique, is named UNO (Underground Nucleon decay and Neutrino Observatory) [7].

Preliminary cost estimates indicate the cost of the UNO detector—as described herein with 13 times the total mass of Super-Kamiokande and 20 times the fiducial mass—would be \$500M (including excavation), and we find no significant technical obstacles to construction of such a detector. We expect the detector could be completed within ten years of ground-breaking.

At present, the informal UNO proto-collaboration consists of 48 experimental physicists, representing 23 institutions. The collaboration is supported by a Theoretical Advisory Committee (UNO-TAC) and other interested parties from Canada, China, Europe, Japan, and the United States, numbering about 100 in total.

Parallel to the UNO initiative, the possibility of similar next-generation underground water Cherenkov detectors has been discussed in Japan (Hyper-Kamiokande) and in Europe (Fréjus). Also under study in Japan is a large underwater Cherenkov detector (Titanic). The UNO proto-collaboration views these efforts (including our own) as reinforcing, rather than competing with, each other. Taken together, they demonstrate an even broader endorsement of the physics objectives we aim to address, and a global commitment to the shared goal of constructing a next-generation water detector somewhere in the world. Indeed, many of the physicists involved in these other projects have participated fruitfully in our discussions and made very significant contributions to this document, for which we are most grateful.

If realized, UNO will provide a comprehensive nucleon decay and neutrino physics program to the astrophysics, nuclear physics, and particle physics communities world-wide, for decades to come. In the remainder of this document, we present the conceptual configuration, physics potential, candidate sites, and R&D plans for the UNO detector in greater detail.

1.1 Bibliography

[1] Y. Fukuda *et al.*, Phys. Rev. Lett. **81**, 1562 (1998)

[2] M. Gell-Mann, P. Ramond, R. Slansky, in *Supergravity*, edited by P. van Nieuwenhuizen and D. Freedman (North Holland,Amsterdam, 1979), p.315; T. Yanagida in Proceedings of *Workshop on Unified Theory and Baryon Number in the Universe*, KEK, 1979.

[3] J. Pati and A. Salam, Phys. Rev. Lett. **31**, 661 (1973); Phys. Rev. **D10**, 275 (1974).

[4] C. Albright, K. Babu, and S. Barr, Phys. Rev. Lett. **81**, 1167 (1998) (hep-ph/9802314).

[5] C. Albright and S. Barr, Phys. Rev. Lett. **85**, 244 (2000) (hep-ph/0002155); Phys. Rev. **D62**, 093008 (2000) (hep-ph/0003251); hep-ph/0104294.

[6] K. Babu, J. Pati, and F. Wilczek, Phys. Lett. **B423**, 337 (1998); Nucl. Phys. **566**, 33 (2000) (hep-ph/9812538).

[7] C. K. Jung, Feasibility of a Next Generation Underground Water Cherenkov Detector: UNO, (hep-ex/0005046); Next Generation Nucleon Decay and Neutrino Detector, AIP Conference Proceedings 533, edited by M. V. Diwan and C. K. Jung (2000)

Chapter 2

The UNO Detector

UNO's design philosophy begins with the well-established water Cherenkov detector technology of Super-Kamiokande. Extension of the technique to achieve an order of magnitude better sensitivity to nucleon decay and precision measurements of neutrino properties presents no serious technical challenges. In addition to the proven soundness of the fundamental design, UNO can draw on and further refine the twenty years of experience, expertise and analysis tools accumulated from IMB, Kamioka and Super-Kamiokande.

To strike a balance between increased physics reach and practical considerations of cost, the benchmark fiducial volume of the UNO detector is 20 times that of Super-Kamiokande. We aim for broad physics capabilities and a simple, robust detector configuration.

2.1 Optimization: Criteria and Constraints

Several design options have been considered, keeping in mind two practical constraints on the water Cherenkov technique, namely:

- The water depth is limited by the pressure tolerance of the glass bulb of the PMT ($\sim$8 atm, or roughly 80 meters of water for current $20''$ Hamamatsu PMTs). This can be overcome only by enclosing each PMT in a high-pressure water-tight container, thereby compromising the Cherenkov collection efficiency, or by using new PMTs specially designed for high-pressure applications.

- The maximum dimension of a detector with only surface instrumentation is limited by the finite attenuation length of Cherenkov light in pure water ($\sim$80 m at $\lambda = 400\,\mathrm{nm}$ is in Super-Kamiokande).

2.2 Geometry

Three detector concepts have been studied: Cubical, Toroidal and Multi-Cubical. Excavation costs are relatively insensitive to the shape of the cavity [1], but the choice of geometry is still important:

- The cost of mining the cavity is proportional to the *total* volume of the detector, including a ∼2.5 m veto region outside each face of the inner detector and a further 2 m inside the PMT planes which defines the *fiducial* volume. While these non-fiducial buffer volumes do not contribute directly to our nucleon decay and neutrino rates, experience has shown that they are indispensable for ensuring shielding against entering low energy particles from the surrounding rocks and for background rejection.

- The instrumentation cost (for a fixed photocathode coverage) is proportional to the surface area of the inner detector PMT faces. Equivalently, for a fixed PMT budget, increasing the surface area reduces the amount of information collected for each event, eventually degrading the efficiency for low-energy phenomena and the ability to understand complex higher-energy interactions.

To optimize the detector cost for a fixed fiducial volume (445 kton; ∼20 times Super-Kamiokande), the ratio r_V (fiducial volume/total volume) should be maximized and the ratio r_A (PMT surface area/total volume) should be minimized. These geometrical considerations clearly favor detectors which are large in all dimensions.

To achieve the desired fiducial volume, the Cubical design implies a cavity of $86 \times 86 \times 86\,\mathrm{m}^3$ outer dimensions. While the Cubical detector is close to optimal in terms of r_V and r_A, it runs afoul of the practical constraints. PMTs at the bottom of the detector would be subject to a water pressure of about 9 atmospheres. In addition, the diagonal length of 150 m is almost double the attenuation length in pure water measured by Super-Kamiokande.

The Toroidal design is very inefficient in its use of the excavated volume (r_V). It is not physically possible if the cross-section of the detector is $60 \times 60\,\mathrm{m}^2$. Even with a $50 \times 50\,\mathrm{m}^2$ cross-section the torus would be too tight, making the diameter of the central rock column too small to support the structure. Therefore a Toroidal design requires a small cross-section, making the r_V ratio small and the r_A value large. For example, in a Toroidal design with $40 \times 40\,\mathrm{m}^2$ cross-section, only 60% of the total volume is fiducial, compared to 70% for the Multi-Cubical design option discussed below.

The Multi-Cubical design has outer dimensions of $60 \times 60 \times 180\,\mathrm{m}^3$ and appears to be the optimal geometry consistent with practical constraints. When segmented into three $60 \times 60 \times 60\,\mathrm{m}^3$ cubical subdetector elements, both the maximum water pressure and light travel distance are in acceptable ranges, and the r_V and r_A values are reasonable.

Segmentation naturally increases the cost (by creating 4 additional surfaces to instrument) but provides several significant benefits compared to an open geometry:

- Mitigation of so-called "flasher" (PMT discharge) instrumental backgrounds (which occur in all water Cherenkov detectors) by confining each event in a smaller optical compartment.

- Reduced inefficiency and associated systematics due to light attenuation in water, by limiting the maximum distance a photon can travel before reaching a sensitive detector.

- Ensuring nearly 100% operational live time, which is essential for a supernova watch. Even with exceptional reliability, Super-Kamiokande is limited to about 90% operational efficiency due to detector calibration. With three optically separated compartments, two subdetectors can remain live even while a third is being calibrated.
- Better trigger performance at low energy, not only from reduced attenuation but also since each subdetector can trigger independently with a lower accidental rate.
- If the divisions between subdetectors are rigid (*i.e.,* water-tight), it would be possible to periodically empty and maintain each compartment separately. It requires four months to drain and refill the present Super-Kamiokande tank, which is less than 1/4 of the total volume in a single UNO subdetector. Rigid segmentation would also facilitate possible reconfiguration of the detector in the future, for instance to install a magnetic tracking system for neutrino factory physics. At present, cost to benefit ratio for rigid segmentation is uncertain, and thus this option requires further study.

2.3 Underground vs. Underwater

The possibility of siting a next-generation detector underwater rather than underground has also been considered. One serious disadvantage of underwater deployment is inaccessibility for calibration and service. Experience with Super-Kamiokande indicates that a well-selected and well-maintained underground site provides an ideal working environment, and that regular and routine access to the detector is indispensable. In contrast, reliable calibration and operation of a deep underwater detector is a challenge which has still not been solved, despite investment of countless man-years of R&D. In addition, other services such as water purification, power, and computing would need to be deployed near any such underwater laboratory, perhaps even maintained at sea. In summary, an underwater detector would raise many technical complications which are absent in the time-tested and more accommodating underground configuration raising the specter of indeterminate delays and cost overruns. The next large underground water Cherenkov detector will be a fourth-generation device; the next large underwater Cherenkov detector will be the first.

2.4 Baseline Design

We conclude that a large underground water Cherenkov detector with a Multi-Cubical, segmented configuration is the best choice for UNO. Such a experiment could be operational within 10 years, with assured performance and reliability, and no large-scale R&D required. The baseline conceptual design of the UNO detector is shown in Figure 2.1.

The detector has three compartments, each measuring $60 \times 60 \times 60\,\mathrm{m}^3$, for a total length of 180 m and a total mass of 648 kton. The outer detector region serves as a veto shield of 2.5 m depth, and is instrumented with 14,901 outward-facing 8$''$ PMTs at a density of 0.33 PMTs/m^2. The inner detector regions contain the software-defined fiducial volume,

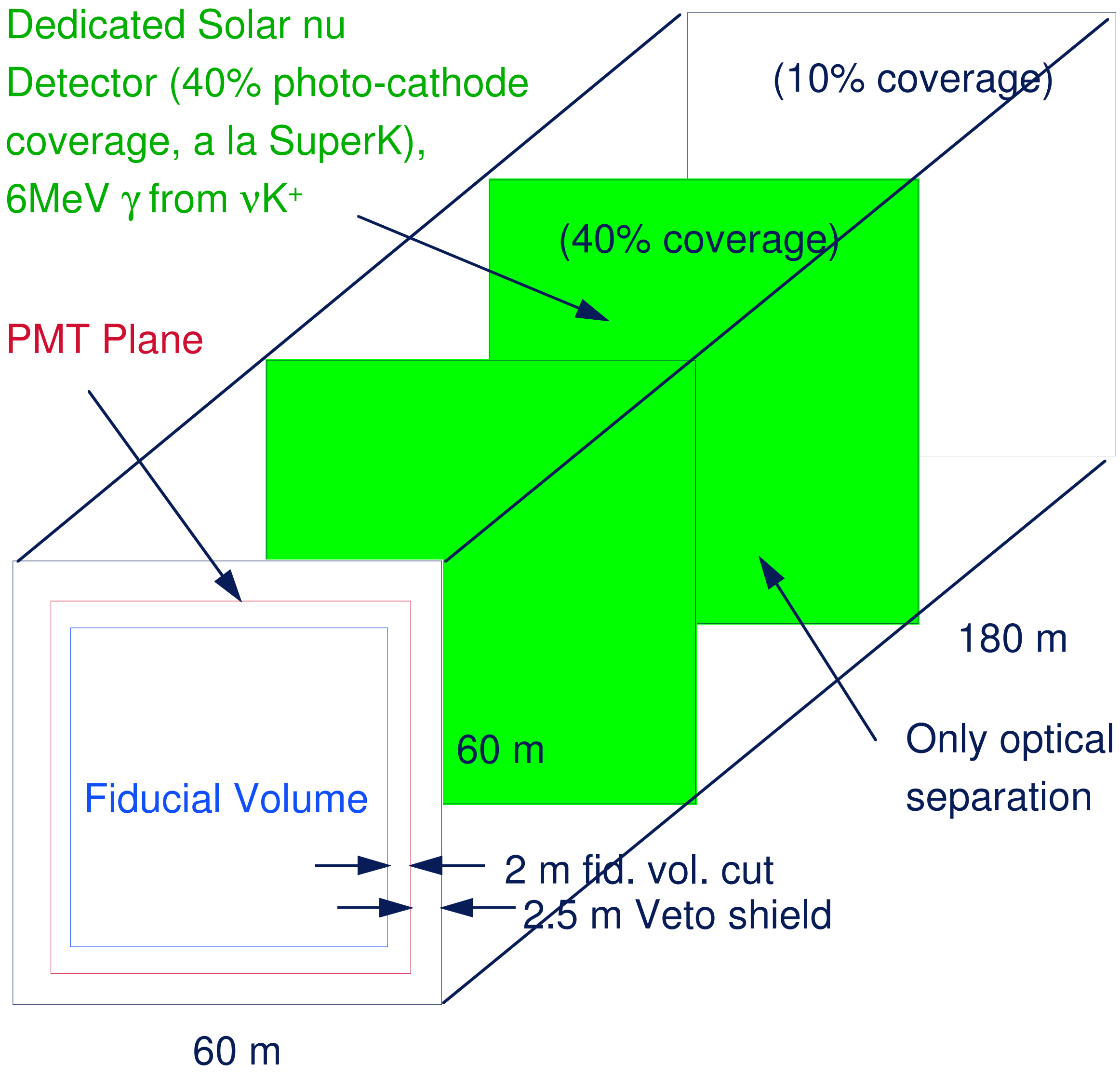

Figure 2.1: Baseline configuration of the UNO detector

beginning 2 m within the PMT planes; the total fiducial mass the three subdetectors is 445 kton. The inner detector regions are viewed by 56,650 20″ PMTs, with an average PMT density of approximately 1 PMT/m^2. Table 2.1 compares UNO's parameters with those of other large water Cherenkov detectors.

Table 2.1: Comparison of water Cherenkov detector parameters.

Parameters	Kamiokande-III	IMB-3	Super-Kamiokande	UNO
Total mass	4.5 kton	8 kton	50 kton	650 kton
Fiducial mass				
proton decay	1.0 kton	3.3 kton	22 kton	440 kton
solar	0.7 kton	–	22 kton	440 kton
supernova	2.1 kton	6.8 kton	32 kton	580 kton
Photocathode coverage	20%	4%	40%	1/3 40% 2/3 10%
Total size	$16m \times 19m\phi$	$22 \times 17 \times 18m^3$	$41m \times 39m\phi$	$60 \times 60 \times 180m^3$

2.5 Light Collection

UNO's PMT density is chosen to allow excellent sensitivity to a broad range of nucleon decay and neutrino physics while keeping the instrumentation costs under control. Even after fixing the average PMT density, however, additional choices are possible.

The PMTs could be deployed uniformly, providing 20% photo-cathode coverage (equivalent to that of Kamiokande-III) over the entire inner detector. The advantages of this scheme are a uniform detector response, excellent ring-identification and particle ID, and roughly 7 MeV analysis threshold through-out the entire 445 kton fiducial volume. Identification of the 6 MeV γ from nuclear de-excitation following $p \to \bar{\nu} K^+$is still possible in this configuration, notwithstanding the nominal 7 MeV threshold, since these events trigger on the higher energy μ^+ from K^+ decay.

Alternatively, the PMT density in the central subdetector module could be doubled to 40% photo-cathode coverage (equivalent to Super-Kamiokande) at the expense of the reducing the two outer modules to 10% each. In this scenario, the trigger threshold for the two wings would be around 10 MeV, while the central detector analysis threshold is reduced to approximately 5 MeV. Only in this configuration is there hope for solar neutrino studies, using the central module. In addition, the lower threshold would allow additional information on core collapse and black-hole formation to be extracted from supernovae neutrinos, along with measurement of the ν_μ and ν_τ fluxes using neutral current excitation of Oxygen.

Several other detector configurations were explored, while keeping the total cost fixed, including four subdetector modules with 10% coverage and five subdetector modules with 4% coverage. While these two options present similar sensitivities for $p \to e^+\pi^0$ searches, they are inferior to the others for $p \to \bar{\nu} K^+$and low-energy neutrino physics.

A uniform 40% photocathode coverage would clearly enhance UNO's low-energy sensitivity, but it would incur additional cost of ~\$160M. To retain the possibility of additional photo-cathode coverage, should a compelling physics case for it arise, the PMT mounting system is designed to accommodate a possible future upgrade.

2.6 Data Acquisition

While UNO does not require cutting-edge readout or triggering, it could benefit from relatively modest improvements to the dual-hit electronics used by Super-Kamiokande. In the conceptual design, waveform digitization of the PMT signals (with roughly 200 MHz sampling frequency and several ms full-scale) opens a number of possibilities for enhancing the detector's sensitivity. Energy resolution and reconstruction of higher energy events (*e.g.,* $p \to e^+\pi^0$) will benefit from the ability to distinguish direct Cherenkov light from later-arriving scattered and reflected photons. $\mu \to e$ identification can be extended to as little as 50 ns after the global trigger, raising the efficiency to nearly 100% and improving background rejection for $p \to e^+\pi^0$. Freed from the limitations of dual-hit electronics, a multi-level trigger would be implemented, using the digital pattern of hits to eliminate accidental coincidences and lower the effective threshold. Waveform digitization could also be used (after the fact) to find lower-energy coincidences during a supernova burst, again allowing more physics to be done with less light collection.

While the potential benefits of improved electronics are many, they are not yet firmly established. Existing analysis software, designed for dual-hit electronics, was not designed to take advantage of the much more detailed event data provided by waveform digitizers. Next-generation reconstruction algorithms are now under development, and will permit more quantitative study of our data acquisition concept.

2.7 Overburden

The optimal detector overburden is influenced by a number of factors, including physics goals, cosmic ray background, excavation and installation costs, structural stability and rock temperature. Thus, the question is non-trivial and the choice depends on the specific characteristics of a given site. With an outer detector veto and waveform electronics, cosmic ray background even at modest depth ($\sim$2000 mwe) will not compromise nucleon decay studies, however the greater demands of a solar neutrino physics program would require a depth of at least 3000 mwe to avoid unacceptable inefficiency or background from muon-induced spallation products.

2.8 Bibliography

[1] Talk by D. Lee Petersen at NNN99 Workshop at Stony Brook; See his talk on http://superk.physics.sunysb.edu/NNN99.

Chapter 3

Nucleon Decay

3.1 Overview

Proton decay offers a unique window to view physics at truly short distances ($< 10^{-30}$ cm). It is one of the crucial predictions made by the hypothesis of grand unification of the fundamental particles and of their forces: Thus the discovery of proton decay would have far-reaching consequences on our understanding of nature at the highest energy scale.

Baryon number conservation was first proposed by Stueckelberg (1938) [1] and Wigner (1949) [2]. This conservation law can be proved exact to an extremely good approximation from such evident data as the ambient level of radioactivity. If we assume that each violation is associated with the emission of a charged particle or a gamma-ray, the resultant limit is greater than 10^{16} years. A series of tests, starting with one by Reines et al. (1954) [3] that yielded a limit of greater than 10^{22} years, produced increasingly stringent limits.

Until the 1970's, there was no compelling theoretical reason to question baryon-number conservation. Instead, experiments were motivated by the conviction that fundamental laws should be tested as the means become available. The situation changed with the success of Weinberg and Salam's ideas regarding unification of the weak and electromagnetic forces and with the development of quantum chromodynamics describing the strong interaction. Theorists proposed to unify these three interactions in a way that called for quarks to change into leptons with the result that nucleons would decay. The simplest of these grand unification theories, SU(5) [4], predicted a proton lifetime in the range 10^{28} to 10^{30} years and specified the decay modes. These predictions stimulated world-wide, dedicated searches for proton decay and led to the construction of the Frejus, IMB, Kamiokande, Kolar and NUSEX underground experiments during the 1980's. In its initial report in 1983, the largest of these detectors, IMB, set a lower limit on SU(5)'s dominant decay process ($p \to e^+\pi^0$) at $\tau/\beta = 6.5 \times 10^{31}$yr, effectively ruling out the minimal theory. With additional data collected over the remainder of the decade, the lower limit on the lifetime was improved to 8.5×10^{32}yr.

Results obtained by LEP experiments provided high precision measurements of electroweak and strong coupling constants at the M_Z scale and allowed for more conclusive extrapolations to high energies in search of the unification scale. In a non-supersymmetric

Standard Model with only one Higgs doublet, the convergence of coupling constants at a single point is excluded. With additional Higgs doublets, unification can be obtained. However, this unification is at a scale conflicting with the experimental limits on the proton lifetime. In the supersymmetric extension of SU(5) with a minimal Higgs sector of two doublets, a single convergence point is obtained by fitting both the unification scale M_{GUT} and the SUSY breaking scale M_{SUSY}. This in turn predicted a proton decay lifetime of $\tau/\beta \sim 10^{34\pm1.2}$yr if the decay is dominated by gauge boson exchange. In many SUSY models, Higgs exchange interactions further reduced the proton lifetime. In unification models with dominant baryon violation amplitude generated by the Higgs exchange, the decay rates of $p \to \bar{\nu}K^+$ and $n \to \bar{\nu}K^0$ would be dominant. For experimenters, those decay modes demand sensitivity to visible energies well below the 1 GeV typical of gauge boson mediated decay modes. Although strange particle production is strongly suppressed in the soft atmospheric neutrino spectrum, excellent topological and kinematic resolution (which allows kaon identification) is essential for background reduction.

These considerations suggested the possibility of observing proton decay with the operation of a larger, more sensitive, detector and were the primary motivation for construction of the Super-Kamiokande experiment in Japan. The search for nucleon decay requires massive detectors. A search with a sensitivity of 10^{33} years requires a detector with approximately 10^{33} nucleons. Since there are 6×10^{29} nucleons per metric ton of material, this implies detectors of the multi-kiloton scale. The 50,000 kt Super-Kamiokande detector is the most recently constructed detector and began taking data in 1996. A summary of the limits currently established by Super-Kamiokande along with the limits obtained by other nucleon decay experiments is given in Table 3.1.

Background for nucleon decay arises from interactions of muons and neutrinos produced by cosmic-ray interactions in the upper atmosphere. By locating the detectors underground, experimenters can reduce cosmic-ray muons to a manageable level, but neutrino background is unavoidable. The vast majority of atmospheric neutrino interactions bear little resemblance to nucleon decay, but a small fraction are indistinguishable (based on topology and kinematic parameters) from the signal. Recently, data from a scaled down version of Super-Kamiokande installed in the neutrino beamline at KEK (K2K 1kton detector) has allowed a high-statistics study of these backgrounds in a controlled environment, and will permit a far more precise estimation of their incidence once fully analyzed. More sophisticated calculations of atmospheric neutrino production in the atmosphere, coupled with data on primary cosmic-ray fluxes (BESS) and secondary particle production (HARP and E907), will likewise refine our understanding of the atmospheric neutrino fluxes themselves in the near future.

While data from existing experiments have yet to reveal evidence for proton decay, it demonstrates that still more sensitive searches are possible. Recent papers by Babu, Pati, Wilczek [5] and others stress the significance of Super-Kamiokande's discovery of neutrino oscillations to the mechanisms for nucleon stability. Their work, based on an SUSY SO(10) framework, can describe the masses and mixings of all quarks and leptons. It predicts proton lifetimes in the range of 10^{33} to 10^{34} yrs, with $\bar{\nu}K^+$ being the dominant decay mode, and suggests that an improvement in the current Super-Kamiokande sensitivity by a factor of

Table 3.1: 90% C.L. lower limit on nucleon decay lifetime.

Decay mode	90% C.L. Lower Lifetime Limit ($\times 10^{32}$)				
	Super-K	IMB	Kamiokande	Soudan-2	Frejus
$p \to e^+\pi^0$	50	8.5	2.6		0.70
$p \to e^+\eta^0$	11	5.1	1.4		0.44
$p \to e^+\rho^0$	6.1		0.75		0.29
$p \to e^+\omega$	2.9	1.5	0.45		0.17
$p \to e^+K^0$	5.4	1.1	1.5	0.85	0.60
$p \to e^+K^{*0}$		0.84	0.52		0.10
$p \to e^+\gamma$	73	11			1.3
$p \to \mu^+\pi^0$	37	7.4	4.4		0.81
$p \to \mu^+\eta$	7.8	1.7	0.69		0.26
$p \to \mu^+\rho^0$			1.1		0.12
$p \to \mu^+\omega$		1.4	0.57		0.11
$p \to \mu^+K^0$	10	1.6	1.2	1.2	0.54
$p \to \mu^+\gamma$	61	8.6			1.6
$p \to \bar{\nu}\pi^+$		0.10	0.45		0.10
$p \to \bar{\nu}\rho^+$		1.7	0.27		0.24
$p \to \bar{\nu}K^+$	16	1.5		0.43	0.15
$p \to \bar{\nu}K^{*+}$		0.61	0.20		0.17
$n \to e^+\pi^-$		2.6	2.3		0.70
$n \to e^+\rho^-$		2.6			0.41
$n \to e^+K^-$		0.17			
$n \to \mu^+\pi^-$		1.5	2.2		0.35
$n \to \mu^+\rho^-$		2.4	0.23		0.22
$n \to \mu^+K^-$		0.26			
$n \to \bar{\nu}\pi^0$		1.8	1.8		0.13
$n \to \bar{\nu}\eta^0$	5.6	1.8	0.54		0.29
$n \to \bar{\nu}\rho^0$		.13	0.19		0.09
$n \to \bar{\nu}\omega$		1.2	0.43		0.17
$n \to \bar{\nu}K^0$	3.0	0.31	0.86	0.26	0.15
$n \to \bar{\nu}K^{*0}$		0.85	0.21		0.22
$n \to \bar{\nu}\gamma$		0.39			0.24

five to ten might allow the observation of proton decay.

Grand unified theories continue to predict a broad range of possible proton lifetimes. There is evidence that our fundamental approach to unification is sound, and nucleon decay is one of the few accessible regimes where grand unified theories can be directly confronted with experimental data. Further progress toward detection of this unique process may be crucial to the future development of physics; this dictates that the search for evidence for nucleon decay be pursued with renewed vigor.

3.2 Theoretical Background and Motivation

3.2.1 Grand Unified Theories and Nucleon Decay

There has been great interest in searches for baryon number violation and proton decay after the development of grand unified theories (GUTs) in the early 1970's. These theories embed the standard model $G_{SM} = \mathrm{SU}(3) \times \mathrm{SU}(2) \times \mathrm{U}(1)_Y$ gauge group in a simple gauge group G_{GUT}. The Pati-Salam idea that lepton number could be considered as the fourth color was an early step in the direction of unification; an associated gauge group was $\mathrm{SU}(4) \times \mathrm{SU}(2) \times \mathrm{SU}(2)$ [6]. Considering fully unified models with simple embedding groups, since $G_{GUT} \supset G_{SM}$, it follows that the rank $r(G_{GUT}) \geq r(G_{SM}) = 4$. Since $r(SU(N)) = N - 1$, it follows that in the SU(N) series of groups, a minimal GUT would be SU(5), and this was the first one to be studied, by Georgi and Glashow [4]. In this theory, the 15 Weyl fermions of a given generation fit nicely into a 10-dimensional second rank antisymmetric tensor representation $\psi_L^{\alpha\beta}$ and a conjugate fundamental representation $\psi_L^{c\alpha}$. Specifically, for the first generation, the $\bar{5}_L$ contains the d_L^c and $(\nu_e, e)_L^T$, while the 10_L contains the $(u, d)_L^T$, u^c, and e^c. In terms of $\mathrm{SU}(3) \times \mathrm{SU}(2)$ SM representations, we have

$$5 = (3, 1) + (1, 2) \tag{3.1}$$

$$10 = (3, 2) + (\bar{3}, 1) + (1, 1) \tag{3.2}$$

The model contains $N^2 - 1 = 24$ gauge bosons in the adjoint representation. The decomposition relative to the SM is given by

$$24 = (8, 1) + (1, 3) + (1, 1) + (3, 2) + (\bar{3}, 2) \tag{3.3}$$

Thus, of the 24 gauge bosons in SU(5), 12 are the gauge bosons of the standard model: 8 gluons, the $W^{\pm}$, Z, and γ. The other 12 consist of (X, Y) and $(X^{\dagger}, Y^{\dagger})$, where X and Y are color triplets with electric charges $-4/3$ and $-1/3$, respectively. The contributions to the anomaly in gauged currents cancel between the two fermion representations. The full SU(5) gauge symmetry must be broken at a high scale to that of the standard model. This is done via a Higgs field in the adjoint representation. The further breaking of the electroweak symmetry is done via an electroweak-doublet Higgs in the fundamental representation of SU(5).

A more complete, although less minimal, grand unification is achieved with the GUT group SO(10), with rank 5 [7]. Maximal subgroups of SO(10) include SU(5) $\times$ U(1) and $SO(6) \times SO(4) \sim SU(4) \times SU(2) \times SU(2)$. It thus contains both the Georgi-Glashow SU(5) group and the Pati-Salam $SU(4) \times SU(2) \times SU(2)$ (422) group. In terms of the decomposition with respect to SU(5) representations we have

$$16 = 10 + \bar{5} + 1 \tag{3.4}$$

so that in addition to the known fermions of each generation, the model also contains a G_{SM}-singlet field, denoted χ_L^c, which is the conjugate of a χ_R with the quantum numbers of (an electroweak singlet) neutrino. The gauge boson sector is expanded relative to that of SU(5) and contains 45 fields.

In general, GUTs introduce a number of attractive features to particle physics:

- Because of the embedding of the standard model in a simple group, they predict the ratios of the three gauge couplings for the SU(3), SU(2), and U$(1)_Y$ factor groups. As discussed below, the predictions of supersymmetric GUTs for this gauge coupling unification are in general agreement with the data.

- They provide a simple and natural explanation of charge quantization, since the charge operator is a generator (equivalently, a linear combination of generators) of the Lie algebra associated with G_{GUT}.

- They unify quarks and (anti)leptons, since these are placed together in irreducible representation(s) of the gauge group G_{GUT}. Indeed, as a consequence, they predict new interactions that transform quarks into antiquarks and into (anti)leptons, and these, in turn, lead to the decay of the proton and the (otherwise stable) bound neutron.

- Because of the unification of quarks and leptons, these theories yield viable predictions for fermion mass relations and the Cabibbo-Kobayashi-Maskawa quark mixing matrix.

- The SO(10) GUT incorporates an elegant seesaw mechanism [8] that yields naturally small neutrino masses of the generic form $m_\nu \sim m_D^2/m_R$, where m_D is a Dirac-type mass, related to the up-type quarks, and m_R is a mass associated with a bilinear consisting of electroweak-singlet neutrinos, of order the GUT scale. This yields values for neutrino masses that are consistent with the values suggested by current atmospheric and solar data.

- The violation of B and L in these theories, together with effects of electroweak instantons at finite temperature, can provide a mechanism for baryogenesis and leptogenesis.

- String theories are appealing candidates for theories of quantum gravity. Ideally, one hopes that it will be possible to deduce the structure of the quantum field theory below the string scale from this framework. While it is still an outstanding challenge to deduce the low-energy field theory from the underlying string theory, one can at least plausibly motivate the appearance of grand unified theories.

Specific appeals of SO(10) include the following:

- All of the the fermions in a given generation can be placed into a single irreducible representation, the 16-dimensional spinor representation of SO(10).
- Rather than having the anomaly in gauged currents cancel between different fermion representations as in SU(5), the theory has the technical property of being "safe", i.e., free of any gauge anomaly, despite having complex representations [9].
- The fermion mass predictions are more complete than in SU(5), involving not just the down-type quarks and charged leptons, but also the up-type quarks and neutrinos. In particular, one gets the seesaw mechanism for neutrino masses.
- If one considers generalizing N_c from three and inquires under what conditions one can achieve minimal grand unification, with all of the fermions of a single generation fitting into a single representation, one is led to a GUT group $SO(2(N_c + 2))$ and the condition [10]
$$2^{N_c+1} = 4(N_c + 1) \tag{3.5}$$
The only solution of this condition is for $N_c = 3$, which provides a deeper insight into why there are three colors.

In these theories, proton and bound neutron decay occurs via Feynman diagrams involving the exchange of X and Y gauge bosons in SU(5) and similar gauge bosons in SO(10). For example, in one such diagram, two u quarks in a proton combine to form a virtual $X^\dagger$ in the s-channel, which then produces a $d^c e^+$ pair. The d^c binds with the spectator d in the proton to form an outgoing π^0, thereby yielding the decay $p \to e^+\pi^0$. An example of another diagram contributing to this decay is a t-channel exchange in which a u emits a virtual $X^\dagger$ and changes into a u^c; the $X^\dagger$ is absorbed by a d quark, changing it to a e^c, and then the u^c combines with the spectator u to form a π^0, thereby yielding the final state $e^+\pi^0$. Higgs scalars can also contribute to proton and bound neutron decay.

As one moves below the mass scale M_{GUT} where the GUT gauge symmetry is spontaneously broken to the SM, one has three, rather than one, gauge couplings, and these run separately. Working back from the observed values of the electroweak couplings g_1 and g_2, or equivalently, $\sin^2\theta_W$ and α_{em}, in conjunction with the value of the strong coupling parameter α_s, early estimates suggested a unification point around 10^{14} GeV, which would then play the role of M_{GUT}. Based on this, estimates of the proton lifetime for minimal non-SUSY SU(5) were of order $10^{29\pm1.5}$ yrs. This prediction is long excluded by experiments. But supersymmetric GUTs brings a few complexion to proton decay as discussed below.

Although grand unified theories achieve a number of desirable theoretical goals, they bring with them some new problems. One is the gauge hierarchy problem, namely that the condition that the GUT scale is much larger than the electroweak scale, $M_{GUT} >> M_{ew}$, is unstable to radiative corrections. That is, considering the Higgs potential terms in the SM Lagrangian, $V = \mu^2\phi^\dagger\phi + \lambda(\phi^\dagger\phi)^2$, one-loop radiative corrections would modify $\mu^2 \to$

$\mu^2 + O(\lambda M_{GUT}^2)$. Thus, preserving $\mu << M_{GUT}$ would require extreme fine-tuning. One promising solution to this problem is supersymmetry which naturally suppresses the large radiative correction to Higgs mass, and this gave rise to the development of supersymmetric (SUSY) GUTs. Of course, supersymmetry is not observed at lower energies, and must be broken. However, the scale at which it is broken cannot be very much larger than the electroweak scale, $M_{ew} \sim 250$ GeV, or else the role of supersymmetry in protecting the Higgs sector against large radiative corrections would be lost. Current models hypothesize a SUSY breaking scale of several hundred GeV to a TeV. The proton would decay much too rapidly in such theories if one did not impose a certain discrete symmetry known as R-parity. This is defined to take the value $R = 1$ for each of the usual fields, i.e., matter fermions, gauge bosons, and Higgs, and $R = -1$ for each of their superpartners, i.e., squarks, sleptons, gauginos, Higgsinos. Henceforth, we assume that this symmetry is imposed.

3.2.2 Predicted Nucleon Decay Rates

As the data from LEP and SLC, in conjunction with other data for $\sin^2\theta_W$ and α_s, have shown, in the minimal supersymmetic standard model (MSSM), the gauge couplings approximately unify, at a scale $M_{GUT} \sim 10^{16}$ GeV, which thus characterizes a SUSY GUT [11]. (Here the MSSM contains the usual particle content of the SM with the addition of a second Higgs doublet whose hypercharge is opposite to that of the usual Higgs doublet, together with the addition of all of the corresponding superpartners.) In contrast, although early data in the 1970's was consistent with gauge coupling unification in nonsupersymmetric GUTs, the more accurate data obtained in the 1990's has shown that the gauge couplings fail to unify in such theories. In view of this, the role of SUSY in protecting the gauge hierarchy, and the fact that the first generation of dedicated proton decay searches ruled out nonsupersymmetric GUTs, we henceforth restrict our discussion to supersymmetric GUTs, for now. One can consider both SUSY SU(5) and SO(10), with the MSSM embedded in either. While the regular known fermion and gauge boson sectors of these theories, and hence also the full corresponding chiral and vector superfields, are fixed, the full set of Higgs chiral superfields varies from model to model. A general statement is that realistic SUSY GUTs contain at least a pair of color-triplet Higgs fields H_{ic}, $i = 1, 2$. (Even in nonsupersymmetric GUTs a color-triplet Higgs field was present, e.g., as the first three components of the 5 of Higgs in the original SU(5) model. Since it contributed at tree level to proton decay, its mass had to be be of order the GUT scale, and the huge splitting between this and the mass of the electroweak doublet Higgs forming the 4,5 components of the 5 of Higgs was known as the second hierarchy problem. Unlike the gauge hierarchy problem, which was solved with the hypothesis of supersymmetry, the second hierarchy problem, that of doublet-triplet Higgs mass splitting, remains even in SUSY GUTs and requires further devices for its solution.)

As noted above, the evidence for neutrino masses provides, via the seesaw mechanism, further support for SUSY SO(10). Examples of recent SO(10) models that fit Super-Kamiokande data on atmospheric and solar neutrinos include [12, 13, 14].

In general, in grand unified theories, the lowest-dimension operator products that mediate nucleon decay contain a part of the form QQQ, coupled to a color singlet, to annihilate the three quarks in the nucleon. The fourth field is a lepton, so that the full Lorentz-invariant operator product is of the form $QQQL$. This is a dimension-six operator, and hence involves a c-number coefficient with dimensions of inverse mass squared. In conventional nonsupersymmetric GUTs, as discussed above, the exchange of the massive gauge bosons with propagators of the form $1/M_{GUT}^2$ yield c-number coefficients for these operator products of the form α_{GUT}/m_{GUT}^2 in the amplitudes.

In SUSY GUT theories, there are two main contributions to proton decay. The dominant one arises from one-loop graphs involving the fermionic superpartners of the Higgs color triplets and the scalar superpartners of the fermions. Because the Higgs couplings to fermions are proportional to fermion masses, and the same couplings hold for the corresponding Higgsinos, it follows that the decays into higher-generation particles are preferred, subject to obvious constraints from phase space. Because the only GUT-scale mass in the diagram occurs on a fermion, rather than a boson, line, the amplitude involves only an external factor of $1/M_{GUT}$ rather than $1/M_{GUT}^2$ as for the gauge boson-induced amplitude. For this reason, this type of operator is often called "dimension-5", although of course the actual operator is still the dimension-6 $QQQL$ operator. The other factor with dimensions of inverse mass that multiples the $QQQL$ operator in these types of theories is $1/m_{SUSY}$, where m_{SUSY} is the SUSY breaking scale.

Recall that SUSY GUTs introduce two new features to proton decay: (i) First, by raising M_X to a higher value about 2×10^{16} GeV (contrast with the non-SUSY case of nearly 3×10^{14}), they strongly suppress the gauge-boson-mediated d=6 proton decay operators, for which $e^+\pi^0$ would have been the dominant mode (for this case, one typically obtains: $\Gamma^{-1}(p \to e^+\pi^0)|_{d=6} \sim 10^{35.3\pm1.5}$ yrs). (ii) Second, they generate d=5 proton decay operators [15] of the form $Q_iQ_jQ_kL_l/M$ in the superpotential, through the exchange of color triplet Higgisinos, which are the GUT partners of standard Higgs(ino) doublets, such as those in the $5 + \overline{5}$ of SU(5) or 10 of SO(10). Assuming that a suitable doublet-triplet splitting mechanism provides heavy GUT-scale masses to these color triplets and at the same time light masses to the doublets, these "standard" dimension-5 operators, suppressed by just one power of the heavy mass and the small Yukawa couplings, are found to provide the dominant mechanism for proton decay in SUSY GUT [16, 17].

Now, owing to (a) Bose symmetry of the superfields in $QQQL/M$, (b) color antisymmetry, and especially (c) the hierarchical Yukawa couplings of the Higgs doublets, it turns out that these standard d=5 operators by themselves lead to dominant $\overline{\nu}K^+$ and comparable $\overline{\nu}\pi^+$ modes, but in all cases to highly suppressed $e^+\pi^0, e^+K^0$ and even μ^+K^0 modes.

It has recently been pointed out that in SUSY GUTs based on SO(10) or G(224)=SU(2) $\times$ SU(2) $\times$ SU(4) which assign heavy Majorana masses to the right-handed neutrinos, there exists a new set of color triplets, and thereby very likely a new source of d=5 proton decay operators [5], which are related to neutrino masses. In general, these new operators compete favorably with the standard ones. They can, however, lead to prominent μ^+K^0 modes, with $\overline{\nu}K^+$ still being dominant. The color-triplet Higgsino-exchange leads to transitions of the type $\tilde{q}\tilde{q}q \to \bar{l}$. Supplemented by wino-exchange in a loop, they lead to transitions of the type

$qqq \rightarrow \bar{l}$, which in turn induce proton decay. The expression for the inverse rate of proton decay, induced via such a loop, is given by [14, 18]

$$\Gamma^{-1}(p \rightarrow \overline{\nu}_\tau K^+) \approx \\ (4 \times 10^{30} yrs) \times (\tfrac{0.67}{A_s})^2 [\tfrac{0.014 GeV^3}{\beta_H}]^2 [\tfrac{1/6}{m_{\tilde{w}}/m_{\tilde{q}}}]^2 [\tfrac{m_{\tilde{q}}}{1\ TeV}]^2 [\tfrac{2 \times 10^{-24} GeV^{-1}}{\hat{A}(\overline{\nu})}]^2 \tag{3.6}$$

This is a general expression that applies to both SUSY SU(5) and SUSY SO(10). The

model dependence enters through the entity $\hat{A}(\overline{\nu})$, which denotes the strength of the $d = 5$ operator, multiplied by the CKM mixing parameters that enter into the wino-vertices. Thus $\hat{A}$ depends for example on the mass of the color triplet, on the SUSY-parameter $\tan\beta$ and also on the way the different contributions to the amplitude interfere with each other. The entity β_H measures the matrix element of the three quark-operator between the proton and the vacuum state. Two early lattice gauge theory calculations of β_H are, in units of GeV^3, 0.029(6) [19] and $\sim$ 0.050 [20]. The recent lattice calculation in Ref. [21] yields the more precise accurate value $\beta_h = 0.014(1)$ GeV^3, which is used in (3.6). In order for SUSY to protect the Higgs sector from large radiative corrections, one normally would not take the SUSY breaking scale too much larger than the electroweak scale of $v/\sqrt{2} = 175$ GeV; in eq. (3.6) we use 1 TeV. A similar estimate was obtained in Ref. [22] from a different SO(10) SUSY GUT.

It may also be noted that if one attributes the 2.6 σ discrepancy, $a_{\mu,exp.} - a_{\mu,thy} = (4.3 \pm 1.6) \times 10^{-9}$ between the recent measurement by a Brookhaven experiment of the anomalous magnetic moment of the μ^+ [23] and the theoretical calculation supersymmetric contributions [24], one is led to infer that

$$4.3 \times 10^{-9} = (1.4 \times 10^{-9}) \Big(\frac{100\ \text{GeV}}{M_{SUSY}} \Big)^2 \tan\beta \tag{3.7}$$

where we recall that $\tan\beta = v_u/v_d$ is the ratio of the vacuum expectation values of the two Higgs doublets in the MSSM. Thus, for example, for the illustrative value $M_{SUSY} \simeq 400$ GeV, one would have $\tan\beta \simeq 50$. (The LEP limit on the mass of the lightest Higgs in the MSSM also suggests independently that $\tan\beta \gtrsim 4$.) If one substituted these values into the proton decay rate, it would substantially shorten the lifetime (for large $\tan\beta$, the rate goes like $\tan\beta^2$; the original estimate in (3.6) assumed a a value of $\tan\beta$ of about 2–3.

The central value of $\Gamma^{-1} = \tau/B$ for $p \rightarrow \bar{\nu} K^+$ in SUSY SO(10) models in eq. (3.6) is somewhat less than the current Super-Kamiokande limit of 1.6×10^{33} years. (This difference would be rendered more severe if one were to substitute values such as the illustrative ones $M_{SUSY} = 400$ GeV and $\tan\beta = 50$ from fitting the discrepancy in the muon anomalous magnetic moment to SUSY.) In view of these estimates, one could argue that current Super-Kamiokande data disfavor the simplest SUSY GUTs. However, the idea of supersymmetric grand unification is sufficiently attractive that one would not like to give it up, and instead one concentrates on carefully examining possibilities that yield longer proton lifetimes. If one tries to make color triplet Higgs much heavier than the SUSY GUT scale, this produces large corrections to gauge coupling unification, although one can try to arrange further cancellations to maintain this coupling unification (e.g., [22]). However, as discussed in [14, 18], what enters the calculation is an effective color triplet mass, which can be greater than the SUSY GUT scale without producing problems with gauge coupling unification. Moreover, one can entertain the possibility of having a simple group at the string scale break immediately to the SU(4) $\times$ SU(2) $\times$ SU(2) group, removing the problem with proton decay mediated by Higgs color triplets. Another alternative is denoted the ESSM (extended supersymmetric standard model) [18, 25], and involves the addition of chiral superfields transforming as 16 and $\bar{1}6$ of SO(10); these are vectorlike as regards the standard model gauge group but have different charges under a string-motivated $U(1)_A$. Adding such complete SO(10)-multiplets would of course preserve gauge coupling unification. In this model the partial lifetime for $p \to \bar{\nu} K^+$ can be increased by factors of order 10^2 relative to the prediction (3.6) in usual SUSY SO(10). A similar increase in $\tau/B(p \to \bar{\nu} K^+)$ can be achieved in models in which a presumed underlying string theory yields the gauge group G(224) at a high scale instead of SO(10), which could still satisfy gauge coupling unification at the string scale. In this case the usual box diagrams involving colored triplet higgsinos would not occur, but the other class of contributions proportional to M_{GUT}^{-1} in the amplitude would occur [18]. In these types of theories, $\tau/B(p \to \bar{\nu} K^+)$ could also be increased substantially relative to (3.6) and could also lead to prominent decays of the form $p \to \mu^+ K^0$ with typical branching ratios of 10 to 50 %.

A rather different theoretical possibility is illustrated by models with a low scale of quantum gravity, ∼10–100 TeV, and associated large extra dimensions [26]. Estimates for proton decay rates vary widely in these models.

Taking account of the range of SUSY GUTs and other theoretical possibilities, a rough estimate for an upper limit might be

$$\Gamma^{-1}(p \to \bar{\nu} K^+) \ \lesssim 10^{34} \text{ yrs} \tag{3.8}$$

Concerning other proton decay modes, there is also, for example, $p \to \mu^+ K^0$; typically this has a somewhat smaller, but still sizable, branching ratio, relative to $p \to \bar{\nu} K^+$. Correspondingly, there are also the bound neutron decays $n \to \bar{\nu} K^0$ and $n \to \mu^+ K^-$, again with comparable respective rates.

In addition to these favored decay modes, SUSY GUTs also lead to the same type of decays, such as $p \to e^+ \pi^0$, as nonsupersymmetric GUTs. These have much smaller branching ratios than the favored modes. A typical estimate in an SO(10) SUSY GUT is [27]

$$\Gamma^{-1}(p \to e^+ \pi^0) \simeq 1 \times 10^{35} \text{ yrs} \left(\frac{0.015 \text{ GeV}^3}{\beta_h}\right)^2 \left(\frac{M_{GUT}}{10^{16} \text{ GeV}}\right)^4 \tag{3.9}$$

where we have included the most uncertain factors. Since this decay mode is mediated by the GUT gauge bosons, its rate is much less model-dependent than the favored $p \to \bar{\nu} K^+$ decay mode, which depends on details of the SUSY GUT Higgs sector.

Table 3.2: Summary of nucleon decay lifetime limits set by Super-Kamiokande.

Mode	Exposure (kt·yr)	Efficiency	Background	Candidates	Limit (90% CL)
$p \to e^+\pi^0$	79.3	43%	0.2	0	5.0×10^{33}yr
$p \to \mu^+\pi^0$	79.3	32%	0.4	0	3.7×10^{33}yr
$p \to \bar{\nu}K^+$	79.3	49%	—	—	1.6×10^{33}yr
spectrum	79.3	33%	—	—	0.4×10^{33}yr
prompt γ	79.3	8.8%	0.5	0	1.0×10^{33}yr
$K^+ \to \pi^+\pi^0$	79.3	6.8%	1.7	1	0.6×10^{33}yr
$p \to e^+K^0$	70.4	19.4%	2.6	6	5.4×10^{32}yr
$p \to \mu^+K^0$	70.4	14%	2.8	1	1.0×10^{33}yr
$n \to \bar{\nu}K^0$	70.4	14%	36.4	38	1.8×10^{32}yr

The current Super-Kamiokande limit on $p \to \bar{\nu}K^+$ partial lifetime is in the vicinity of the predicted upper limits from the simplest SUSY GUTs. Thus, if this appealing theoretical framework is correct, this decay mode should be clearly observed by UNO given its increased sensitivity. Furthermore the central values of the simplest SUSY predicted $p \to e^+\pi^0$ decay mode partial lifetimes are few times 10^{34} to 10^{35} within reach of UNO.

The increased sensitivity of UNO for the $p \to e^+\pi^0$ decay mode, which many consider the fundamental decay mode of proton, enhances its potential for a major discovery not only in the framework of SUSY GUTs but also in the framework of other variety of non SUSY GUT models. This provides a very strong motivation for the UNO project.

3.3 Current Experimental Results

The current and the past experimental searches for nucleon decays can be grouped into water Cherenkov detectors and calorimeters. The former is represented by IMB, Kamiokande and Super-Kamiokande and the latter by Soudan-2 and Fréjus. In particular, it is interesting to consider the strengths and weaknesses of the various detectors so that we can appreciate the challenges faced by the UNO detector.

3.3.1 Water Cherenkov Detectors

Ring imaging water Cherenkov detectors have searched for nucleon decay since the early 1980's when the IMB detector was constructed. This detector in combination with the Kamiokande detector in Kamioka, Japan pushed the limits on the partial lifetime in the various decay modes into charged particles to more than 10^{32} years. The most recently

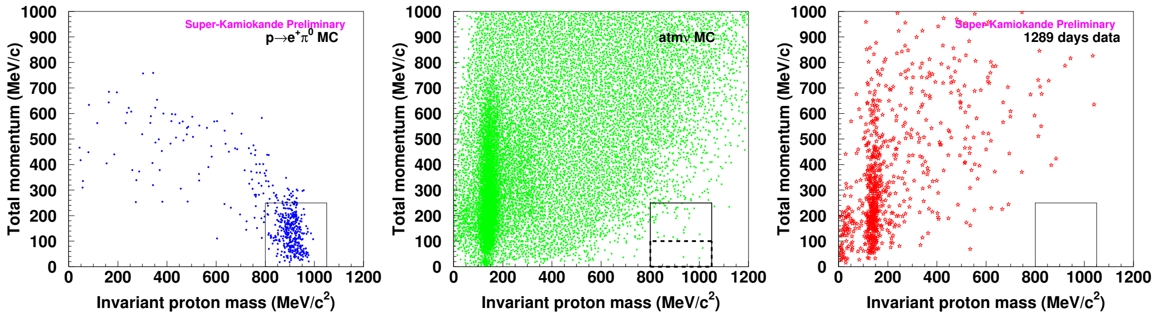

Figure 3.1: The total invariant mass and total momentum distributions for simulated proton decay and atmospheric neutrino background events as well as the distribution found in Super-Kamiokande for events passing the criteria (a)–(d) (see text). The boxed region in the figure shows the selection criterion (e) for the $p \to e^+\pi^0$ signal. A higher purity selection region is shown by the dashed box.

constructed and largest of these detectors is Super-Kamiokande, also located in Kamioka. This detector has been extremely successful and has pushed the limit for the partial lifetime of the proton by the $p \to e^+\pi^0$ mode to 5.0×10^{33} yr.

The partial lifetime limits set by Super-Kamiokande for several possible decay modes are shown in Table 3.2 along with the recovery efficiency, the estimated background, and the number of candidates that have been found. No unambiguous evidence has been found for nucleon decay.

3.3.1.1 Search for $p \to e^+\pi^0$

All of the final particles generated by a proton decay $p \to e^+\pi^0$ are all visible (an e^+ and two γ's) in a water Cherenkov detector, so it is possible to reconstruct the proton mass. Further, all of the products are effectively massless and can be identified so the invariant mass of the proton can be reconstructed unambiguously.

Candidate $p \to e^+\pi^0$ events are selected from the sample of fully contained events. While several interactions can create events which may be confused with the $p \to e^+\pi^0$ signal, the dominant sources of background events are the atmospheric electron neutrino interactions where an electron (or positron) plus a single pion is produced (for instance $\bar{\nu}_e + N \to e^+ + N' + \pi^0$). Even if there is no neutral pion produced, a charged pion may interact via charge exchange to become a neutral pion.

The contained event sample is reconstructed to find the event vertex, the number of rings, the particle type associated with each ring, and the momentum of each particle. A sample of $p \to e^+\pi^0$ candidates is selected by requiring (a) two or three Cherenkov rings which are (b) identified as electron-like, (c) in events with three reconstructed rings, the invariant mass of two rings must be consistent with the π^0 mass (85 MeV/c^2 $< m_{\pi^0} <$ 185 MeV/c^2), (d) there must be no decay electron signals, (e) the total invariant mass must be consistent with the

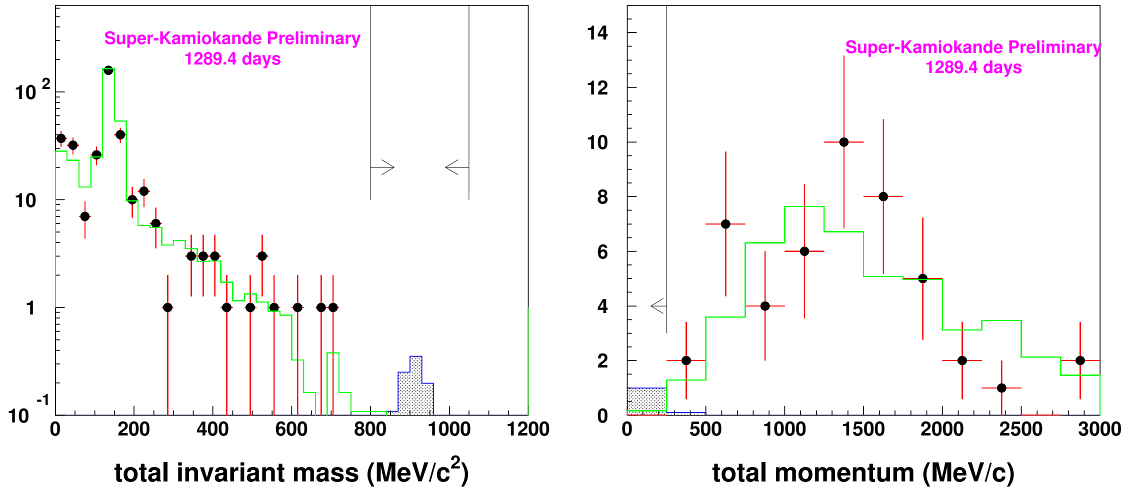

Figure 3.2: The distribution of the invariant mass and total momentum for events near the signal region. The distribution for the atmospheric neutrino background is shown by the histogram. The points show result for the Super-Kamiokande data.

proton mass (800 MeV/c^2 $< M_{total} <$ 1050 MeV/c^2), and (f) the total momentum must be consistent with the Fermi momentum of a proton in an oxygen nucleus ($P_{total} <$ 250 MeV/c).

Most of the background events have a total momentum far from zero while a proton decay candidate will have a momentum near zero. Excluding detector resolution effects, a proton decay candidate will have a total momentum less than the maximum Fermi momentum of a proton within an oxygen nucleus. Figure 3.1 shows the reconstructed total momentum and invariant mass distributions for samples of simulated $p \to e^+\pi^0$ candidates, simulated atmospheric neutrino background, and events from a 79.3 kt·yr exposure of Super-Kamiokande which have been selected by criteria (a)–(d). There are no candidate events. The events near the signal region are summarized in Figure 3.2. The invariant mass of events with a total momentum $P_{total} <$ 250 MeV/c is shown on the left. The total momentum of events with an invariant mass consistent with proton decay is shown on the right. In both cases, the data is consistent with the expectation.

The efficiency and estimated background for this analysis are summarized in Table 3.2. Using the data corresponding to 79kt·yr Super-Kamiokande found no candidate while 0.2 background events were expected. This information is used to obtain a lower limit on the proton partial lifetime of 5×10^{33} years at 90% C.L.

3.3.1.2 Search for $p \to \bar{\nu} K^+$

The momentum of the K^+ from $p \to \bar{\nu} K^+$ is 340 MeV/c and is below the Cherenkov threshold in water. Fortunately, K^+ production by atmospheric neutrinos is an extremely rare process and the existence of $p \to \bar{\nu} K^+$ can be inferred from the existence of a K^+ signal

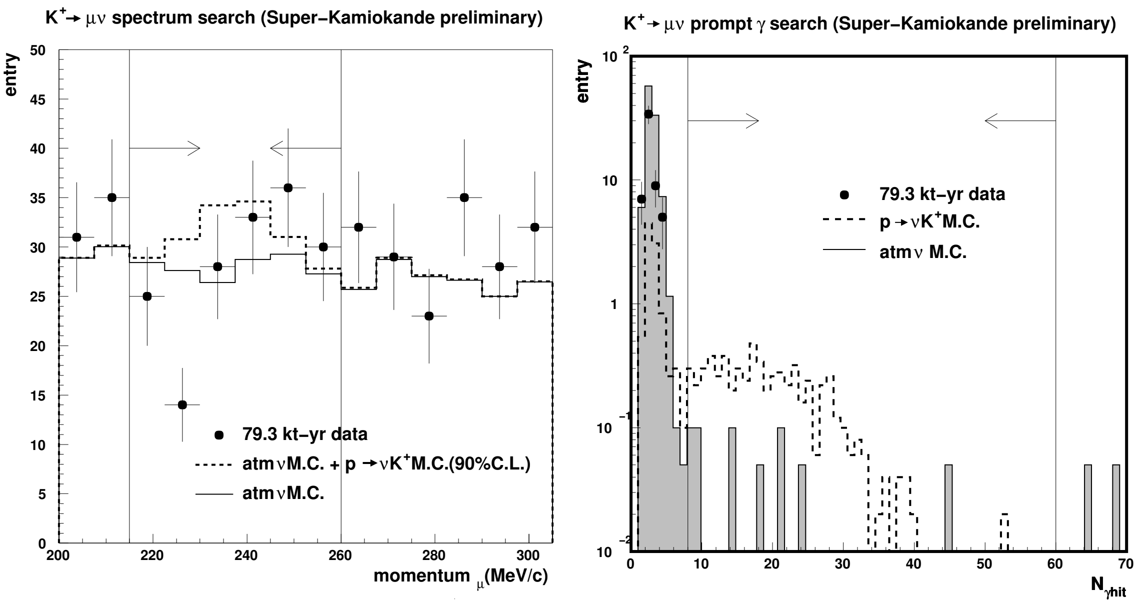

Figure 3.3: Comparision of the data and expectation for the two methods used to search for $p \to \nu K^+$; $K^+ \to \mu^+\nu_\mu$. The left plot shows the muon momentum spectrum near the value expected for the mono-energetic muon associated with K^+ decay. The right plot shows number of PMT hits associated with a prompt γ signal.

where the K^+ is in turn inferred by the decays into $\mu^+\nu_\mu$ or $\pi^+\pi^0$. Further, the K^+ has a small interaction probability in water, it exits the ^{16}O 97% of time, and it is estimated that 90% of K^+ decay at rest. Significantly, if a proton in the $p_{3/2}$ state of ^{16}O decays, the ^{16}O becomes an excited state of ^{15}N nucleus which promptly decays to the ground state by emitting a 6.3 MeV γ with a 41% probability. This is extremely important since the γ ray occurs simultaneous with the proton decay, and the K^+ has the lifetime of 12 ns. A requirement of a 6.3 MeV γ preceding the decay products from K^+ makes it possible to eliminate the majority of the background events.

The Super-Kamokande experiment uses three methods to search for the $p \to \bar{\nu}K^+$ mode: (1) $K^+ \to \mu^+\nu_\mu$ where the μ^+ decays to $e^+\nu_\mu\bar{\nu}_e$, (2) with a 6.3 MeV prompt γ and (3) $K^+ \to \pi^+\pi^0$ where the π^0 decays to two γ's.

The first method makes use of the fact that the decay is two-body and the μ^+ is mono-energetic with a momentum of 236 MeV/c. The selection criteria are that there is a μ-like ring whose momentum is between 215 and 260 MeV/c, no prompt gamma-ray signal exist, and a decay electron is found. These requirements substantially reduce the background, although a relatively large contamination of atmospheric neutrino events remains in the sample. The detection efficiency including the branching ratios is estimated to be 33%. Figure 3.3 shows the spectrum of muon momenta near the expected energy of muons from a K^+ decay at rest. No significant excess above the background is observed. The limit is

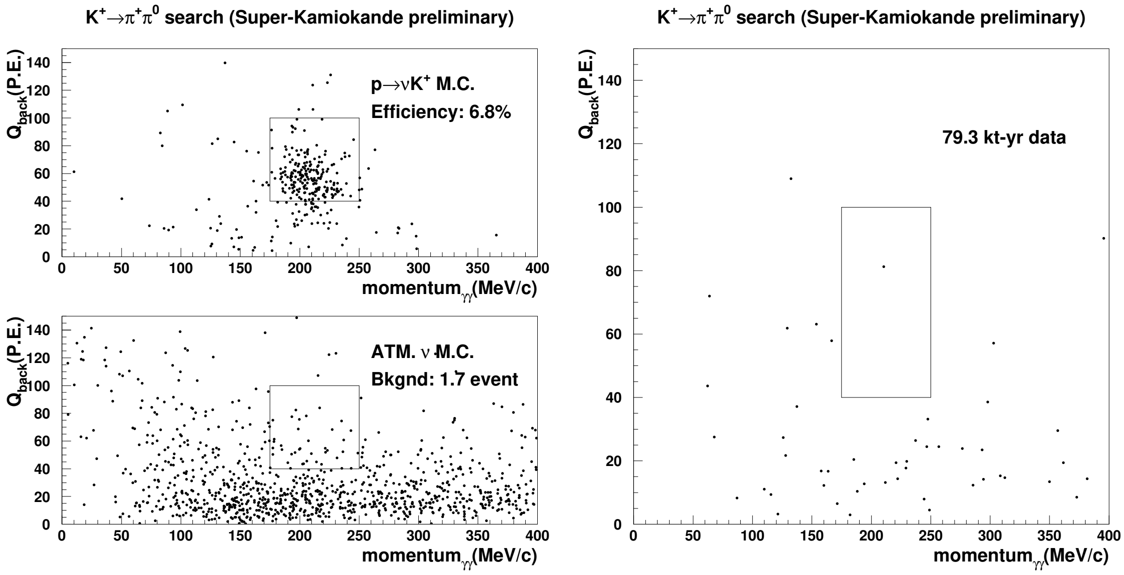

Figure 3.4: The distribution of the reconstructed π^0 momentum versus the charge in a cone opposite the reconstructed π^0 direction. The left plots show the distribution of events expected from $p \to \bar{\nu}K^+$ candidates and from the atmospheric neutrino background. The right plot shows the distribution of events in a 79.3 kt·yr exposure.

derived by fitting the shape of the spectrum to the expected atmospheric neutrino spectrum plus the spectrum expected from the decay of a K^+. The limit from this method on the partial proton lifetime was found to be 4.4×10^{32} years at 90% C.L.

In the second method an additional requirement of a prompt γ preceding the μ signal is applied by requiring that between 8 and 59 PMT hits occur outside a 50° cone around the muon ring in a sliding 12 ns window. The hits must occur between 0 ns and 120 ns prior to the muon signal. This additional requirement completely eliminates the background and no candidate is found. The expected background is 0.5 events. However, most of estimated background results from mis-reconstructed events. The reconstruction failure is understood and the background rejection will likely be improved in the near future. Figure 3.3 shows the distribution of the number of PMT hits found proceeding the muon signal. The atmospheric neutrino distribution extends well beyond a total of 8 PMT hits within the window. However, these events result from the misreconstruction of the primary particle in the event. The detection efficiency including the branching ratio is estimated to be 8.8%. The lower limit on the partial proton lifetime is thus obtained to be 1.0×10^{33} years at 90% C.L.

Unlike the first two methods the third method uses the K^+ decay to $\pi^+\pi^0$ where π^+ and π^0 both carry approximately 205 MeV/c in the opposite directions. While the π^0 is identified from the existence of two γs which are used to reconstruct π^0 mass, the π^+ is barely above the Cherenkov threshold and is reconstructed with very low efficiency. To maximize the $p \to \bar{\nu}K^+$ reconstruction efficiency, the reconstruction of the π^+ is not required. Instead, the charge in a 50° cone opposite the π^0 direction is summed (referred to as the backward charge, Q_{back}) and must be consistent with the expectation for a π^+ near threshold. The selection criteria for this decay mode are: (i) two e-like rings, (ii) one decay electron, (iii) 85 MeV/c^2 $< m_{\gamma\gamma} <$ 185 MeV/c^2, (iv) 175 MeV/c$< P_{\gamma\gamma} <$ 250 MeV/c, and (v) 40 p.e. $< Q_b <$ 100 p.e.

Figure 3.4 shows the distribution of the backward charge versus the reconstructed invariant mass of the e-like rings. The left plots show the expectation for the atmospheric neutrino background and the possible $p \to \bar{\nu} K^+$ signal. The right plot shows the distribution found during a 79.3 kt·yr exposure. After all cuts one event survives while 1.7 background events are expected. The detection efficiency including the branching ratios is estimated to be 6.8%, and the lower limit on the partial proton lifetime is found to be 5.9×10^{32} years.

The three independent methods just discribed can be combined to set a total lower limit on the proton partial lifetime. The combined limit is 1.6×10^{33} years using the data corresponding to an exposure of 79.3kt·yr.

3.3.2 Tracking Calorimeters

The detection capabilities for nucleon decay which have been demonstrated by water Cherenkov experiments, especially for resolving two-body decays in a large mass of monitored medium, are difficult to match using other techniques. However there are some decay channels for which the information provided by Cherenkov detection seems less than optimal. These channels involve higher multiplicities of track and shower prongs in the final state, and/or charged particles which are non-relativistic and hence are invisible to a Cherenkov experiment. Multiprong nucleon decays which have various degrees of these attributes are among the modes favored by supersymmetric (SUSY) grand unification theories (GUTs), e.g. $p \to \mu^+ K^0$, $K^0 \to \pi^+ \pi^-$. Motivated in part by these considerations, development of fine-grained tracking calorimeters for nucleon decay has proceeded in parallel with development of the water Cherenkov technique as an alternative experimental approach [28].

Tracking calorimeters used in non-accelerator experiments are ionization sensitive devices which are generally dense since they use iron or liquid argon as the monitored mass. The various calorimeters deployed underground differ in the method used for observing ionization and in the granularity of the sampling. The generic design goal for tracking calorimeters is to achieve bubble–chamber–like imaging for vertices and for non-relativistic as well as relativistic charged particles. In pursuit of this goal, detector geometries of iron plate calorimeters have evolved over the years from planar layered configurations, e.g. NUSEX and Fréjus, to the honeycomb lattice geometry utilized by Soudan 2. In the latter detector a spatial resolution of about 1 cm has been realized, and ionizing particles are imaged with dE/dx sampling thereby allowing proton tracks to be distinguished from charged pion and muon tracks. In general, tracking calorimeter detectors can provide relatively uniform detection efficiencies for a wide variety of nucleon decay channels, making them well-suited to branching ratio measurements in the case that signals are observed.

It has been demonstrated with prototype liquid argon time projection chambers (TPC) developed for the ICARUS project, that performance characteristics of underground calorimeters can be substantially improved. Indeed, a spatial resolution of $\sim$ 3 mm with ionization $\mathrm{d}E/\mathrm{d}x$ sampling is feasible with this approach. However, the extent to which performance and costing for such devices can be scaled to multi-kiloton detectors remains to be seen [29].

An oft-cited "advantage" attributed to fine-grained calorimeters is that discovery of nucleon decay is made possible with the observation of one or few well-imaged events. Unfortunately this advantage entails substantial cost; in all calorimeter experiments to date, fine granularity has been achieved by trading off monitored mass, thereby limiting the decay lifetime reach of the experiments. As it has turned out, there appears to be no nucleon decay signal at lifetimes below the maximum reach of deployed calorimeters ($\sim 2 \times 10^{32}$ years), and so these experiments have not been able to capitalize on high resolution imaging of individual events. Contrastingly, the water Cherenkov technique has proven readily extendable to higher fiducial masses while being remarkably amenable to refinements in light collection and in search strategies. The result is that no tracking calorimeter to date has approached the nucleon decay search capability realized by the Super-Kamiokande experiment. The current situation is made clear by the relatively modest lifetime limits reported by calorimeter experiments; examples are given below. For the foreseeable future, the only plausible calorimeter alternative to water Cherenkov detectors lies with ICARUS-type liquid argon TPCs.

3.3.2.1 Searches for $\overline{\nu}\mathrm{K}^+$, $\ell^+\mathrm{K}^0$, and $\overline{\nu}\mathrm{K}^0$ modes

Supersymmetric grand unification models introduce new processes involving SUSY particle loops for nucleon decay amplitudes. Nucleon decay diagrams of this type give integrals which vanish unless the transitions involve intergenerational mixing. Consequently final states containing strange mesons are predicted; in particular, two-body $(B-L)$ conserving decays involving strangeness +1 K^+ or K^0 mesons are expected to be prominent.

Of keen interest to SUSY GUTs models is the mode $\mathrm{p} \rightarrow \overline{\nu}\ \mathrm{K}^+$, for which a number of detailed lifetime calculations have been published. In Soudan 2, a search was carried out using a 3.56 fiducial kiloton year (kt·yr) exposure. The search utilized the visibility of the K^+ in the calorimeter together with the visibility of the decay electron from a stopped μ^+ ($\mathrm{K}^+ \rightarrow \mu^+\nu$, $\mu^+ \rightarrow \mathrm{e}^+\nu\overline{\nu}$) to minimize background from atmospheric neutrino interactions. Two K^+ decay channels were investigated: $\mathrm{K}^+ \rightarrow \mu^+\nu$ and $\mathrm{K}^+ \rightarrow \pi^+\pi^0$. One marginal candidate event was observed with total background estimated to be 1.54 events. The combined lower lifetime limit at 90% CL without (with) background subtraction is $4.3(4.6) \times 10^{31}$ years [30].

Searches for nucleon decay into two-body modes involving K^0 mesons have been carried out by Soudan 2 using a 4.41 fiducial kt·yr exposure. Channels investigated included proton decay into μ^+ K^0 and e^+ K^0 with $\mathrm{K}^0 \rightarrow \mathrm{K}^0_s$ or K^0_l, and neutron decay into ν K^0_s. Event selection criteria were developed by studying Monte Carlo samples of nucleon decay and atmospheric neutrino events. These simulations included the full detector response and were processed in conjunction with data events.

For these final states, the distributions of event invariant mass and of magnitude of

Table 3.3: Background–subtracted lifetime lower limits at 90% confidence level from Soudan 2. Correction of neutrino background for ν_μ-flavor depletion by oscillations has an effect for $\mathrm{n} \to \nu \mathrm{K}^0_s$; values without this correction are given in parentheses.

Decay Mode	Final State	$\epsilon\times$B.R.	ν_{Bk}	Total$_{Bk}$	Data	$\tau/B \times 10^{30}$y
$\mathrm{p} \to \mu^+\mathrm{K}^0_s$	$\mu^+\pi^+\pi^-$	0.16	< 0.2	< 0.2	0	150
	$\mu^+\pi^0\pi^0$	0.06	0.6	0.6	0	
$\mathrm{p} \to \mathrm{e}^+ \mathrm{K}^0_s$	$\mathrm{e}^+\pi^+\pi^-$	0.15	0.6	0.7	1	120
	$\mathrm{e}^+\pi^0\pi^0$	0.08	0.4	0.6	0	
$\mathrm{p} \to \mu^+\mathrm{K}^0_l$	$\mathrm{K}^0_l \to$ interaction	0.12	0.2	0.4	0	83
$\mathrm{p} \to \mathrm{e}^+\mathrm{K}^0_l$	$\mathrm{K}^0_l \to$ interaction	0.11	2.6	3.5	2	51
$\mathrm{p} \to \mu^+\mathrm{K}^0$	$\mu^+(\mathrm{K}^0_s + \mathrm{K}^0_l)$	0.17	<0.9	<1.2	0	120
$\mathrm{p} \to \mathrm{e}^+\mathrm{K}^0$	$\mathrm{e}^+(\mathrm{K}^0_s + \mathrm{K}^0_l)$	0.17	3.5	4.9	3	85
$\mathrm{n} \to \nu\mathrm{K}^0_s$	$\pi^+\pi^-$	0.17	3.6(5.1)	4.6(6.1)	7	51(59)
(3 showers)	$\pi^0\pi^0$	0.03	2.6	3.4	7	
(4 showers)	$\pi^0\pi^0$	0.05	0.6	1.1	2	
$\mathrm{n} \to \nu\mathrm{K}^0$	$\nu(\mathrm{K}^0_s + \mathrm{K}^0_l)$	0.13	6.8(8.3)	9.1(10.6)	16	26(29)

net three-momentum are approximately Gaussian. Consequently the density distribution of points on the invariant mass versus net momentum plane can be represented by a bi-variate Gaussian probability distribution function. Projections of this bi-variate Gaussian surfaces onto the M_{inv} versus $\left|\vec{P}_{net}\right|$ plane enable kinematic selections to be defined in an optimal way. Figure 3.5a shows the kinematic selection contour in the M_{inv} versus $\left|\vec{P}_{net}\right|$ plane which was used for $p \to \ell^+ \mathrm{K}^0_s$ searches in four separate channels.

Backgrounds from neutrinos and from cosmic ray interactions in the cavern rock distribute diffusely with respect to the search region as shown in Figs 3.5b,c. Only three data events satisfy this kinematic selection (Figure. 3.5d); one of the data events is shown in Figure. 3.6.

No evidence for a nucleon decay signal was observed; the lifetime lower limits reported by Soudan 2 at 90% CL are summarized in Table 3.3 [31].

For the two-body K^0_s channels, these limits are comparable to those reported earlier by Kamiokande and IMB-3 [32, 33]. For K^0_l channels, the Soudan 2 limits supersede previous Fréjus limits. A preliminary lifetime limits obtained by Super-Kamiokande using a 70 kt·yr exposure, the K^0_s channel limits of Table 3.3 have been improved upon by factors of 3 to 7 (See Table 3.2).

Table 3.4: Comparison of reported candidate events, estimated background, and 90% confidence level background-subtracted limits in nucleon decay experiments.

Mode	τ/B (10^{30} years)											
	Soudan 2 [35]			Fréjus [36, 37]			Kamiokande [32]			IMB-3 [33]		
	Evt	Bkd	Lim	Evt	Bkd	Lim	Evt	Bkd	Lim	Evt	Bkd	Lim
p $\rightarrow \mu^+\eta$	0	1.6	89	1	0.8	26	1	< 0.08	69	3	2.8	126
p $\rightarrow$ e$^+\eta$	1	1.7	81	0	0.1	44	0	< 0.04	140	0	0.2	313
n $\rightarrow \overline{\nu}\eta$	2	3.7	71	0	0.9	29	2	0.9	54	0	1.2	158
n $\rightarrow \overline{\nu}\pi^0$	4	3.8	39	1	1.2	13	1	3	100	6	6.6	112
p $\rightarrow \overline{\nu}\pi^+$	6	6.7	16	11	14	10	32	32.8	25	15	20.3	10

3.3.2.2 Searches for lepton(ℓ^+,$\overline{\nu}$) + meson(S=0) modes

While SUSY GUT models generally favor decay modes with final state K$^+$ or K^0 mesons, some models predict that certain other $\Delta(B-L) = 0$ modes involving non-strange mesons may have significant branching fraction. For example, in SUSY SO(10) it is possible for p $\rightarrow \ell^+ \eta$ to become prominent, along with $\overline{\nu}$ K and $\overline{\nu}\pi$ [5]. Two-body ℓ^+, $\bar{\nu}$ + π, η, ρ, and ω decays of nucleons were previously indicated to be of interest in the context of non-SUSY GUT models, and experimental searches by tracking calorimeters as well as by water Cherenkov experiments have been regularly reported.

Nucleon decay involving final state non-strange pseudoscalar or vector mesons can be significantly affected by intranuclear rescattering of these mesons within parent nuclei. Sizable inelastic rescattering may arise due to excitation of low-lying delta and N* baryonic resonances. This situation is rather different from that which arises with nucleon decay into modes involving K$^+$ or K^0 mesons, for which the absence of low-lying KN(S=+1) states implies relatively little inelastic scattering. For the tracking calorimeters, π or η intranuclear rescattering within heavy nuclei can reduce detection efficiencies for individual channels by 40–50% compared to efficiencies of lepton + K^0 modes of similar topology. Efficiencies for water Cherenkov experiments are similarly affected albeit to lesser degree since intranuclear rescattering is less probable in oxygen (A=16) than in iron (A=56). Thus intranuclear rescattering poses a complication for all lepton + non-strange meson(s) modes, one which generally penalizes tracking calorimeters more severely than water Cherenkov detectors.

Lifetime lower limits for $(B-L)$-conserving lepton + non-strange meson decays obtained with tracking calorimeters are comparable to but generally less stringent than limits reported by the older water Cherenkov experiments. By way of illustration, Table 3.4 provides comparisons for searches in five different lepton + pseudoscalar meson modes.

For each decay channel, Table 3.4 shows candidate events, estimated background, and the lifetime lower limit τ/B at 90% CL as reported by Soudan 2 and Fréjus, versus those reported by Kamiokande and IMB-3. There is reasonable consistency among the results from the four experiments; in all cases the occurrence of candidates is compatible with expectations for background arising from interactions of atmospheric neutrinos. The Soudan 2 limits, which are the highest achieved using an iron calorimeter, fall below the IMB-3 limits with the exception of p $\rightarrow \overline{\nu}\, \pi^+$. However for this mode Soudan 2 has not surpassed the Kamiokande limit. Taken together, the experimental results of Table 3.4 suggest that the two-body lepton + η modes are relatively background-free and may be fertile ground for searches with larger exposure. This inference appears to be borne out by new limits recently reported by Super-Kamiokande; these show improvements upon the lepton + η modes limits of Table 3.4 by factors of 4 to 6.

3.3.2.3 Searches for $(B - L)$ violating processes

In many GUTs models, nucleon decay changes baryon number B but also changes lepton number L in such a way that $(B - L)$ is conserved. That is, modes to be expected are $\Delta B = -1$, $\Delta L = -1$ nucleon-antilepton transitions such as p $\rightarrow$ e$^+$ π^0 or p $\rightarrow$ K$^+$ $\overline{\nu}$. Consequently nucleon decay searches have generally targeted two-body decay modes for which $\Delta(B - L) = 0$. Among the large water Cherenkov experiments to date, the targeting has been almost exclusive; possibilities for $(B-L)$-violating nucleon decay have received limited treatment by IMB-3 and almost no consideration by Kamiokande and Super-Kamiokande. It is however possible to have $(B - L)$ non-conservation within a GUTs framework, as has been shown with left-right symmetric GUTs models [38]. Indeed it has been argued that "the most natural explanation of the baryon asymmetry of the universe would require non-conservation of $(B - L)$ at an energy scale above the electro-weak scale" [39]. With regard to baryon instability, $(B - L)$ violation could give rise to new classes of processes such as nucleon decay into lepton + mesons, or di-nucleon decay of nucleons bound in nuclei (ΔB = -2), or neutron into anti-neutron oscillation. Among experiments to date, the most comprehensive investigation of these processes has been carried out by Fréjus.

Utilizing the resolution capability for multi-prong events and for detection of low energy pions and protons inherent with the experiment's planar iron tracking calorimeter, the Fréjus experiment considered $(B - L)$ violating nucleon decay and di-nucleon decay as well, for thirty-nine different channels [40]. Limits of order $1 - 8 \times 10^{31}$ years were established, for processes listed in Table 3.5.

Among the various alternatives to $\Delta B = \Delta L$ nucleon decay, the oscillation of a neutron into an anti-neutron remains as an intriguing possibility in some GUT models. If there exists a GUT interaction which enables a neutron to evolve into an anti-neutron, then its experimental signature in underground experiments is straightforward: The resulting anti-neutron will collide with another baryon of the parent nucleus and will annihilate to produce a relatively stationary burst of pions. In a high resolution detector the resulting signal would be unambiguous, were it not for complications arising from intranuclear rescattering of the final state pions. As with other $(B-L)$ violating processes, the current most stringent lifetime lower limit for neutron oscillation by bound nucleons is the one reported by Fréjus [41].

For a number of the $(B-L)$ non-conserving processes listed above, the tracking calorimeter technique offers no particular advantage over water Cherenkov detection. Fréjus current

Table 3.5: $(B-L)$ violating nucleon and di-nucleon decay modes and $(B-L)$ conserving di-nucleon decay modes investigated by Fréjus.

$\Delta(B-L)$ = -2	$\Delta(B-L)$ = 0
$\mathrm{n} \to \ell^- \mathrm{K}^+$ (ℓ^- = e^-, μ^+)	$\mathrm{pn} \to \ell^+ \mathrm{n}$ (ℓ^+ = e^+, μ^+)
$\mathrm{p} \to \ell^- \pi^+ \pi^+$	$\mathrm{pp} \to \ell^+ \mathrm{p}$
$\mathrm{n} \to \ell^- \pi^+ \pi^0$	$\mathrm{NN} \to \ell^+ \Delta$
$\mathrm{p} \to \ell^- \pi^+ \mathrm{K}^+$	$\mathrm{pp} \to \ell^+ \ell^+$
$\mathrm{NN} \to \pi\ \pi$	$\mathrm{pn} \to \ell^+ \overline{\nu}$

dominance for the above-listed two-body final states for example, stems from particular attention devoted to these modes rather than from superior technique. As noted previously, tracking calorimeters offer pattern recognition advantages for final states characterized by high multiplicity of tracks and showers, especially so if key tracks are below threshold for Cherenkov detection in water. Such situations arise with detection of neutron oscillation and of $(B-L)$ violating nucleon decay into three body modes and/or modes involving K^+ mesons. However for final states with multiple pions, e.g. as with neutron oscillation, these advantages are compromised somewhat by higher intranuclear rescattering rates incurred in iron compared to oxygen nuclei.

In summary, while there may be modest advantages which the tracking calorimeter technique can provide for study of $(B-L)$ non-conserving processes, these are readily offset by the order-of-magnitude increase with monitored mass achievable with water Cherenkov detection.

3.4 Nucleon Decay Sensitivity

3.4.1 Sensitivity to $p \to e^+\pi^0$

To study the sensitivity for $p \to e^+\pi^0$ searches in the UNO detector, a 20 Mt·yr exposure of atmospheric neutrinos background events is simulated and reconstructed using the Super-Kamiokande neutrino interaction and detector simulations. Three sets of simulated data are prepared with varying PMT coverage (40%, detector (A), same as Super-Kamiokande), 10%, detector (B) and 4.4%, detector (C)). With the exception of PMT coverage, the geometry for each of these simulations is identical. In the future, studies will be done using the actual UNO geometry, however, the effect of the geometry is expected to be quite small for the $p \to e^+\pi^0$ decay mode.

A large sample of $p \to e^+\pi^0$ candidate events is also generated for each of the detector options using the Super-Kamiokande proton decay Monte Carlo. Figure 3.7 shows event display of a $p \to e^+\pi^0$ Monte Carlo event for detector-(A), (B), and (C). Three showering rings caused by a positron (lower left) and two γ (upper right) from the decay of π^0 are seen

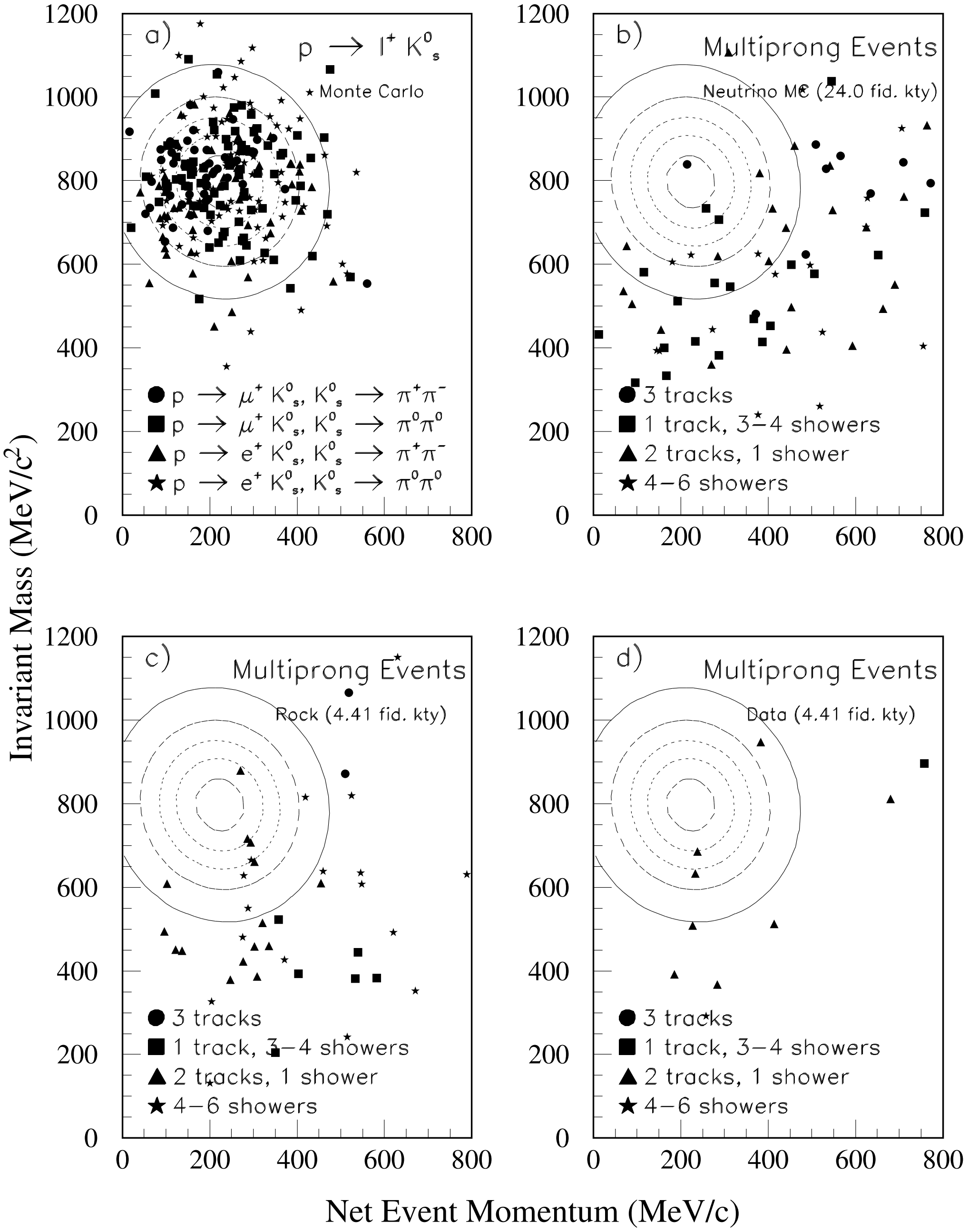

Figure 3.5: For proton decay modes p $\rightarrow \ell^+$K^0_s, the "primary" kinematic selection contour (outermost contour) together with event distributions, in the M_{inv} versus the $|\vec{p}_{net}|$ plane. Distributions show a) the proton decay simulations, b) atmospheric neutrino MC events, c) rock events, and d) data events. The μ^+K^0_s (e$^+$K^0_s) final states are depicted using solid circles and squares (triangles and stars).

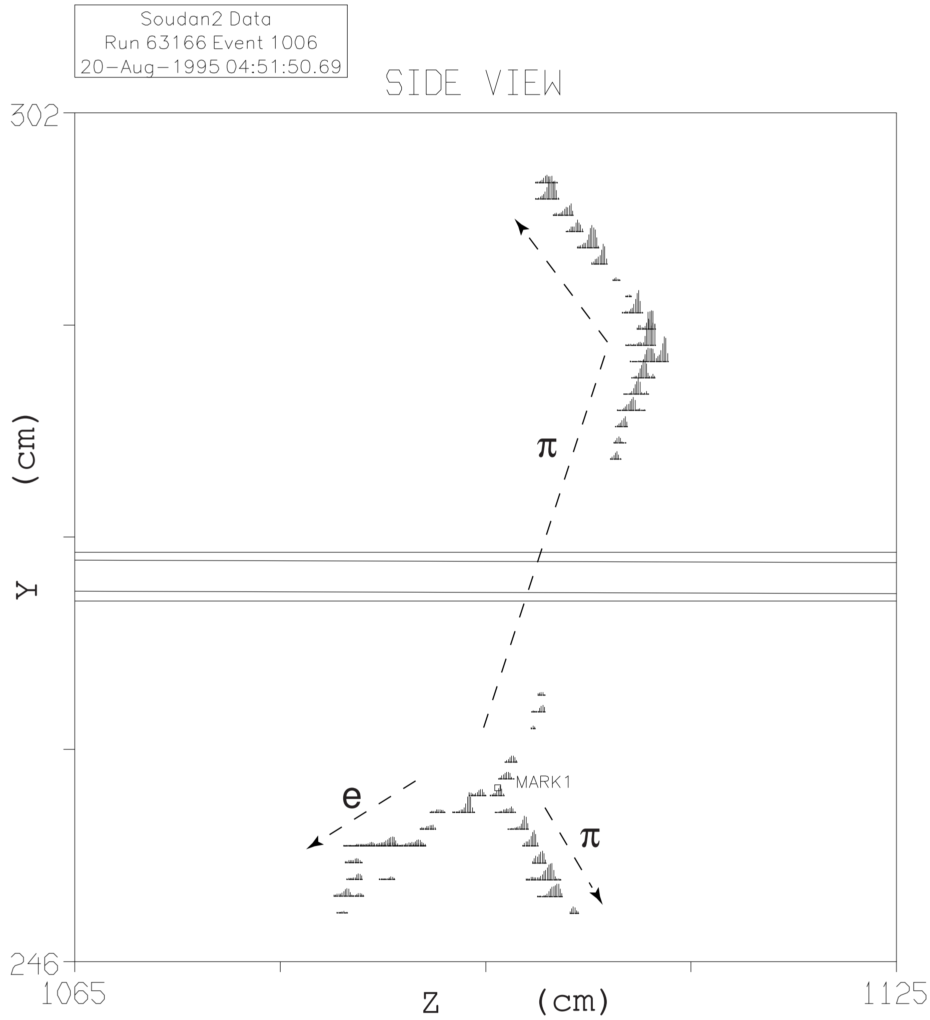

Figure 3.6: Data candidate for proton decay $\mathrm{p} \to \mathrm{e}^+\mathrm{K}^0_s$, $\mathrm{K}^0_s \to \pi^+\pi^-$, shown in the cathode ($Y$) versus drift time ($Z$) projection.

in each detector. Although Cherenkov rings become faint in (B) and (C) due to the low photo-coverage, it is possible to identify these rings.

The samples are reconstructed [42] to find the vertex position, number of Cherenkov rings, the particle type and momentum associated with each Cherenkov ring, and the number of muon decays associated with the event. The selection criteria for $p \to e^+\pi^0$ candidates in detector-(A) are; (a) the event has 2 or 3 rings, (b) all rings are e-like, (c) for three ring events, two rings have an invariant mass consistent with a π^0 decay (85 MeV/c^2 < M_{inv} < 185 MeV/c^2), (d) no muon decay signals are associated with the event, (e) the

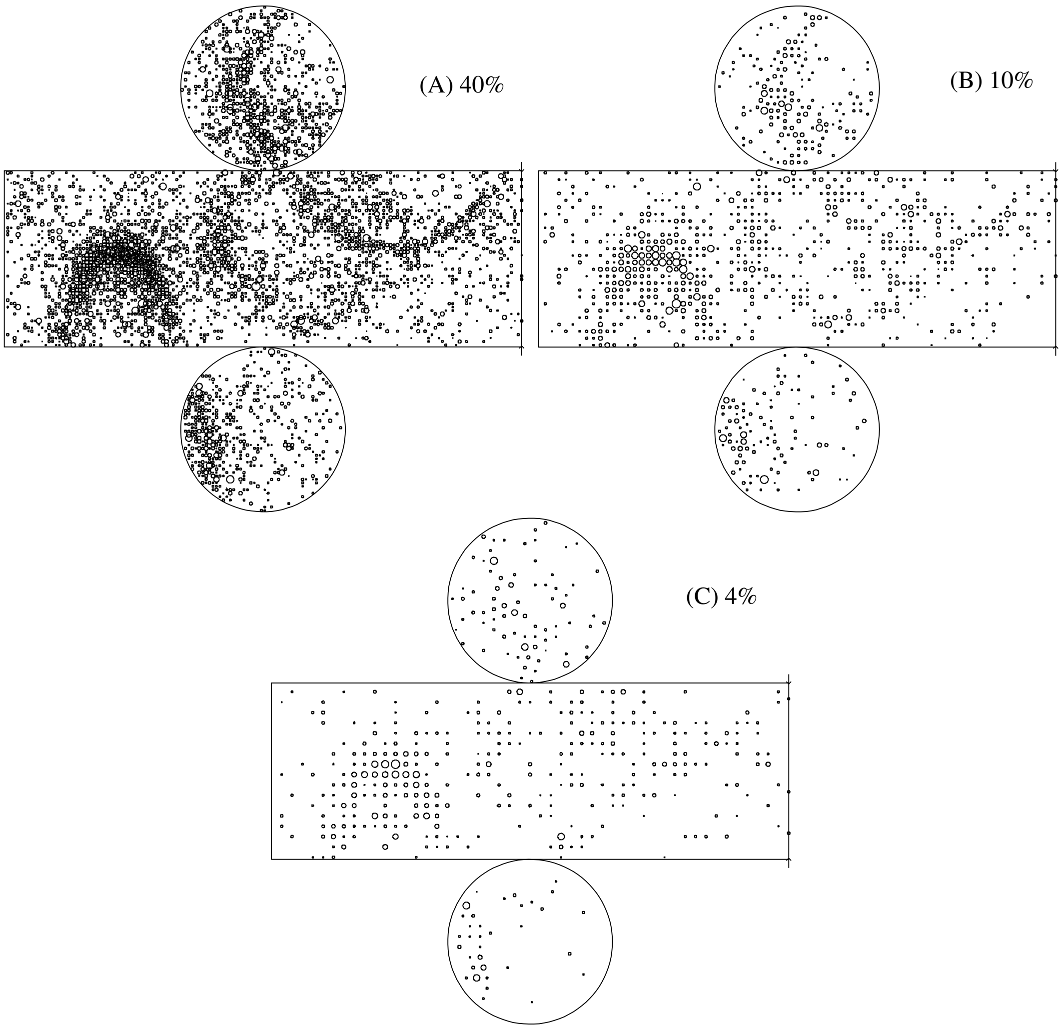

Figure 3.7: Event displays of a $p \rightarrow e^{+}\pi^{0}$ Monte Carlo event for detector-(A) with Super-Kamiokande PMT density, (B) with 1/4 PMT density, and (C) with 1/9. Small circles indicate hit PMTs with the size proportional to detected photoelectrons. Positron ring (lower left) and two γ rings (upper right) from the decay of π^{0} are seen in each detector.

total invariant mass is consistent with proton decay ($800 < M_{tot} < 1050$ MeV/c^2) and (f) the total momentum is consistent with the Fermi motion of the proton within an oxygen nucleus ($P_{tot} < 250$ MeV/c). The selection criteria are the same for detector-(B) and (C), except criteria (b) and (c) are omitted and the invariant mass cut, criterion (e), is relaxed to $750 < M_{tot} < 1050$ MeV/c^2 for the detector-(C). Using these criteria, detection efficiency for $p \rightarrow e^+\pi^0$ mode is 43% for detector (A), 32% for (B), and 21% for (C). The dominant inefficiency in detector-(A) comes from π^0 interactions in the ^{16}O nucleus where the π^0 is absorbed, scattered, or exchanges charge with a nucleon to become a charged pion. Free protons (hydrogen) are also simulated, and are the products do not undergo charge exchange interactions yielding a detection efficiency of about 90%. The primary cause of the different efficiency for (A), (B), and (C) is the performance of ring finding algorithm. The fraction of events which are reconstructed as 2 or 3-ring is 73% for (A), but only 57% (36%) for (B) and (C), respectively. However, the estimated efficiency of the ring finding algorithm for (B) and (C) is quite conservative because it has been extensively tuned assuming a 40% PMT coverage and was not re-adapted.

Figure 3.1 shows the reconstructed total momentum versus the reconstructed invariant mass distributions of the proton decay MC (left), the atmospheric neutrino MC (middle), and the Super-Kamiokande data (right) for the events which are selected by criteria (a)–(d). The shape of the distribution of data agrees well with that of the atmospheric neutrino MC. The simulated atmospheric neutrino background shown in figure 3.1 represents 20 Mt·yr Super-Kamiokande exposure and yields a background estimate of 2.25 events/Mt·yr. The background level for cases (B) and (C) is about 3 events/Mt·yr.

From the estimated background levels and detection efficiencies, proton decay sensitivity as a function of detector exposure are shown in Figure 3.8. Sensitivity is also calculated and shown in Figure 3.8 for the UNO configuration in which 40% and 10% photo-coverage detectors are combined. The sensitivities are calculated at 90% confidence level assuming Poisson processes with backgrounds [43]. With a 6 Mt·yr exposure, we would reach 1.0×10^{35} years partial lifetime.

Figure 3.9 shows expected total invariant mass distribution in detector-(A) with 20 Mt·yr exposure assuming partial proton lifetime of 1×10^{35} years. The left figure shows proton decay signals and backgrounds which pass all selection criteria except total invariant mass cut. In order to extract signals, we need to understand accurately the background. If we tighten the total momentum cut from 250 MeV/c to 100 MeV/c in order to improve signal to noise ratio, the mass distribution changes as shown in the right figure and we can observe a clear proton peak in this case. To see the sensitivity dependence on detector exposure and proton lifetime, the same distribution for different parameters is shown in Figure 3.10.

3.4.2 Sensitivity to $p \rightarrow \bar{\nu}K^+$

The $p \rightarrow \bar{\nu}K^+$ decay mode presents specific challenges in a water Cherenkov detector since both the K^+ is below the Cherenkov threshold and the neutrino is invisible. As described in the previous section the search must be performed by looking for the decay products of

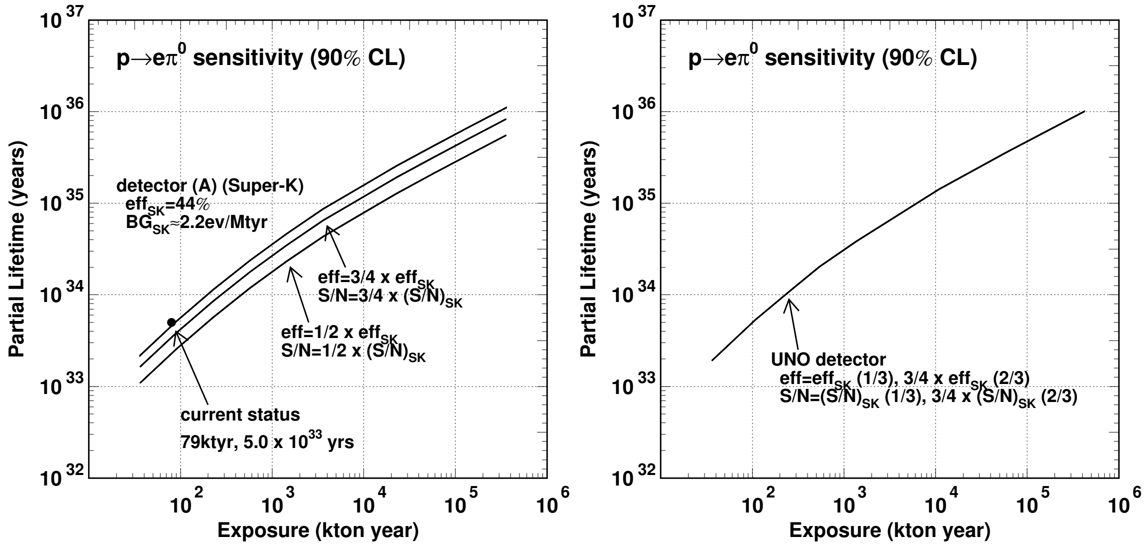

Figure 3.8: Expected sensitivity for the partial lifetime of protons. In the left figure, the sensitivity was calculated at 90% confidence level for the detector-(A) (upper line), detector-(B) (middle line), and detector-(C) (lower line). The right figure was calculated at 90% confidence level for the proposed UNO configuration.

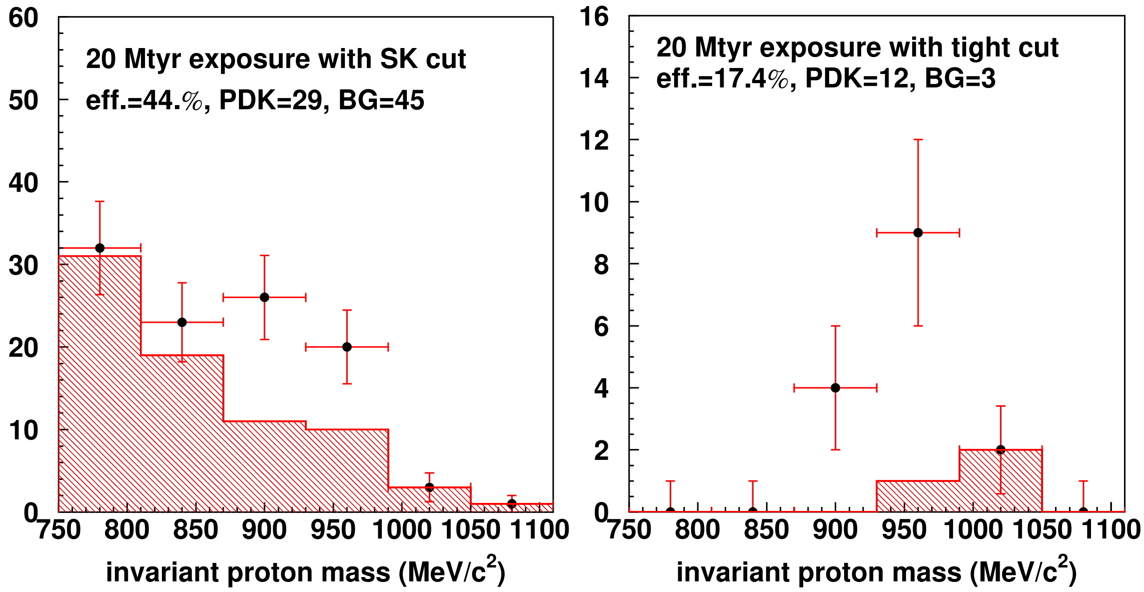

Figure 3.9: Expected invariant mass distribution of events which pass through selection criteria (a) to (e) except total mass cut. Detector exposure is 20 Mt·yr and partial proton lifetime is assumed to 1×10^{35} years. In the right figure, additional tight momentum cut of $P_{tot} < 100$ MeV/c is required to improve signal to noise ratio. A clear peak is seen at proton mass.

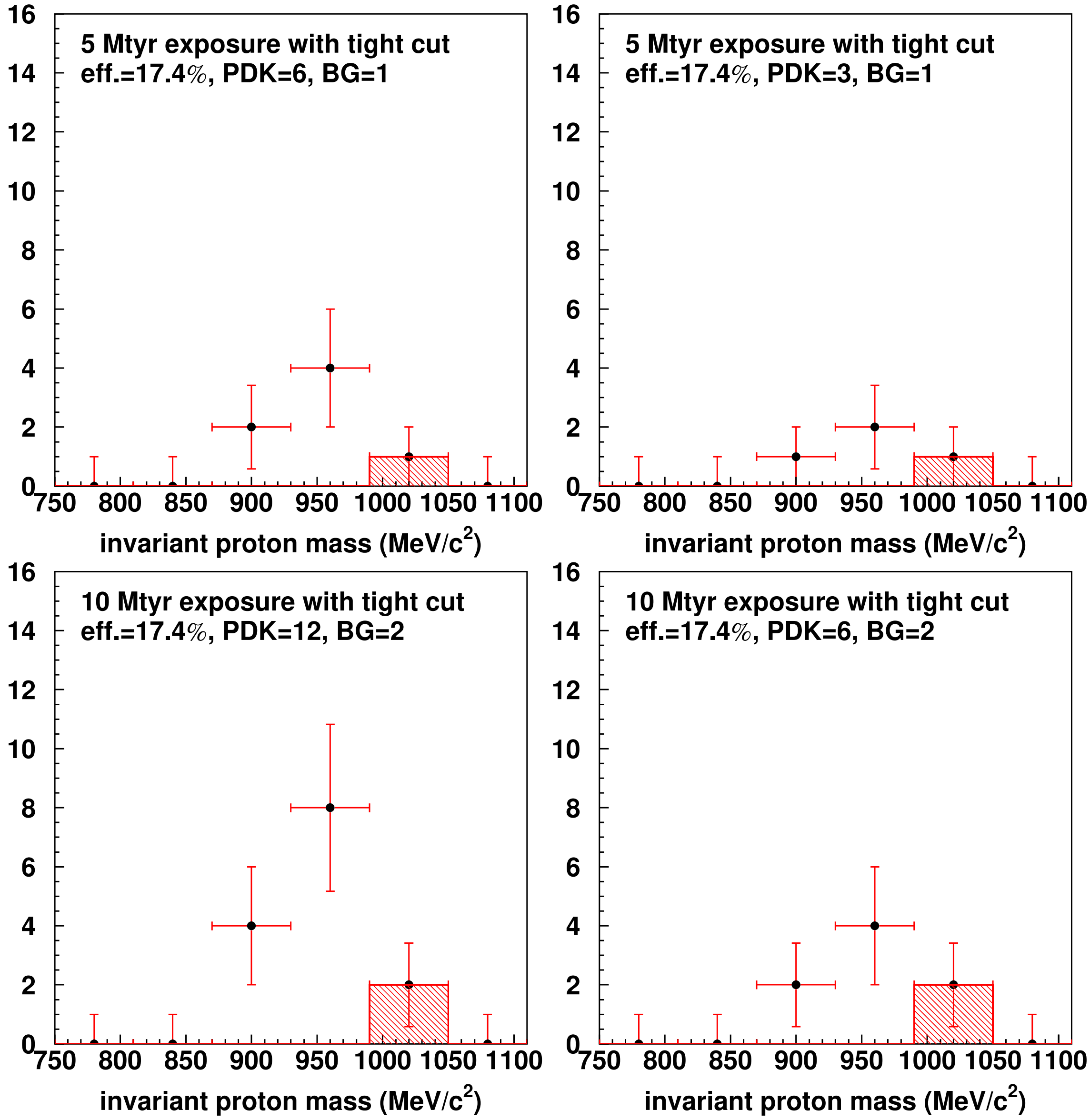

Figure 3.10: Expected invariant mass distribution for different parameter case. Top two figures and bottom two figures are in the cases of detector exposure of 5 Mt·yr and 10 Mt·yr, respectively. From left to right, partial proton lifetime is set to be 5×10^{34} and 1×10^{35} years.

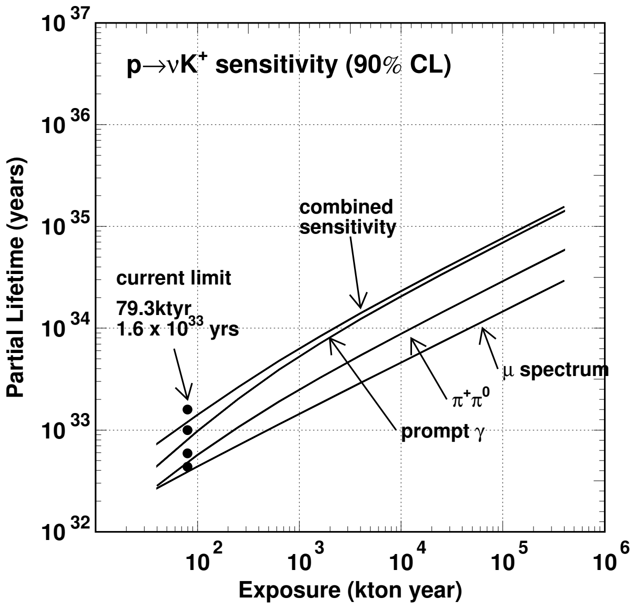

Figure 3.11: Expected sensitivity for the partial lifetime of protons for $p \to \bar{\nu}K^+$ mode. The expected sensitivity has been calculated assuming that the technical problems associated with event mis-reconstruction can be solved.

the kaon; a 236 MeV/c muon and its decay electron (method I) or 205 MeV/c π^+ and π^0 (method II). Further, since the K^+ has a finite lifetime ($\sim$ 12 ns) and the $p \to \bar{\nu}K^+$ decay leaves the product nitrogen nucleus in a highly excited state it is possible to search for the nuclear de-excitation products as well as the particles from the K^+ decay. By requiring the 6 MeV nuclear de-excitation γ as a prompt signal, the neutrino backgrounds can be significantly reduced (method III) [44].

In the Super-Kamiokande detector, the detection efficiencies for these methods, including the K^+ branching ratio, are estimated as 33%(I), 6.8%(II), and 8.8%(III) while estimated backgrounds are 2100/Mt$\cdot$yr (I), 22/Mt$\cdot$yr (II), and 6/Mt$\cdot$yr (III). Unlike the $p \to e^+\pi^0$ and $p \to \mu^+\pi^0$ modes, the dominant background for the p$\to \bar{\nu}K^+$ search using the "prompt γ" method comes from mis-reconstruction. Efforts are underway at Super-Kamiokande to reduce this problem and there is reason to be optimistic that a solution will be found. Once this is accomplished, the atmospheric neutrino interaction $\nu p \to \nu \Lambda K^+$ will become the limiting background on this mode with an expected rate of about 1 event/Mt$\cdot$yr.

Figure 3.11 shows the expected sensitivity for a $p \to \bar{\nu}K^+$ search assuming the efficiency estimated by Super-Kamiokande, and that the backgrounds due to mis-reconstructed events can be reduced. It is clear that the combined sensitivity is predominantly determined by prompt gamma search and that the ability to detect the 6 MeV γ is crucial for future $p \to \bar{\nu}K^+$ searches.

3.4.3 Experimental Determination of the Background

The evaluation of the background rate expected in UNO is critical to the design of the detector. However, the atmospheric neutrino sample collected by UNO will be several orders of magnitude large than the samples currently used to measure the neutrino cross section at neutrino energies near 1 GeV. Fortunately, the K2K one kiloton water Cherenkov detector (1KT) is collecting a data sample that will approximate a 10 Mt·yr exposure and provides an excellent opportunity. In particular, the energy spectrum of the K2K neutrino flux is quite similar to that of the atmospheric neutrino flux. Ultimately, of course, we would like to determine the reach of UNO for detecting nucleon decay. Since all possible background affect this so fundamentally, we must understand the interactions which will generate the background events in detail.

Consider the background to the $p \to e^+\pi^0$ decay mode. The Super-Kamiokande detector currently expects a background of approximately 0.2 events in this mode, and finds no candidate events. Since the number of candidate events is zero and the number of expected background is also almost zero, we can neglect uncertainty in the background in the current Super-Kamiokande analysis. However, for UNO we naively expect one background event every two years. Even assuming a relatively optimistic proton lifetime, the rate of nucleon decay events will be similar to the expected rate of background events, therefore, it is very important to understand the neutrino interactions which generate events which might be considered $p \to e^+\pi^0$ candidates. For example, taking the detection efficiency and the background of the current Super-Kamiokande $p \to e^+\pi^0$ analysis (43% efficiency and $\sim$0.2 events/79.3 kt·yr, respectively), the signal to noise ratio for a 10^{34} yr proton lifetime and a 10 Mt·yr (22 year baseline UNO) exposure will be $\sim$6. In this case for a $\sim$10 σ discovery the background uncertainty must be less than 20%.

Figure 3.12 shows the upper limit of the experimentally accessible lifetime as a function of accuracy of the background determination assuming a background rate of 3 ev/Mt·yr and exposures 1, 10, and 20 years. Not surprisingly, a precise background determinations is more important for higher exposures. For example, a $\leq$20 % accuracy is needed to benefit from exposures of more than 10 years of UNO operation. Further, the goal of UNO is conclusive detection of nucleon decay so the reduction in the uncertainty of the background estimates made possible by the 1KT data is needed to allow the full use of UNO.

The atmospheric neutrino background to the $p \to e^+\pi^0$ search mostly comes from CC ν_e ($\bar{\nu}_\mathrm{e}$) interactions where an electron (positron) and a π^0 are produced in the final state [45]. This background can be checked by studying $\nu_\mu N \to \mu\pi^0 X$ produced in the K2K beam. The K2K neutrino beam [47] is a nearly pure ν_μ beam (98.2% ν_μ, 1.3% ν_e, and 0.5% $\bar{\nu_\mu}$) with average energy $\sim$1.3 GeV as shown in Figure 3.13. The number of ν_μ interactions at 1$\sim$3 GeV for 10^{20} protons on target (pot) corresponds to about 10 Mt·yr of atmospheric ν_μ data. The statistics of the 1KT data is higher than any other previous similar beam experiments [48] by 2$\sim$3 orders of magnitude and enables us to check the neutrino interactions in detail. The neutrino energy of events where a muon and a π^0 are reconstructed in the 1KT is also shown in Figure 3.13. These $\mu\pi^0$ events cover the energy range from 0.5 to 3.0 GeV.

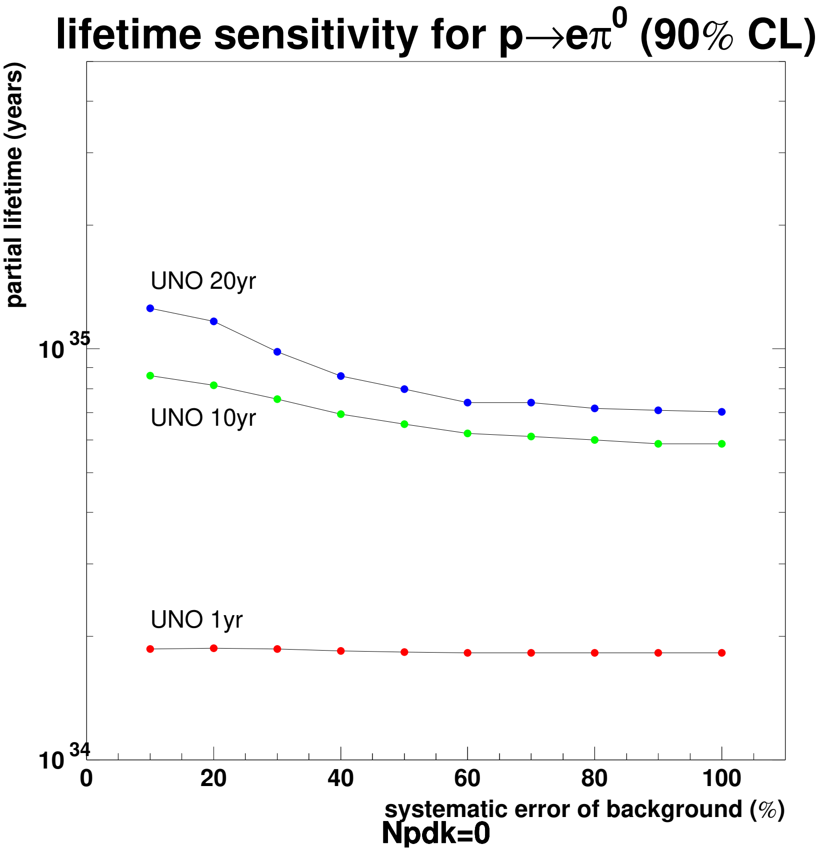

Figure 3.12: Lifetime sensitivity versus the uncertainty in the background estimation for 1, 10, 20 yr's operation of UNO. The efficiency and background found in Super-Kamiokande has been assumed.

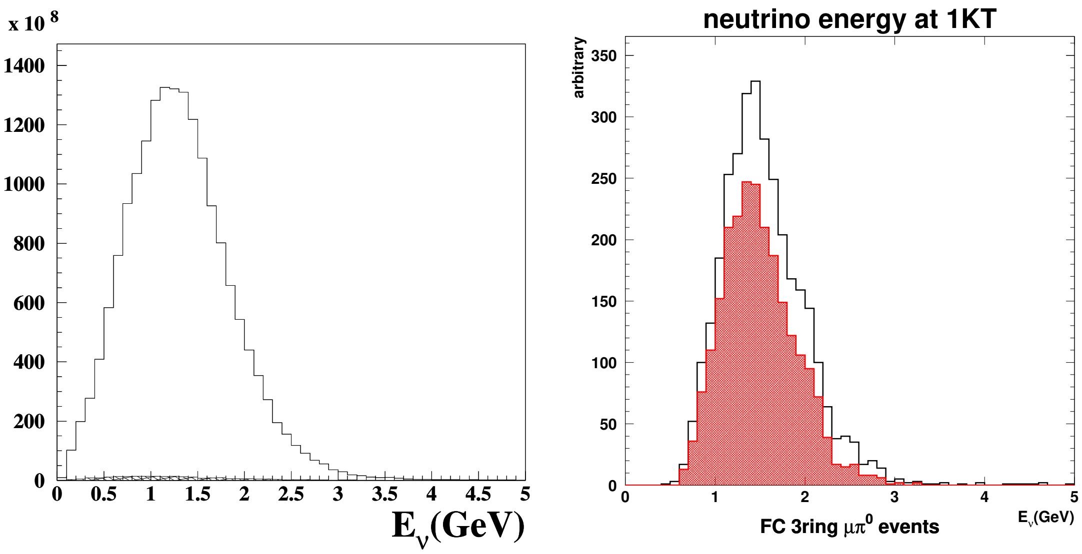

Figure 3.13: Neutrino energy of the K2K beam at the near detector (left) and neutrino energy of all $\mu\pi^0$ candidate events (right) in the 1KT. The hatched area in the left plot shows the ν_e contamination. The hatched area in the right plot shows events where a muon ($\geq$200 MeV/c) and a π^0 are in the final state.

3.4.3.1 1KT data and simulation

The data collected between January and March 2000 corresponding to $\sim 8.9 \times 10^{18}$ pot have been studied to measure the atmospheric neutrino background to proton decay searches. The $\mu^+\pi^0$ events at 1KT were selected with essentially the same cuts used in the Super-Kamiokande analysis: (1) fully contained, (2) 2 or 3 rings, (3) one "muon"-like ring and one or two "electron"-like ring (s), (4) 85 MeV/c$^2 \leq \pi^0$ mass$\leq$185 MeV/c^2 (3 ring sample). The "decay electron cut" is not applied due to the higher cosmic ray background in the 1KT, however, the efficiency of this cut is well understood for events containing a muon, and the K2K beam is primarily muon neutrinos.

An event display of a typical $\nu_\mu N \rightarrow \mu\pi^0 X$ interaction (MC) is shown in Figure 3.14. Three rings, one muon and 2 γ's from π^0 are reconstructed as "muon"-like and "electron"-like rings, respectively. The invariant mass distribution of two "e-like" rings before the π^0 mass cut (4) is also shown in Figure 3.14. There are clear peaks at the π^0 mass in both data and MC. The data and MC agree with each other very well.

Figure 3.15 shows total momentum vs. total invariant mass distributions of the $\mu\pi^0$ candidate events of 1KT data and MC ($\sim$1.2$\times$10^{19} pot), respectively. There are no events around the origin in either figure due to requiring $\geq$2000 collected photo-electrons in the 1KT analysis in order to select one neutrino interaction per beam spill. This does not affect the background study around the signal box.

The 1KT data shown here corresponds to $\sim$1 Mt$\cdot$yr and more than 10 times as much data

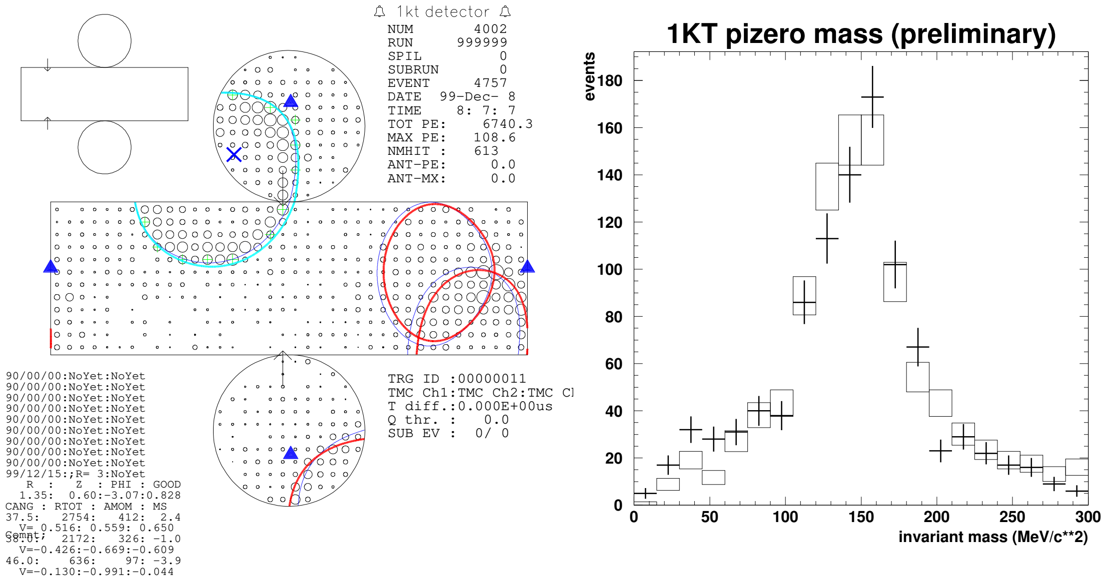

Figure 3.14: Typical event display of the $\mu\pi^0$ event (left) and invariant π^0 mass distribution for $\mu\pi^0$ candidates (right). Cross (box) shows data (MC).

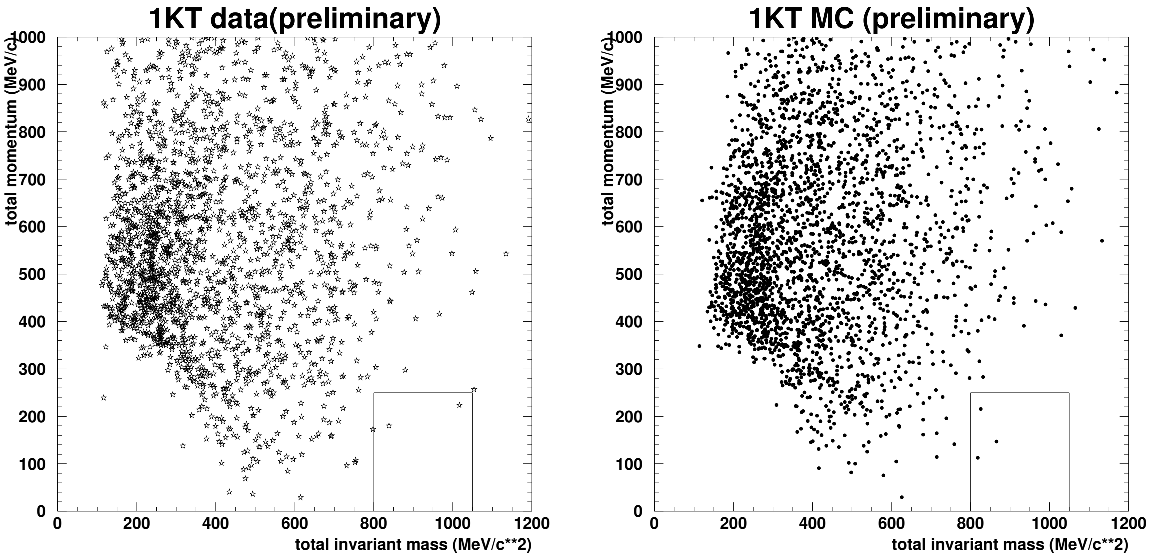

Figure 3.15: Total momentum vs. total invariant mass for $p \to \mu^+\pi^0$ candidate events of 1KT data (left) and MC (right).

(10^{20} pot) are expected within a few years. Currently, detailed studies are being performed to check the details of the agreement between the data and MC for various distributions, but Figure 3.15 clearly demonstrates that our ability to model nucleon decay background interactions is well supported by the data so far in hand.

3.5 Bibliography

[1] E.C.G. Stueckelberg, Helv. Phys. Acta.**11**, 225 (1938)

[2] E.P. Wigner, Proc. Am. Phil. Soc. **93**, 521 (1949)

[3] F. Reines, C.L. Cowen and M. Goldhaber, Phys. Rev.**D 96**, 1157 (1954)

[4] H. Georgi and S. L. Glashow, Phys. Rev. Lett. **32**, 438 (1974).

[5] K.S. Babu, J.C. Pati, and F. Wilczek, Phys. Lett. **B 423**, 337 (1998).

[6] J. Pati and A. Salam, Phys. Rev. Lett. **31**, 661 (1973); Phys. Rev. **D10**, 275 (1974).

[7] H. Georgi, in Particles and Fields, ed. C. Carlson (A.I.P., New York, 1975), p. 575; H. Fritzsch and P. Minkowski, Ann. Phys. **93**, 193 (1975).

[8] M. Gell-Mann, P. Ramond, R. Slansky, in *Supergravity*, edited by P. van Nieuwenhuizen and D. Freedman (North Holland, Amsterdam, 1979), p. 315; T. Yanagida in proceedings of *Workshop on Unified Theory and Baryon Number in the Universe*, KEK, 1979.

[9] H. Georgi and S. L. Glashow, Phys. Rev. **D6**, 429 (1972).

[10] R. Shrock, Phys. Rev. **D53**, 6465 (1996).

[11] S. Dimopoulos, S. Raby, and F. Wilczek, Phys. Rev. **D24**, 1681 (1981); I. Ibanez and G. Ross, Phys. Lett. **105B**, 439 (1981); M. Einhorn and D. R. T. Jones, Nucl. Phys. **B196**, 475 (1982); W. Marciano and G. Senjanovic, Phys. Rev. **D25**, 3092 (1982).

[12] C. Albright, K. Babu, and S. Barr, Phys. Rev. Lett. **81**, 1167 (1998) (hep-ph/9802314).

[13] C. Albright and S. Barr, Phys. Rev. Lett. **85**, 244 (2000) (hep-ph/0002155); Phys. Rev. **D62**, 093008 (2000) (hep-ph/0003251); hep-ph/0104294.

[14] K. Babu, J. Pati, and F. Wilczek, Phys. Lett. **B423**, 337 (1998); Nucl. Phys. **566**, 33 (2000) (hep-ph/9812538).

[15] N. Sakai and T. Yanagida, Nucl. Phys. **B197**, 533 (1982); S. Weinberg, Phys. Rev. **D26**, 287 (1982).

[16] S. Dimopoulos, S. Raby and F. Wilczek, Phys. Lett. **B112**, 133 (1982); J. Ellis, D. V. Nanopoulos and S. Rudaz, Nucl. Phys. **B202**, 43 (1982).

[17] K. S. Babu and S. M. Barr, Phys. Rev. **D50**, 3529 (1994); **D51**, 2463 (1995).

[18] J. Pati, Erice lectures, 2000, hep-ph/0106082.

[19] Y. Hara, S. Itoh, Y. Iwasaki, and T. Yoshie, Phys. Rev. **D34**, 3399 (1986).

[20] K. Bowler et al., Nucl. Phys. **B296**, 431 (1988).

[21] S. Aoki et al. (JLQCD Collab.), Phys. Rev. **D62**, 014506 (2000) (hep-lat/9911026).

[22] R. Dermisek, A. Mafi, and S. Raby, Phys. Rev. **D63**, 035001 (2001) (hep-ph/0007213).

[23] H. Brown et al. (Muon $g-2$ Collab.), Phys. Rev. Lett. **86**, 2227 (2001).

[24] See A. Czarnecki and W. Marciano, hep-ph/0102122; F. Jegerlehner, hep-ph/0104304, W. Marciano and B. L. Roberts, hep-ph/0105056 and references therein.

[25] K. Babu and J. Pati, Phys. Lett. **B384**, 140 (1996) (hep-ph/9606215).

[26] There is a rapidly growing literature on these models. A few of the early references are I. Antoniadis, Phys. Lett. **B246**, 377 (1990); I. Antoniadis, C. Muños, and M. Quirós, Nucl. Phys. **B397**, 515 (1993); I. Antoniadis, S. Dimopoulos, and G. Dvali, Nucl. Phys. **B516**, 70 (1998); N. Arkani-Hamed, S. Dimopoulos, and G. Dvali, Phys. Lett. **B429**, 263 (1998); I. Antoniadis, N. Arkani-Hamed, S. Dimopoulos, and G. Dvali, Phys. Lett. **B436**, 257 (1998); K. R. Dienes, E. Dudas, and T. Gherghetta, Phys. Lett. **B436**, 55 (1998); G. Shiu and S.-H.H. Tye, Phys. Rev. **D58** (1998) 106007. G.F. Giudice, R. Rattazzi and J.D. Wells, Nucl. Phys. **B544** (1999) 3; S. Nussinov and R. Shrock, Phys. Rev. **D59**, (1999) 105002; E.A. Mirabelli, M. Perelstein and M.E. Peskin, Phys. Rev. Lett. **82**, (1999) 2236.

[27] J. Hisano, hep-ph/0004266.

[28] See discussion in D.H. Perkins, Ann. Rev. Nucl. Sci. **34**, 1 (1984).

[29] A. Bueno, M. Campanelli, A. Ferrari, A. Rubbia,"Nucleon decay studies in a large liquid argon detector", Proc. NNN99 Workshop, AIP Conf. Proc. 533, Edited by M.V. Diwan and C.K. Jung, Stony Brook, New York, September 1999; p. 12.

[30] Soudan 2 Collaboration, W.W.M. Allison *et al.*, Phys. Lett. **B 427**, 217 (1998).

[31] Soudan 2 Collaboration, D. Wall *et al.*, Phys. Rev. **D 61**, 072004 (2000).

[32] Kamiokande Collaboration, K.S. Hirata *et al.*, Phys. Lett. **B 220**, 308 (1989).

[33] IMB-3 Collaboration, C. McGrew *et al.*, Phys. Rev. **D 59**, 052004 (1999).

[34] J. Learned,"Proton Decay", talk presented at the IX Int. Workshop on Neutrino Telescopes, March 2001, Venice, Italy (http://axpd24.pd.infn.it/conference2001/venice01.html).

[35] Soudan 2 Collaboration, D. Wall *et al.*, Phys. Rev. **D 62**, 092003 (2000).

[36] Fréjus Collaboration, Ch. Berger *et al.*, Nucl. Phys. **B 313**, 509 (1989).

[37] Fréjus Collaboration, Ch. Berger *al.*, Z. Phys. **C 50**, 385 (1991).

[38] R.N. Mohapatra and R.E. Marshak, Phys. Rev. Lett. **44**, 1316 (1980); Phys. Lett. **94B**, 183 (1980); Z. Chacko and R.N. Mohapatra, Phys. Rev. **D 59**, 055004 (1999).

[39] Y. Kamyshkov,"Nucleon Instability and $(B-L)$ Non-Conservation", in Proc. NNN99 Workshop, AIP Conf. Proc. 533, Edited by M.V. Diwan and C.K. Jung, Stony Brook, New York, September 1999; p. 84.

[40] Frèjus Collaboration, Ch. Berger *et al.*, Phys. Lett. **B 269**, 227 (1991).

[41] Frèjus Collaboration, Ch. Berger *et al.*, Phys. Lett. **B 240**, 237 (1989).

[42] M. Shiozawa *et al.*, *Phys. Rev. Lett.* **81**, 3319 (1998).

[43] Particle Data Group, *Phys. Rev.* **D50**, 1281 (1994).

[44] Y. Totsuka, *7th Workshop on Grand Unification, ICOBAN '86*, (World Scientific, 1986), p. 118.

[45] M.Shiozawa, "Feasibility study on 1 Mton water Cherenkov detector II", 7-Aug.-2000, NNN00-Fermilab.

[46] Y.Hayato *et al.*, Phys. Rev. Lett. **83**, 1529 (1999).

[47] H.Noum *et al.*, Nucl.Instr. and Meth. **A398**, 399 (1997).
M.Ieiri *et al.*, Proc. 1st Asian Particle Accelerator Conference(1998).
S.H.Ahn et al, hep-ex/0103001, submitted to Phys.Lett.B.

[48] G.Battistoni *et al.*, Nucl. Instr. Meth. **A219**, 300 (1984).
W.A.Mann, *et al.*, Phys. Rev. **D34**, 2545 (1986).
C.Berger *et al.*, Nucl. Instr. Meth. **A302**, 406 (1991).

Chapter 4

Neutrino Physics

4.1 Overview

4.1.1 Evidence for Neutrino Oscillation

While in the framework of the Standard Model, one assumes zero neutrino masses, in a modern theoretical context one expects nonzero neutrino masses and associated lepton mixing. Experimentally, there has been accumulating evidence for such masses and mixing.

Strong observational evidence for neutrino oscillations is the atmospheric neutrino anomaly, observed by Kamiokande [1], IMB [2], Super-Kamiokande [3] with the highest statistics, and by Soudan 2 [4] and MACRO [5]. This data can be fit by $\nu_\mu \to \nu_x$ oscillations with $\Delta m^2_{atm} \sim 3 \times 10^{-3}$ eV^2 [3] and maximal mixing $\sin^2 2\theta_{atm} \approx 1$. The identification $\nu_x = \nu_\tau$ is preferred over $\nu_x = \nu_{sterile}$, and the identification $\nu_x = \nu_e$ is excluded by both the Super-Kamiokande data and the CHOOZ experiment [7].

All solar neutrino experiments (Homestake, Kamiokande, Super-Kamiokande, SAGE, and GALLEX) show a significant deficit in the neutrino fluxes coming from the Sun [8]. This deficit can be explained by oscillations of the ν_e's into other weak eigenstate(s), with Δm^2_{sol} of the order 10^{-5} eV^2 for solutions involving the Mikheev-Smirnov-Wolfenstein (MSW) resonant matter oscillations [9, 10] or of the order of 10^{-10} eV^2 for vacuum oscillations.

In addition, the LSND experiment [11] has reported observing $\bar{\nu}_\mu \to \bar{\nu}_e$ and $\nu_\mu \to \nu_e$ oscillations with $\Delta m^2_{LSND} \sim 0.1$–$1$ eV^2 and a range of possible mixing angles, depending on Δm^2_{LSND}. This result is not confirmed, but also not completely ruled out, by a similar experiment, KARMEN [12]. The MiniBOONE experiment at Fermilab is designed to resolve this issue.

If one were to try to fit all of these experiments, then, since they involve three different values of $\Delta m^2_{ij} = m(\nu_i)^2 - m(\nu_j)^2$ which could not satisfy the identity for three neutrino species,

$$\Delta m^2_{32} + \Delta m^2_{21} + \Delta m^2_{13} = 0 \tag{4.1}$$

it would follow that one would have to introduce further neutrino(s). Since there are only three leptonic weak doublets and associated light neutrinos with weak isosopin $I = 1/2$ and

$I_3 = 1/2$ from the measurement of the Z width, it follows that such further neutrino weak eigenstate(s) would have to be electroweak singlet(s) ("sterile" neutrinos). We choose here to consider only the (confirmed) solar and atmospheric neutrino data, and to work in the context of three active neutrino weak eigenstates.

4.1.2 Neutrino Oscillation Formalism

In this simplest theoretical context, there are three electroweak-doublet neutrinos. Although electroweak-singlet neutrinos may be present in the theory, one expects that, since their bare mass terms are electroweak singlet operators, the associated masses should not have any close relation with the electroweak symmetry breaking scale and, from a top-down point of view such as a grand unified theory, should be much larger than this scale. If this is the case, then the neutrino mixing can be described by the matrix

$$U = \begin{pmatrix} c_{12}c_{13} & c_{13}s_{12} & s_{13}e^{-i\delta} \\ -c_{23}s_{12} - s_{13}s_{23}c_{12}e^{i\delta} & c_{12}c_{23} - s_{12}s_{13}s_{23}e^{i\delta} & c_{13}s_{23} \\ s_{12}s_{23} - s_{13}c_{12}c_{23}e^{i\delta} & -s_{23}c_{12} - s_{12}c_{23}s_{13}e^{i\delta} & c_{13}c_{23} \end{pmatrix} K' \tag{4.2}$$

where $c_{ij} = \cos\theta_{ij}$, $s_{ij} = \sin\theta_{ij}$, and $K' = diag(1, e^{i\phi_1}, e^{i\phi_2})$. The phases ϕ_1 and ϕ_2 do not affect neutrino oscillations. Thus, in this framework, the neutrino mixing relevant for neutrino oscillations depends on the four angles θ_{12}, θ_{13}, θ_{23}, and δ, and on two independent differences of squared masses, $\Delta m^2_{atm.}$, which is $\Delta m^2_{32} = m(\nu_3)^2 - m(\nu_2)^2$ in the favored fit, and $\Delta m^2_{sol.}$, which may be taken to be $\Delta m^2_{21} = m(\nu_2)^2 - m(\nu_1)^2$. Note that these quantities involve both magnitude and sign; although in a two-species neutrino oscillation in vacuum the sign does not enter, in the three species oscillations relevant here, and including both matter effects and CP violation, the signs of the Δm^2 quantities do enter and can, in principle, be measured.

For our later discussion it will be useful to record the formulae for the various relevant neutrino oscillation transitions. In the absence of any matter effect, the probability that a (relativistic) weak neutrino eigenstate ν_a becomes ν_b after propagating a distance L is

$$\begin{aligned} P(\nu_a \to \nu_b) &= \delta_{ab} - 4 \sum_{i>j=1}^{3} Re(K_{ab,ij}) \sin^2\Big(\frac{\Delta m^2_{ij} L}{4E}\Big) + \\ &+ 4 \sum_{i>j=1}^{3} Im(K_{ab,ij}) \sin\Big(\frac{\Delta m^2_{ij} L}{4E}\Big) \cos\Big(\frac{\Delta m^2_{ij} L}{4E}\Big) \end{aligned} \tag{4.3}$$

where

$$K_{ab,ij} = U_{ai} U^*_{bi} U^*_{aj} U_{bj} \tag{4.4}$$

and

$$\Delta m^2_{ij} = m(\nu_i)^2 - m(\nu_j)^2 \tag{4.5}$$

Recall that in vacuum, CPT invariance implies $P(\bar\nu_b \to \bar\nu_a) = P(\nu_a \to \nu_b)$ and hence, for $b = a$, $P(\bar\nu_a \to \bar\nu_a) = P(\nu_a \to \nu_a)$. For the CP-transformed reaction $\bar\nu_a \to \bar\nu_b$ and the

T-reversed reaction $\nu_b \to \nu_a$, the transition probabilities are given by the right-hand side of (4.3) with the sign of the imaginary term reversed. (Below we shall assume CPT invariance, so that CP violation is equivalent to T violation.)

In most cases there is only one mass scale relevant for long-baseline neutrino oscillations, $\Delta m^2_{atm} \sim$ few $\times\, 10^{-3}$ eV^2 and one possible neutrino mass spectrum is the hierarchical one

$$\Delta m^2_{21} = \Delta m^2_{sol} \ll \Delta m^2_{31} \approx \Delta m^2_{32} = \Delta m^2_{atm} \tag{4.6}$$

In this case, CP (T) violation effects are negligible small, so that in vacuum

$$P(\bar{\nu}_a \to \bar{\nu}_b) = P(\nu_a \to \nu_b) \tag{4.7}$$

$$P(\nu_b \to \nu_a) = P(\nu_a \to \nu_b) \tag{4.8}$$

In the absence of T violation, the second equality (4.8) would still hold in uniform matter, but even in the absence of CP violation, the first equality (4.7) would not hold. With the hierarchy (4.6), the expressions for the specific oscillation transitions are

$$\begin{aligned} P(\nu_\mu \to \nu_\tau) &= 4|U_{33}|^2|U_{23}|^2 \sin^2\Big(\frac{\Delta m^2_{atm} L}{4E}\Big) \\ &= \sin^2(2\theta_{23}) \cos^4(\theta_{13}) \sin^2\Big(\frac{\Delta m^2_{atm} L}{4E}\Big) \end{aligned} \tag{4.9}$$

$$\begin{aligned} P(\nu_e \to \nu_\mu) &= 4|U_{13}|^2|U_{23}|^2 \sin^2\Big(\frac{\Delta m^2_{atm} L}{4E}\Big) \\ &= \sin^2(2\theta_{13}) \sin^2(\theta_{23}) \sin^2\Big(\frac{\Delta m^2_{atm} L}{4E}\Big) \end{aligned} \tag{4.10}$$

$$\begin{aligned} P(\nu_e \to \nu_\tau) &= 4|U_{33}|^2|U_{13}|^2 \sin^2\Big(\frac{\Delta m^2_{atm} L}{4E}\Big) \\ &= \sin^2(2\theta_{13}) \cos^2(\theta_{23}) \sin^2\Big(\frac{\Delta m^2_{atm} L}{4E}\Big) \end{aligned} \tag{4.11}$$

For sufficiently small θ_{13} and sufficiently large $\sin^2 2\theta_{12}$ and Δm^2_{21}, corrections to this hierarchical one-Δm^2 approximation can be significant [6].

In neutrino oscillation searches using reactor antineutrinos, i.e. tests of $\bar{\nu}_e \to \bar{\nu}_e$, the two-species mixing hypothesis used to fit the data is

$$\begin{aligned} P(\nu_e \to \nu_e) &= 1 - \sum_x P(\nu_e \to \nu_x) \\ &= 1 - \sin^2(2\theta_{reactor}) \sin^2\Big(\frac{\Delta m^2_{reactor} L}{4E}\Big) \end{aligned} \tag{4.12}$$

where $\Delta m^2_{reactor}$ is the squared mass difference relevant for $\bar{\nu}_e \to \bar{\nu}_x$. In particular, in the upper range of values of Δm^2_{atm}, since the transitions $\bar{\nu}_e \to \bar{\nu}_\mu$ and $\bar{\nu}_e \to \bar{\nu}_\tau$ contribute to $\bar{\nu}_e$ disappearance, one has

$$P(\nu_e \to \nu_e) = 1 - \sin^2(2\theta_{13}) \sin^2\Big(\frac{\Delta m^2_{atm} L}{4E}\Big) \tag{4.13}$$

i.e., $\theta_{reactor} = \theta_{13}$, and, for the value $|\Delta m^2_{32}| = 3 \times 10^{-3}$ from Super-Kamiokande, the CHOOZ experiment on $\bar{\nu}_e$ disappearance yields the upper limit [7]

$$\sin^2(2\theta_{13}) < 0.1 \tag{4.14}$$

which is also consistent with conclusions from the Super-Kamiokande data analysis [3].

Further, the quantity "$\sin^2(2\theta_{atm})$" often used to fit the data on atmospheric neutrinos with a simplified two-species mixing hypothesis, is, in the three-generation case,

$$\sin^2(2\theta_{atm}) \equiv \sin^2(2\theta_{23}) \cos^4(\theta_{13}) \tag{4.15}$$

The Super-Kamiokande experiment finds that the best fit to their data is to infer $\nu_\mu \to \nu_\tau$ oscillations with maximal mixing, and hence $\sin^2(2\theta_{23}) = 1$ and $|\theta_{13}| << 1$. The various solutions of the solar neutrino problem involve quite different values of Δm^2_{21} and $\sin^2(2\theta_{12})$: (i) large mixing angle solution, LMA: $\Delta m^2_{21} \simeq \text{few} \times 10^{-5}$ eV^2 and $\sin^2(2\theta_{12}) \simeq 0.8$; (ii) small mixing angle solution, SMA: $\Delta m^2_{21} \sim 10^{-5}$ and $\sin^2(2\theta_{12}) \sim 10^{-2}$, (iii) LOW: $\Delta m^2_{21} \sim 10^{-7}$, $\sin^2(2\theta_{12}) \sim 1$, and (iv) "just-so": $\Delta m^2_{21} \sim 10^{-10}$, $\sin^2(2\theta_{12}) \sim 1$. The Super-Kamiokande experiment favors the LMA solutions [8].

4.1.3 Relevant Near- and Mid-Term Experiments

There are currently intense efforts to confirm and extend the evidence for neutrino oscillations in all of the various sectors—solar, atmospheric, and accelerator. Some of these experiments are running; in addition to Super-Kamiokande and Soudan-2 (until July 2001), these include the Sudbury Neutrino Observatory SNO, and the K2K long-baseline experiment between KEK and Kamioka. Others are in development and testing phases, such as BOONE, MINOS, the CERN - Gran Sasso program, KamLAND, and Borexino [13]. Among the long-baseline neutrino oscillation experiments, the approximate distances are $L \simeq 250$ km for K2K, 730 km for both MINOS, from Fermilab to Soudan and the proposed CERN-Gran Sasso experiments. K2K is a ν_μ disappearance experiment with a conventional neutrino beam having a mean energy of about 1.4 GeV, going from KEK to the Super-Kamiokande detector. It has a near detector for beam calibration. It has obtained results consistent with the Super-Kamiokande experiment, and has reported that its data disagrees by 2σ with the no-oscillation hypothesis [14]. MINOS is another conventional neutrino beam experiment that takes a beam from Fermilab to a detector in the Soudan mine in Minnesota. It again uses a near detector for beam flux measurements and has opted for a low-energy configuration, with the flux peaking at about 3 GeV. This experiment expects to start taking data in early 2005 and, after some years of running, to obtain higher statistics than the K2K experiment and to achieve a sensitivity down to roughly to the level $|\Delta m^2_{32}| \sim 10^{-3}\mathrm{eV}^2$. The CERN - Gran Sasso program is also planned to start around 2005. It will involve taking a higher energy neutrino beam from CERN to the Gran Sasso deep underground laboratory in Italy. This program will emphasize detection of the τ's produced by the ν_τ's that result from the inferred neutrino oscillation transition $\nu_\mu \to \nu_\tau$. The OPERA experiment will do this using emulsions [15], while the ICARUS proposal uses a liquid argon chamber [16]. The Japan Hadron Facility (JHF), also called the High Intensity Proton Accelerator (HIPA), plans to use a 1 MW proton driver to produce a high-intensity conventional neutrino beam with a pathlength 300 km to the Super-Kamiokande detector [17]. Moreover, at Fermilab, the MiniBOONE experiment plans to run in the next few years and to confirm or refute the LSND claim after a few years of running.

There are also several relevant solar neutrino experiments. The SNO experiment is currently running and should report their first results in summer, 2001. These will involve measurement of the solar neutrino flux and energy distribution using the charged current reaction on heavy water, $\nu_e + d \to e + p + p$ (addendum: within a week prior to the publication of this paper, the SNO collaboration announced that they had seen the evidence of ν_e oscillation to ν_μ, ν_τ. Their results were obtained by measuring the CC rate of ν_e interaction with deutron in heavy water and comparing it to the Super-Kamiokande precision measurement of the total elastic scattering rate of the solar neutrinos on electrons in water. The results strongly favors at 3 σ level $\nu_e \to \nu_\mu, \nu_{tau}$ transition to $\nu_e \to \nu_s$). Subsequently, they will measure the neutral current reaction $\nu_e + d \to \nu_e + n + p$. The KamLAND experiment in Japan expects to begin taking data in late 2001. This is a reactor antineutrino experiment using baselines of order 100 - 250 km and will search for $\bar{\nu}_e$ disappearance. On a similar time scale, the Borexino experiment in Gran Sasso expects to measure the ^{7}Be neutrinos from the sun. These experiments should help to decide which of the various solutions to the solar neutrino problem is preferred, and hence the corresponding values of Δm^2_{21} and $\sin^2(2\theta_{12})$.

This, then, is the program of relevant experiments during the period 2000–2010. By the end of this period, we may expect that much will have been learned about neutrino masses and mixing. However, there will remain several quantities that will not be well measured and which can be measured by UNO.

4.2 Atmospheric Neutrinos

Our current knowledge concerning neutrino oscillation phenomena has benefitted extensively from measurements of atmospheric neutrinos carried out using the Super-Kamiokande water Cherenkov detector. Among the crucial insights which have resulted from the study of the atmospheric fluxes using Super-Kamiokande, we may cite:

1. Compelling evidence for anomalous depletion of muon neutrinos with zenith angles at and below horizon at sub-GeV and multi-GeV neutrinos.

2. Strong evidence that the depletion exhibits the dependence in L/E which is predicted for neutrino two-state mixing.

3. Delineation of allowed regions for the mixing angle and Δm^2 values which characterize this mixing of the ν_μ flavor state with another flavor state.

4. Evidence, in conjunction with the reactor experiments, that the predominant atmospheric oscillation mode is not ν_μ to ν_{e}.

5. Observations which discriminate against ν_μ to ν_{s} as the dominant two-state oscillation; these same observations are completely consistent with ν_μ to ν_τ predominance.

6. Evidence for a contribution arising from charged current ν_τ interactions among inclusive distributions inferred using multi-GeV neutrino events.

7. Observation of the "East-West effect", a signature asymmetry in zenith angles of both ν_μ and ν_{e} fluxes arriving at the underground site. This observation provides strong evidence that treatment of geomagnetic effects in atmospheric neutrino flux calculations is essentially correct.

We regard Super-Kamiokande to be a prototype UNO detector from which guidelines may be inferred when considering new physics possibilities which may arise with UNO measurements of atmospheric neutrinos.

The new feature which UNO will introduce to the study of atmospheric neutrino physics is truly colossal event statistics for each and every atmospheric event sample, e.g. for the fully contained (FC) sub-GeV and multi-GeV mu-like and e-like samples, for the FC multi-ring flavor-tagged samples, for the partially contained (PC) ν_μ sample, for the up-stopping muons sample, and for the through-going muons sample. The UNO program will result in exposures rated in multiple megaton-years; atmospheric neutrino samples for analysis will 20 to 40-fold larger than those currently available in Super-Kamiokande.

These high statistics event samples will materialize in a milieu wherein knowledge of neutrino oscillations will be considerably farther advanced than at present. We then consider how UNO atmospheric samples might be analyzed to best advantage.

4.2.1 Direct Observation of the Oscillation Pattern

The Super-Kamiokande experiment has presented compelling evidence for muon neutrino disappearance. This anomaly is generally explained as evidence for neutrino oscillation from ν_μ to ν_τ or ν_{s}, however, the data set cannot exclude the possibility that the observed behavior is of some other form. In fact, several models [18] have been proposed where the expected disappearance of ν_μ as function of L/E will be of the form $e^{-\alpha \cdot L/E}$ where α is determined by the model. The oscillatory nature of the disappearance can be explicitly demonstrated by observing the disappearance and regeneration of the ν_μ flux as a function of L/E.

Table 4.1: The assumed detector resolution of UNO for various processes.

Muon Angular Resolution	$4°$
Hadronic Shower Angular Resolution	$10°$
Muon Energy Resolution	$3\% + 1.5\%/\sqrt{\text{GeV}}$
Hadronic Shower Energy Resolution	$9\% + 30\%/\sqrt{\text{GeV}}$

One of the primary difficulties for distinguishing oscillatory from exponential disappearance of ν_μ is that the disappearance is occurring at values of L/E which correspond to events coming from near the horizon. This is simply a result of the energy response of the detector coupled with the relevant Δm^2 range and is not at all surprising as the flight path of neutrinos changes most rapidly for zenith angles near horizontal. In a detector which can measure the energy of muons over a very wide dynamic range, a sample of muons can be selected where the L/E of the expected first oscillation will not occur near the horizon. This will result in the detector having a sufficient resolution to rule out (or confirm) a wide variety of neutrino decay models and has the possibility to dramatically confirm the neutrino oscillation hypothesis.

The limited dynamic range of the energy acceptance for high energy muons has prevented Super-Kamiokande from directly observing the oscillatory (or exponential) nature of the ν_μ disappearance. In the proposed UNO detector muons of up to 36 GeV will be fully contained. In the smallest dimension, a 12 GeV muon will be fully contained which is comparable to the maximum muon energy which can be fully contained in the Super-Kamiokande detector. This improved energy acceptance will enable UNO to test the oscillatory nature of the muon neutrino disappearance seen by Super-Kamiokande.

4.2.1.1 Experimental Sensitivity to L/E

The sensitivity of the UNO detector has been studied assuming detector resolutions similar to those found in Super-Kamiokande (summarized in table 4.1).

The muon angular resolution is taken to be $4°$ about the true direction of the muon. This is well matched to the low energy muon track reconstruction in Super-Kamiokande and is much worse than the high energy reconstruction where the angular resolutions approach $1°$. The hadronic shower angular resolution is taken to be $10°$ about the initial direction of the hadron. Typical events used in this analysis have more than 1 GeV of energy carried by hadrons generated in the neutrino interaction. These hadrons will appear as hadronic showers.

Muon events with relatively high energies are selected so that the direction of the neutrino can be reconstructed with an acceptable accuracy. The neutrino direction, and hence the L/E, is better estimated for higher energy events, however the L/E for low energy events with directions far from the horizontal is estimated with sufficient accuracy for use in this analysis.

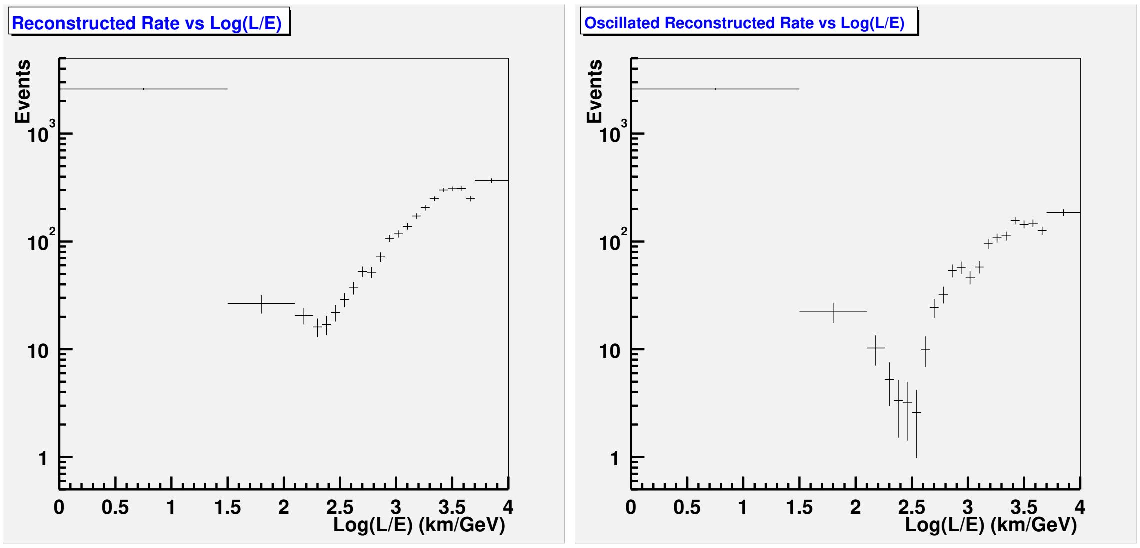

Figure 4.1: The number of events as a function of L/E assuming a 2830 kt·yr exposure ($\sim$7 yr) in the straw-man detector). The left plot shows the expected distribution in absence of oscillations. The right plot shows the effect of oscillations. The oscillated event rate assumes the oscillation parameters are Δm^2=0.003 eV^2, and $\sin^2 2\theta$=1.

Events resulting from lower energy neutrinos traveling vertically are either oscillated to equilibrium (up-going), or have not traveled far enough to have a significant oscillation probability (down-going). These events provide a baseline to compare against the behavior in the transition region.

A high energy muon is required in each event. This requirement is present so that the detector will be able to determine the presence of the muon with high efficiency and with a small probability of confusion. If the muon has a momentum of greater than 1 GeV/c then it can be identified based on its path length through the water. If an event contains a muon with less than 1 GeV/c of momentum, but the muon carries more than half the visible energy of the event then it can be identified using the same method used by Super-Kamiokande.

In order to observe the oscillatory nature of the ν_μ disappearance, it is essential to accurately reconstruct the L/E of the neutrino which generated each event. The neutrino direction is assumed to be the same as the event direction, and neutrino interaction kinematics dominate the uncertainty in the reconstructed neutrino direction. Unfortunately, the path-length varies quite rapidly for directions near the horizontal and small uncertainties in the neutrino direction can lead to large uncertainties in the neutrino path-length. For this reason, only events with reconstructed zenith angles far from horizontal are used. The criterion for inclusion in the analysis is that a 3σ variation in the reconstructed neutrino direction will result in less than a factor of 2 uncertainty in the reconstructed path-length which has the effect of selecting event well away from the horizontal.

Figure 4.1 shows the expected distribution of events as a function of reconstructed L/E

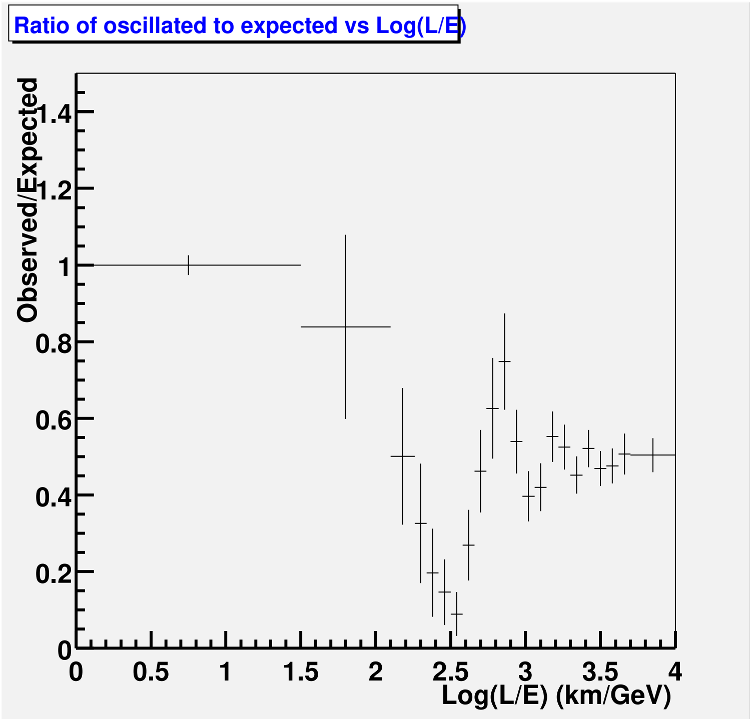

Figure 4.2: The ratio of the oscillated muon event rate to the expected rate as a function of L/E assuming a 2830 kt·yr exposure ($\sim$7 yr in the straw-man detector). The oscillated flux assumes the parameters are Δm^2=0.003 eV^2, and $\sin^2 2\theta$=1.

for a 7 yr exposure of the proposed UNO detector. The left plot shows the distribution in the absence of neutrino oscillation and displays the expected shape due to phase space considerations. The region around $L/E = 10$ is generally populated by events coming from near the horizon where the neutrino path-length is changing rapidly as a function of angle. The region is further depleted by the selection criterion which eliminates events with a poor L/E resolution. The events which finally populated this region have very high energies. The right plot shows the effect of oscillations on the expected signal where the oscillation parameters have been assumed to be Δm^2=0.003 eV^2 and $\sin^2 2\theta$=1. It should be noted that this analysis will become more sensitive if the value of Δm^2 is smaller than expected. The ratio of the oscillated muon event rate to the expected rate as a function of L/E is shown in Figure 4.2. A clear neutrino oscillation signature (assuming Δm^2=0.003 eV^2 and $\sin^2 2\theta$=1) is evident in the atmospheric flux arriving from below the horizon as a dip at $\mathrm{Log}(L/E) \sim 2.5$.

In summary, the UNO detector will have a sufficient energy response and resolution to unambiguously observe the first cycle of neutrino oscillations, or to demonstrate the observed effect is due to an exponential disappearance of muon neutrinos.

4.2.2 Search for ν_τ Appearance

The Super-Kamiokande experiment disfavors $\nu_\mu \rightarrow \nu_s$ as an explanation for the atmospheric neutrino zenith angle distributions. the Super-Kamiokande group has begun a search for the appearance of ν_τ charged current interactions. Given full mixing, and assuming two component mixing, approximately one ν_τ charged current event is expected per kiloton-year of exposure. In the current sample this corresponds to approximately 80 events, this combined with a relatively low reconstruction efficiency ($< 50\%$) and relatively high backgrounds limit the capability of Super-Kamiokande to make a significant statement about ν_τ appearance. The situation will be much better for UNO, with the primary improvement coming from the increased exposure.

The Super-Kamiokande experiment has performed three independent, but statistically correlated searches for τ appearance. These analyses have similar backgrounds levels and efficiencies, yielding measurements consistent with the expectation from $\nu_\mu \rightarrow \nu_\tau$ oscillations. After a 70 kiloton-yr exposure the excess is almost two standard deviations above the level expected in the absence of ν_τ appearance [42]. Assuming that the backgrounds, efficiencies and systematic errors for UNO are similar to those found in Super-Kamiokande, the UNO detector will expect more than a three standard deviation excess after a one year exposure (400 kiloton year).

4.2.3 Global Oscillation Fits

New physics can be gleaned from the high statistics atmospheric samples of UNO by invoking "global" fits for three-state neutrino mixing which utilize all samples simultaneously and which incorporate the (future) extensive knowledge of concerning three-state mixing. The UNO global fits will provide extensive new checks of flux calculations which are based on 3-dimensional models of the atmosphere. UNO, since it will likely be situated at a site which has a distinctly lower geomagnetic cutoff than Kamioka, will provide new and different measurements for azimuthal flux dependences and for modulation of sub-GeV neutrino fluxes with the solar cycle. The global fits of UNO will establish (or otherwise discern) new, constraining limits for possible sub-dominant contributions arising with sterile neutrinos. These limits (discovery) will arise from observation of absence (existence) of deviations from expectations of conventional three-state neutrino flavor mixing.

The global fits of UNO can be used to search for amplification of sub-dominant ν_μ to ν_e oscillation resulting from matter resonances in the Earth. Two kinds of resonance effects have been discussed in the literature. One possibility would be an MSW-type enhancement which could take place in the terrestrial mantle or in the core. A second type of resonance enhancement has been proposed for neutrinos which traverse the mantle, the core, and again the mantle. The sequence of altering matter densities may give rise to a constructive interference among oscillation amplitudes such that ν_μ to ν_e is enhanced for certain neutrino energies. Evidence for these effects could conceivably arise as deviations of UNO data from global fits which include three-state mixing but which do not allow for these resonance effects.

	Neutrino source			
Detector site	BNL	CERN	Fermi Lab	JAERI
Frejus	5980	130	6830	8900
Gran Sasso	6530	730	7340	8830
Homestake	2530	7350	1280	8240
Kamioka	9630	8750	9130	290
San Jacinto	3860	8610	2620	8150
Soudan	1710	6580	730	8490
WIPP	2930	8160	1770	8880

Table 4.2: Baselines in km for potential experimental sites.

4.3 Long-Baseline Neutrino Oscillation Experiments

4.3.1 Overview

UNO is well-suited to become a distant target for future long-baseline neutrino oscillation experiments. The neutrino source could be either a high-intensity conventional ("Super") beam produced by π decays, or a muon storage ring ("neutrino factory"). Superbeam studies would require no modification to the baseline design, and could be conducted together with the search for nucleon decay and other physics. To fully exploit the beam from a neutrino factory, however, would require a magnetic field to identify muon charge, as discussed further below, and in Section 6.4. Table 4.2 summarizes baselines between potential neutrino sources and proposed future far detector sites.

K2K and other long-baseline experiments planned for the coming five years will focus primarily on $\nu_\mu \to \nu_\tau$ oscillation. ν_e appearance studies with MINOS may achieve $\sim 10^{-2}$ sensitivity to $\sin^2 2\theta_{13}$. Positive observation of $\nu_\mu \leftrightarrow \nu_e$ oscillation at smaller mixing angles, as well as searches for CP violation, will require more intense beams with greater purity—and very massive detectors like UNO to study them.

4.3.2 Superbeams

Within 5–10 years, planned or proposed high-intensity proton sources such as the 3 GeV proton synchrotron at the Japan Hadron Facility (JHF) [17] or the CERN Superconduction Proton Linac (SPL) [50] will provide beams of unprecedented power which can be harnessed for long-baseline neutrino physics. With increased power, corresponding gains in pion, and hence neutrino, production are possible. As Table 4.3 shows, orders of magnitude greater luminosity than the present K2K and even MINOS experiments are on the horizon.

The physics potential and feasibility of these superbeams has recently been the focus of

Source	Location	Proton Energy (GeV)	Power(MW)	Experiment
KEK PS	KEK	12	0.005	K2K
NUMI	Fermilab	120	0.2	MINOS
SPS	CERN	400	0.2	CNGS
JHF PS	JAERI	3	1	JHF/SK
SPL	CERN	2.2	4	UNO?

Table 4.3: Proton source parameters for present and future long-baseline neutrino oscillation experiments. Future high-intensity proton sources are the key to producing “superbeams”.

considerable study [38, 43, 40, 41, 44]. It is fair to say that while superbeams fall short of a neutrino factory in their physics reach, they still hold the promise of significant gains in sensitivity to θ_{13} and (under reasonable assumptions) δ_{CP} over existing (CHOOZ, K2K) and approved (MINOS, CNGS) experiments. Moreover, they do so at a fraction of the cost and absent most technical challenges of a muon storage ring.

A long-baseline experiment using a $\sim$1 GeV neutrino beam from the JHF facility to Super-Kamiokande has been proposed [17]. The Fermilab working group has also considered large water Cherenkov targets for a superbeam [41, 40]. To provide a concrete example of UNO’s sensitivity, a similar experiment, this time using a $\sim$300 MeV beam from the CERN SPL to UNO (assuming a baseline of 130 km to one of the potential sites at Fréjus—see Chapter 5) has been studied in detail [44].

4.3.2.1 The CERN SPL neutrino beam

The proposed CERN SPL would recycle the superconducting cavities of the LEP e^+e^- collider into a very intense proton linac [50]. The neutrino beam from pions produced in a liquid mercury jet target has been designed and simulated in detail [45]. The pion focusing and decay tunnel (20 m length, 1 m radius) parameters have been chosen to maximize the ν_μ flux while minimizing the contamination of ν_e from muon decay. The relatively low energy of the SPL (2.2 GeV proton kinetic energy) helps assure the purity of the beam, since kaon production is negligible. As explained below, the low energy of the beam also minimizes detector backgrounds to any ν_e appearance signal. The polarity of the neutrino beam can be selected by focusing either π^+ or π^-.

The neutrino fluxes for a π^+-focused beam at a distance of 130 km are shown in Figure 4.3. Those of the π^--focused beam are similar but slightly smaller, due to suppression of π^- production by a positively-charged primary beam. The fluxes are normalized to 10^{23} protons on target per year, corresponding to the design specification of 10^{16} protons on target per second and a realistic operating efficiency (1 “year” = 10^7 seconds). For comparison, the total design luminosity of the K2K experiment is 10^{20} protons on target, accumulated over five years. The mean energy of the neutrino beam is well-matched to the distance between

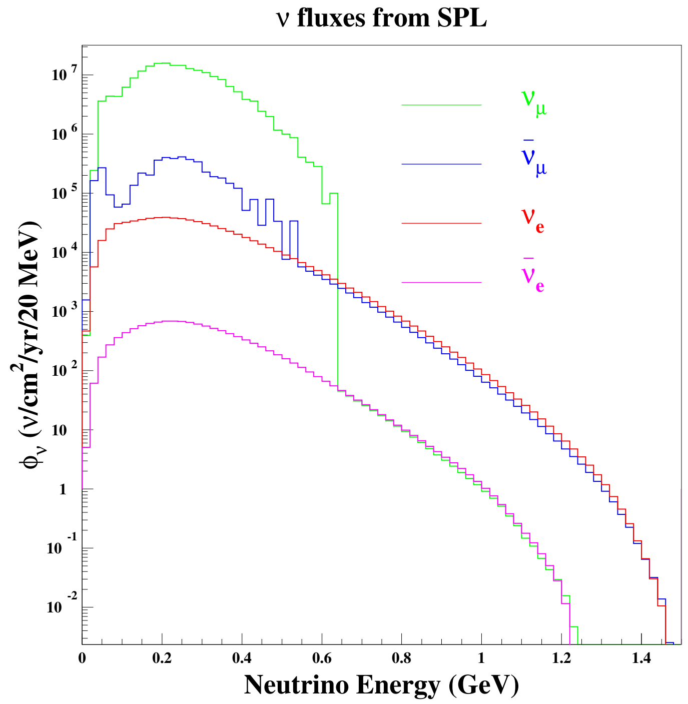

Figure 4.3: Simulated neutrino fluxes from the SPL, at a distance of 130 km.

CERN and Fréjus and the expected $\Delta m^2_{13} (\simeq \Delta m^2_{23} \simeq 3 \times 10^{-3}\,\mathrm{eV}^2)$.

4.3.2.2 Simulation of UNO

For the this study, a water detector of 440 kton fiducial mass and performance identical to Super-Kamiokande is assumed. The response of the detector to positive (π^+) and negative (π^-) polarity neutrino beams from the SPL was studied using a detailed low-energy neutrino physics generator and detector simulation and reconstruction algorithms developed for the Super-Kamiokande atmospheric neutrino analysis. These algorithms, and their agreement with real neutrino data, have been described and demonstrated elsewhere [49, 51, 52].

To estimate the efficiency for the ν_e appearance signal, data from the SPL beam was generated assuming 100% conversion of ν_μ into ν_e (and likewise ν_e into ν_μ). These events were then weighted by the oscillation probability for each $(\sin^2\theta_{13}, \Delta m^2)$ hypothesis. Since a large background rejection factor is necessary, four times as much data from the unoscillated (primarily $\pi \to \mu\nu$) beam was also generated and analyzed. These events were weighted by the *survival* probability for a given oscillation hypothesis. The initial sample consists of all events reconstructed in the fiducial volume with a visible (electron-equivalent) energy between 100 and 450 MeV, having only one identified Cherenkov ring [55].

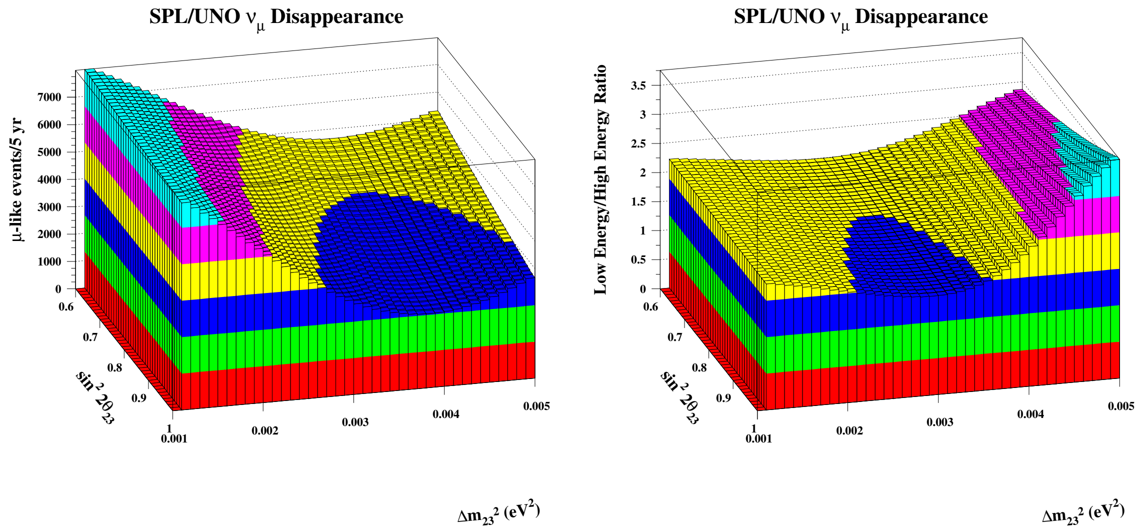

Figure 4.4: Five-year ν_μ disappearance signal. At left, the number of single-ring μ-like events as a function of $\sin^2 2\theta_{23}$ and Δm^2_{23}. Rate alone determines the oscillation parameters along contours of the same height(color). At right, the ratio of low-energy to high-energy μ-like events. The measured muon spectrum narrows the permitted range of parameters. Most of the region shown is presently allowed by Super-Kamiokande data.

4.3.2.3 ν_μ disappearance

The simulation predicts almost 10,000 charged-current ν_μ interactions from the SPL beam in five years of UNO running. Using standard particle identification algorithms from the Super-Kamiokande atmospheric neutrino analysis, a disappearance experiment can be performed to measure $\sin^2 2\theta_{23}$ and Δm^2_{23} with high precision. Figure 4.4a shows the expected sample of μ-like events. For a given rate, the oscillation parameters are constrained to lie along an arc of a particular shade. Some information is also contained in the observed muon spectrum. To exploit this, the ratio of low-energy ($p_\mu < 350\,\mathrm{MeV/c}$) to high-energy ($p_\mu > 350\,\mathrm{MeV/c}$) muons can be used in the fit (see Figure 4.4b).

Examples of the $\sin^2 2\theta_{23}$ and Δm^2_{23} measurement precision are shown in Figure 4.5. For $\Delta m^2_{23} >\sim 3 \times 10^{-3}\,\mathrm{eV}^2$, 1 σ(statistical) errors of a few percent are obtainable. For smaller mass differences, the muon spectrum loses its sensitity and the allowed region becomes a crescent-shaped contour of constant event rate.

4.3.2.4 ν_e appearance

In the absence of neutrino oscillation, the dominant reaction induced by the beam is ν_μ quasi-elastic scattering, leading to a single observed (prompt) muon ring. Recoiling protons are well below Cerenkov threshold at the energies discussed here, and hence produce no rings. To unambiguously identify a potentially small ν_e appearance signal, it is essential to avoid

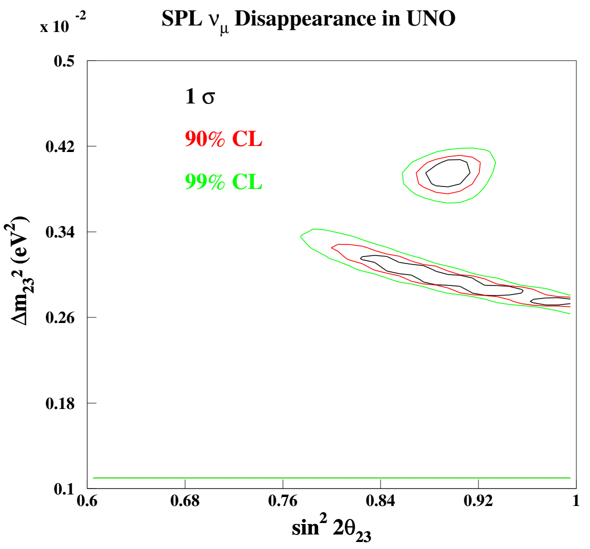

Figure 4.5: Sensitivity to θ_{23} and Δm^2_{23} from a five-year ν_μ disappearance experiment with the SPL beam in UNO. The contours show (from inside outward) the 1 σ, 90% and 99% confidence level measurement errors for two different points in parameter space.

confusion of muons with electrons. Thanks to the low energy of the SPL neutrino beam, the Cherenkov threshold itself helps separate muons and electrons, since a muon produced near the peak of the spectrum (~ 300 MeV/c) cannot be confused with an electron of comparable momentum; instead it will appear to be a much lower-energy (~ 100 MeV/c) electron.

Particle identification discriminates between the Cherenkov patterns produced by showering ("e-like") and non-showering ("μ-like") particles. For the energies of interest in this beam, the different Cherenkov opening angles of electrons and muons can also be exploited. The particle identification performance of water Cherenkov detectors like Super-Kamiokande has been validated using a test beam at the KEK laboratory [53]. In addition, muons which stop and decay (100% of μ^+ and 78% of μ^-) produce a detectable delayed electron signature which can be used as an additional means of background rejection.

An atmospheric neutrino experiment requires unbiased identification of muons and electrons, however in a ν_e appearance search, it is desirable to tighten the cut on particle identification, slightly reducing the efficiency for electron identification in return for higher purity of the resulting e-like sample. The standard Super-Kamiokande particle identification criteria are based on a maximum likelihood fit of both μ-like and e-like hypotheses. A ring is identified as μ-like or e-like depending on which hypothesis gives the greater likelihood; in terms of the particle identification estimator P (in arbitrary units), an event is e-like if $P_e > P_\mu$. For this study, the cut is tightened such that an event is considered e-like only if $P_e > P_\mu + 1$. As Figure 4.6 shows, this cut introduces only a small inefficiency for true ν_e charged-current interactions, while reducing the ν_μ background considerably. In addition, any event with an identified muon decay signature is rejected from the e-like (ν_e appearance)

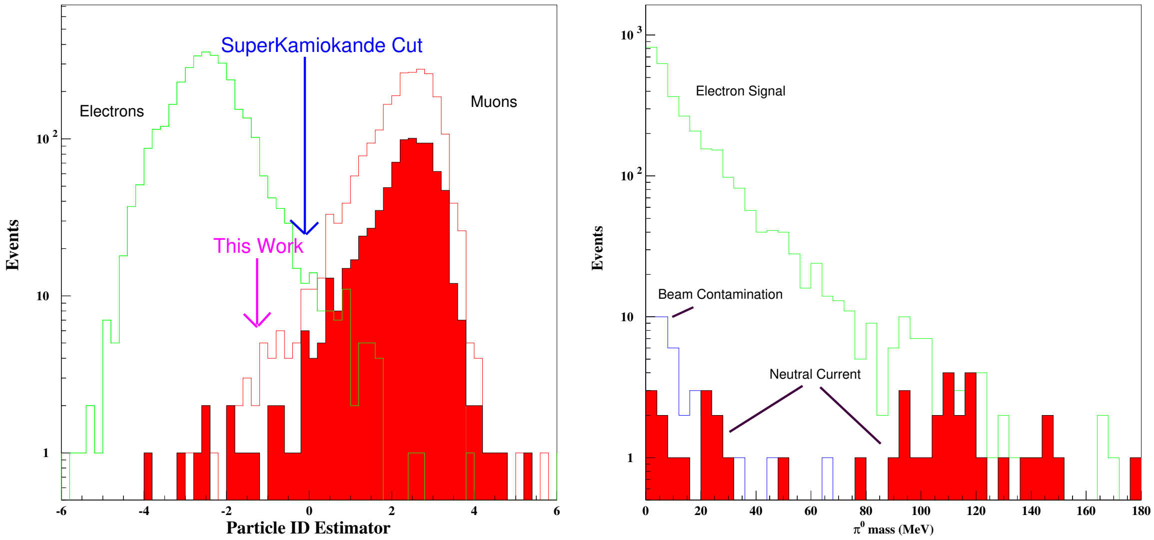

Figure 4.6: Background rejection for ν_μ charged-current events (left) and π^0 production (right). The normal particle ID cut used by Super-Kamiokande can be tightened with little loss of efficiency, and a $\mu \to e$ veto can also be applied. For π^0's, a specialized reconstruction algorithm identifies the best candidate for a second ring. Events are rejected if the original ring and the secondary candidate sum to an invariant mass greater than 45 MeV. Real electrons typically yield a small mass when fit as two-ring events.

sample.

Neutral-current production of π^0 through resonance-mediated and coherent processes is another source of background. This background is suppressed by the low energy of the beam and the relatively small boost available to the π^0, but still important. Most π^0's are correctly identified as two-ring events (and therefore rejected), but asymmetric decays can produce low-energy γ which are missed by the standard pattern-recognition algorithm. As for μ/e identification, the requirements of a ν_e appearance experiment (where π^0's are *a priori* more common than electrons) are quite different from those of an atmospheric neutrino experiment (where electrons are copiously produced and π^0 production is relatively rare). In an appearance experiment, we can afford to apply more lenient criteria to reject almost all π^0 at a small cost in electron efficiency. A specialized algorithm has been developed to search for low-energy γ's in events where the standard ring-finding algorithm finds only a single ring [54]. The algorithm always identifies a candidate for a second ring, which, if the primary ring is truly a single electron, is typically either very low energy, or coincident with the primary. If, on the other hand, two γ from π^0 decay are present, the second ring-candidate is usually the π^0 daughter which was missed by the standard pattern-recognition. As Figure 4.6b shows, by requiring that the invariant mass formed by the primary ring and the secondary ring-candidate is less than 45 MeV$/c^2$, almost all remaining π^0 contamination of the single-ring, e-like sample is removed.

The background in each category (ν_μ charged-current, ν_e contamination in the original

Channel	Initial sample	Fit in fiducial volume Single-ring $100 - 450\,\mathrm{MeV}/c^2$	Tight particle ID	No $\mu \to e$	$m_{\gamma\gamma} < 45\,\mathrm{MeV}/c^2$
ν_μ^{CC}	9760	6360	60.5	27.5	16.5
ν_e^{CC}	134	90.2	88.0	88.0	85.8
NC	406	95.7	84.7	84.7	18.7
$\nu_\mu \to \nu_e$		82.4%	77.2%	76.5%	70.7%

Table 4.4: Summary of simulated data samples a π^+ focused neutrino beam. The first three lines show the expected background surviving the selection at each stage for a 5-year exposure of UNO to the unoscillated beam at 130 km. The bottom line shows the efficiencies for the $\nu_\mu \to \nu_e$ signal. The numbers in the rightmost column (after all cuts) represent the sample used to estimate the oscillation sensitivity.

Channel	Initial sample	Fit in fiducial volume Single-ring $100 - 450\,\mathrm{MeV}/c^2$	Tight particle ID	No $\mu \to e$	$m_{\gamma\gamma} < 45\,\mathrm{MeV}/c^2$
$\bar{\nu}_\mu^{CC}$	2050	1350	25.3	7.7	7.7
$\bar{\nu}_e^{CC}$	36.3	33	29.7	29.7	29.7
NC	129	36.3	33	33	3.3
$\bar{\nu}_\mu \to \bar{\nu}_e$		79.3%	74.1%	74.0%	67.1%

Table 4.5: Summary of simulated data samples a π^- focused neutrino beam. The first three lines show the expected background surviving the selection at each stage for a 5-year exposure of UNO to the unoscillated beam at 130 km. The bottom line shows the efficiencies for the $\bar{\nu}_\mu \to \bar{\nu}_e$ signal. The numbers in the rightmost column (after all cuts) represent the sample used to estimate the oscillation sensitivity.

beam, and neutral current) remaining after all selections, and the efficiency for signal, after each cut is summarized in Table 4.4 for the π^+-focused beam and Table 4.5 for the π^--focused beam. Contamination by ν_e from muon decay in the secondary beam is dominant. The handful of surviving detector-related backgrounds are largely pathological: for the π^+ beam, half the remaining ν_μ^{CC} events arise from muon decay in flight, while the neutral-current background originates from events at the edge of the fiducial volume and hopelessly asymmetric π^0 decays.

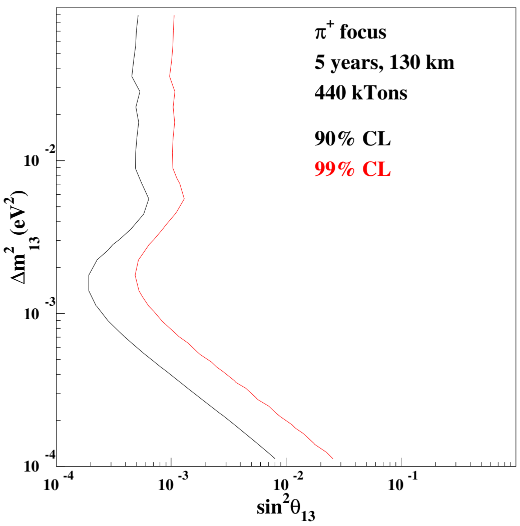

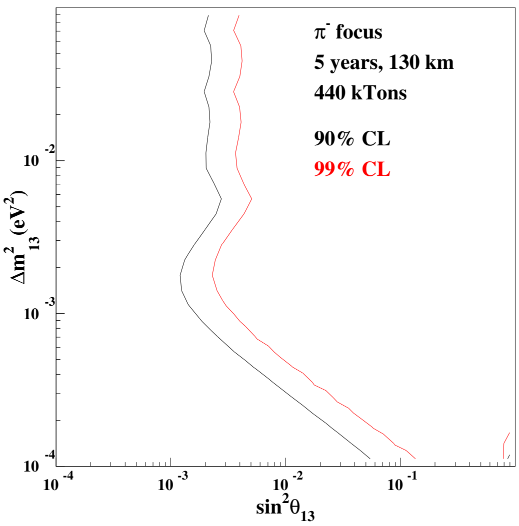

Figure 4.7: θ_{13} sensitivity for π^+- (left) and π^-- (right) focused neutrino beams. The outer(inner) contours are the regions where the expected confidence level to reject the oscillation hypothesis in the absence of oscillation exceeds 90%(99%).

4.3.2.5 θ_{13} sensitivity

Using the simulated event samples, the sensitivity of a hypothetical experiment to $\sin^2\theta_{13}$ can be estimated. For the present study, only statistical errors are considered. Given the 2.5:1 disparity between expected beam and detector backgrounds, it is likely that beam-related uncertainties will be the most important, and these can be controlled by measuring the beam with a near detector and using data from the HARP [56] experiment to refine the hadronic production model. For a given point in the $(\sin^2\theta_{13}, \Delta m^2_{13})$ plane, the expected confidence level of the oscillation hypothesis can be calculated from the simulated data assuming oscillations do not, in fact, occur. A full three-component neutrino oscillation probability is used, since the large mixing between ν_μ and ν_τ suggested by atmospheric neutrino data [58, 59, 60] (and the fact that $\Delta m^2_{23} \approx \Delta m^2_{13}$) implies that a substantial fraction of the original ν_μ beam will oscillate to ν_τ, effectively *decreasing* the ν_μ^{CC} background. For mixing between neutrinos of the first and second generations, $(\sin^2 2\theta_{12}, \Delta m^2_{12})$ are assumed to have values (0.8, $5\times10^{-5}\,\mathrm{eV}^2$), consistent with the Large Mixing Angle solution of the solar neutrino problem. Determination of θ_{13} is largely insensitive to this assumption. The confidence level estimation (based on simple event counting without any spectral information) follows the "Unified Approach" of Feldman and Cousins [61]. Figures 4.7a and 4.7b show the expected sensitivities of a 5-year UNO run, for π^+- and π^--focused beams, respectively.

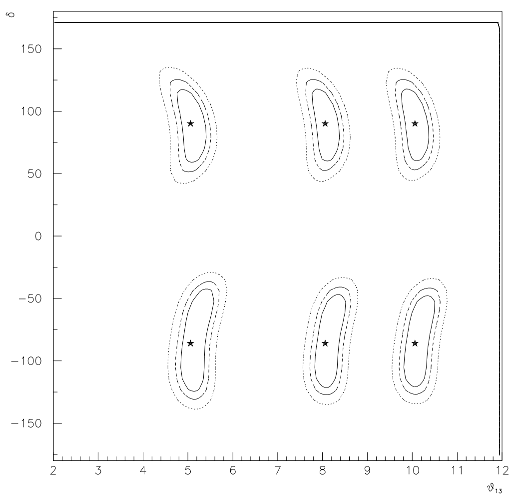

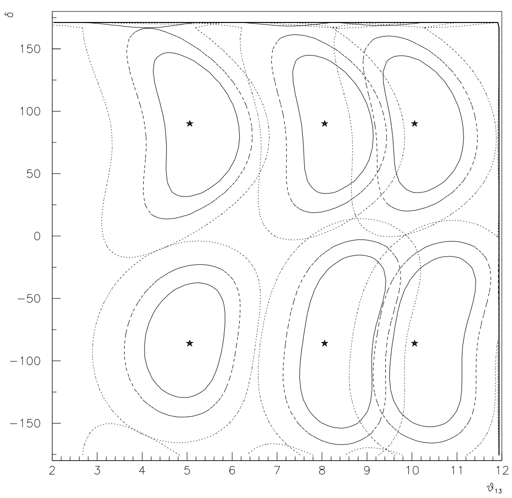

Figure 4.8: δ_{CP} sensitivity for UNO (left) and a hypothetical 40 kton detector (right) with the SPL neutrino beam. Samples were generated with three values of θ_{13} and $\delta_{CP} = \pm 90°$ and then fit. The contours show the allowed regions at 1 σ, 90% and 99% confidence levels. Clearly UNO's large size is crucial. Under the assumptions stated in the text, UNO can distinguish maximal CP violation from no CP violation at better than 99% confidence level.

4.3.2.6 δ_{CP} sensitivity

Unfortunately, the unmeasured cross-section for $\bar{\nu} + {}^{16}O$ charged-current scattering is calculated to be five to six times smaller than that of $\nu + {}^{16}O$ at these energies. Further, π^- production is suppressed by about 20% with respect to π^+ for a primary proton beam. These two factors conspire to make measurement of CP violation a challenge, unless θ_{13} is near the maximum value allowed by the CHOOZ [62] experiment.

To study δ_{CP} sensitivity quantitatively, a 2-year run with π^+ focusing and a 10-year run with π^- focusing are considered; the longer exposure to the $\bar{\nu}$ compensates for the smaller anti-neutrino cross-section. An optimistic, but not unreasonable, LMA solar solution ($\Delta m^2_{12} = 10^{-4}\,\mathrm{eV}^2$, $\theta_{12} = 45°$) is postulated. The approach outlined in [35, 57] is used to fit θ_{13} and δ_{CP} simultaneously, thereby accounting for possible correlation between them. Matter effects are included, however in contrast to longer-baseline, higher-energy scenarios (GeV superbeams or a neutrino factory), they are completely negligible.

Figure 4.8 shows the result of the study for three values of θ_{13} ($5°, 8°$ and $10°$) and $\delta_{CP} = \pm 90°$. UNO is capable of observing maximal CP violation at better than 99% confidence level, under the stated assumptions, even for the smallest of the three θ_{13} hypotheses.

4.3.3 Neutrino Factory

Study of muon storage rings as neutrino sources actually preceded consideration of super-beams, since muon storage rings have long been discussed in the context of a $\mu^+\mu^-$ collider. A number of technical challenges must be overcome before construction of a neutrino factory is feasible, many of them related to cooling the muons from $\pi \to \mu$ decay for further acceleration.

Nevertheless, neutrino factories have attracted tremendous interest[29, 30, 31, 33, 34, 35, 19, 20]. The concept of a neutrino factory is simple. A beam of muons (of either charge) is accelerated to an energy of 10 to 50 GeV, and then stored in a ring with long, straight segments pointing to a detector. As the muons decay, their daughter neutrinos are boosted toward the detector and arrive with a well-characterized spectrum and flavor composition. The neutrino energies are determined by the electroweak physics of the Michel spectrum, and a beam of μ^- always produces equal numbers of ν_μ and $\bar{\nu}_e$. By storing μ^+ in the ring, $\bar{\nu}_\mu$ and ν_e are produced instead. By contrast, a conventional neutrino beam from π decay is plagued by uncertain absolute normalization, spectrum and ν_e content, which must be estimated from knowledge of hadronic physics. Moreover, a neutrino factory beam would be extremely intense; 10^{20} useful muon decays in the straight section is considered achievable in a "year" of 10^7 seconds[19, 20].

Many oscillation channels are accessible with the neutrino factory; those for a stored μ^- beam are:

- $\nu_\mu \to \nu_\mu$, $\nu_\mu \to \mu^-$, (survival)
- $\nu_\mu \to \nu_e$, $\nu_e \to e^-$, (appearance)
- $\nu_\mu \to \nu_\tau$, $\nu_\tau \to \tau^-$, (appearance)
- $\bar{\nu}_e \to \bar{\nu}_e$, $\bar{\nu}_e \to e^+$, (survival)
- $\bar{\nu}_e \to \bar{\nu}_\mu$, $\bar{\nu}_\mu \to \mu^+$, (appearance)
- $\bar{\nu}_e \to \bar{\nu}_\tau$, $\bar{\nu}_\tau \to \tau^+$, (appearance)

and a corresponding list of charge-conjugate channels is available if μ^+ are used.

4.3.3.1 Physics program

The principal physics goals of a neutrino factory[1] are:

- Precision measurement of θ_{23} and Δm^2_{23} via $\nu_\mu \to \nu_\tau$ oscillation, using distortions of the ν_μ energy spectrum to directly observe the oscillatory behavior,

[1] The present work addresses only the first two items, and is intended mainly as a plausibility argument pending more refined studies.

Table 4.6: Charged-current event rates per year ($\equiv 10^{20}$ muon decays) for a 30 GeV neutrino factory at a distance of 7300 km.

	ν_μ	$\bar{\nu}_e$	$\bar{\nu}_\mu$	ν_e
CC events per year	110,000	44,000	52,000	94,000

- Search for $\bar{\nu}_e \rightarrow \bar{\nu}_\mu$ oscillation, using appearance of "wrong-sign" muons,
- Measurement of the sign of Δm^2_{23}, using the matter effects on the spectrum and rate of wrong-sign muons,
- Search for CP violation via differences in the rate of $\bar{\nu}_e \rightarrow \bar{\nu}_\mu$ compared to $\nu_e \rightarrow \nu_\mu$, and
- Precision measurement of θ_{13}, using a global fit to appearance and disappearance data.

ν_e or $\bar{\nu}_e$ propagating through the earth experience a different refractive index due to matter effects[9]. Matter effects can alter oscillation probabilities, sometimes dramatically. They also mimic CP violation since $P(\nu_e \rightarrow \nu_x)$ and $P(\bar{\nu}_e \rightarrow \bar{\nu}_x)$ are affected oppositely: one (depending on the sign of Δm^2) is enhanced while the other is suppressed. Studies have shown that the physics goals of a neutrino factory are most readily achieved by combining information from detectors at two baselines, for instance one intermediate ($\sim 3000\,\text{km}$) and one very far ($\sim 7000\,\text{km}$)[35]. UNO's size makes it better suited to act as the more distant target for the beam. As Table 4.2 shows, any UNO site on a different continent than the neutrino factory would suffice.

At present, neither the muon energy nor the distance from the neutrino factory to UNO are known; for definiteness, a 30 GeV storage ring producing 10^{20} useful muon decays per year (10^7 s) and a baseline of 7300 km are assumed.

4.3.3.2 Event rates

The rate of neutrino factory interactions in a distant detector scales as approximately:

$$\frac{dN}{dt} \sim \frac{E_\mu^3}{L^2} \tag{4.16}$$

where E_μ is the stored muon energy and L is the distance from the neutrino factory[31]. The constant of proportionality depends on the neutrino species to be detected, but the resulting event rates are enormous. As Table 4.6 shows, even at a distance of 7300 km UNO would collect approximately one contained event every 70 seconds while the beam is on. The rock surrounding the detector is also a target, and the analog of Equation 4.16 for entering events includes another power of E_μ. If $E_\mu = 50\,\mathrm{GeV}$, the number of neutrino-induced muons entering the detector is about 4 times greater than the number produced inside.

That a larger detector will collect more events than a smaller one is clear; the real question for UNO is whether the statistical power of these enormous event samples can overcome the limited spatial resolution and multi-track separation of the water Cherenkov technique.

4.3.3.3 Charge identification

Since the beam contains both neutrinos and antineutrinos, in the presence of oscillation a neutrino's identity can only be determined by measuring the charge of the resulting lepton. Of course, disappearance experiments (which do not require a charge measurement) are possible, but the merits of a neutrino factory detector will be judged primarily by its ability to observe the appearance of "wrong" sign muons: those arising from oscillation of electron (anti)neutrinos.

Charge identification in UNO presents two difficulties: the huge size of the detector (which works to its advantage in many other respects) and the loss of PMT collection efficiency in a magnetic field. Both considerations preclude magnetizing the full volume of the detector; instead magnetic regions must be localized, with tracks measured both before and after bending. At least two designs are consistent with this constraint:

- A magnet could be placed outside UNO along an exterior wall downstream of the neutrino factory, to deflect muons which leave the detector. Some external tracking system, for instance an array of streamer tubes, would then be required to measure the muon charge.

- Large, flat magnets could be installed between the UNO subdetector modules, to deflect muons as they pass from one segment of the detector to another. UNO itself would then measure the muon charge by comparing reconstructed muon directions on either side of the magnet.

Since an external tracking system has not been considered in any detail, the remainder of this section will focus on the second option. Section 6.4 describes the conceptual design of a solenoidal magnet which could be placed between subdetectors in this way. The design study suggests that the fringe field of such a magnet could be reduced to a level tolerable by nearby PMTs. Future work will also explore the possibility of a toroidal magnet design to further limit the fringe field.

The present concept calls for a field of 0.1 T in a bending region of 5 m. For purposes of charge identification, only the product of the field and the length of the bending region is important. A 0.5 T m field region provides a transverse momentum "kick" of 150 MeV/c to a passing muon. For a 30 GeV muon, this kick results in an angular deflection of 5 mrad. Since an oppositely charged muon would be deflected by an equal amount in the other direction, charge identification entails discriminating a 10 mrad difference in direction. While this deflection is small, UNO has a long "lever arm" with which to measure it. Assuming the

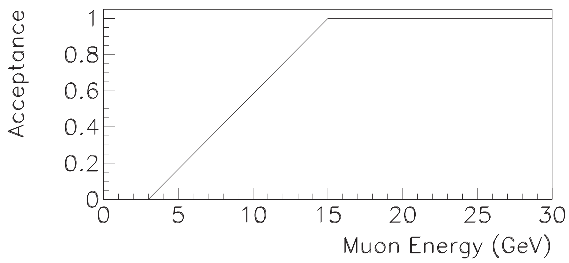

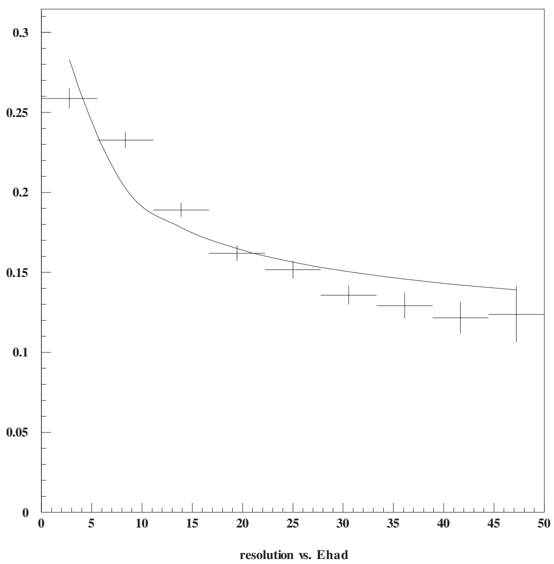

Figure 4.9: Assumed acceptance of UNO's conceptual magnet system as a function of muon energy (left) and estimated hadronic energy resolution vs. hadronic energy (right). The fit to the simulation is $\sigma_{E_{had}} = 9\% + 30\%/\sqrt{E_{had}}$

muon travels a further 30 m before leaving the detector, 10 mrad deflection corresponds to a 30 cm displacement. Timing information from the thousands of PMT's hit by the muon after bending can be used to compare the relative likelihoods of the positive and negative charge hypotheses, using a technique similar to that for μ/e identification. For comparison, a 10 mrad deflection corresponds to the RMS multiple scattering angle of a 30 GeV muon over approximately 300 radiation lengths ($\sim 100\,\text{m}$ of water).

The purpose of the present study is not to demonstrate the feasibility of charge identification, but rather to determine whether the question of its feasibility is worth pursuing. The remainder of this section will assume that charge identification is possible for muons which pass between subdetector modules and investigate the implications of that assumption.

4.3.3.4 Detector performance

Since charge identification would only be possible for muons which pass through a magnetic region between segments of UNO, the acceptance for lower-energy muons (which may stop before reaching a magnet) is reduced. To account for this, the acceptance shown in Figure 4.9a is assumed. This acceptance is roughly correct if the neutrino beam enters the detector horizontally along its 180 m axis, but in reality a neutrino beam from any great distance would arrive from a considerable angle below the horizon.

The detector's neutrino energy resolution is also important for ν_μ disappearance studies. An energetic muon's energy can be accurately determined from its range, but hadronic energy is more difficult due to the Cherenkov threshold. This effect is unavoidable in a water Cherenkov detector, and dominates the neutrino energy resolution. It has been studied using a "fast simulation" which counts the number of Cherenkov photons generated by each event, taking into account thresholds and interactions in the water, but skips the more time-consuming procedure of tracking the optical photons to the PMTs. The resulting resolution can be considered the "intrinsic" hadronic energy resolution of an ideal water Cherenkov detector which measures the number of photons emitted perfectly. The performance of a realistic detector like UNO should not deviate significantly from this limit, since detector-related effects contribute only a few percent. Figure 4.9b shows the hadronic energy resolution as a function of total hadronic energy for simulated neutrino interactions from a 50 GeV neutrino factory. The simulation predicts a hadronic energy resolution $\sigma_{E_{had}} = 9\% + 30\%/\sqrt{E_{had}}$.

Two simulated measurements have been studied, one a ν_μ disappearance measurement, and the other a $\bar{\nu}_\mu$ appearance experiment. As a point of reference for the possible capabilities of UNO, the response of a generic, finer-grained 50 kton iron-scintillator detector[19] is compared with UNO's in each case.

4.3.3.5 ν_μ disappearance experiment

The measured ν_μ spectrum exhibits large distortions due to the effects of oscillation. A disppearance experiment can measure Δm^2_{23} with high-precision by fitting this spectrum. Charge identification is not required for such a measurement. The sensitivity is quantified by generating a sample for a choosen "true" value of Δm^2_{23} (in this case, $3 \times 10^{-3}\,\mathrm{eV}^2$) and plotting the $\Delta\chi^2$ distribution for nearby values as shown in Figure 4.10. In this plot a steeper rise of $\Delta\chi^2$ over the same range indicates a more precise measurement of Δm^2_{23}. This study indicates that, as expected, UNO's resolution exceeds that of a 50 kton iron-scintillator detector by a factor of about three (the square root of the mass ratio). With the enormous number of events produced by a neutrino factory beam, a 1% of measurement of Δm^2_{23} appears easily in reach.

4.3.3.6 $\bar{\nu}_\mu$ appearance experiment

Similarly, a $\bar{\nu}_\mu$ appearance experiment has been simulated. The wrong-sign muon signal for UNO and a generic 50 kton iron-scintillator detector have been calculated based on an assumed $\sin^2 2\theta_{13} = 0.004$. Figure 4.11a shows the appearance rates for a perfectly efficient detector, and accounting for the assumed inefficiency for low-energy muons. Due to matter effects, the signal is strongly influenced by the sign of Δm^2, with $\bar{\nu}_\mu$ appearance enhanced if Δm^2 is positive and ν_μ appearance enhanced if it is negative. In Table 4.7, the signal rate in UNO is enhanced over that of the smaller iron detector by only a factor 4–5, rather than 9, due to reduced acceptance low-energy acceptance.

Nevertheless, the signal is considerable. Figure 4.11b shows the 90% confidence level sensitivity to $\sin^2 2\theta_{13}$ as a function of Δm^2_{23}, considering only the statistics of the appearance signal and neglecting background.

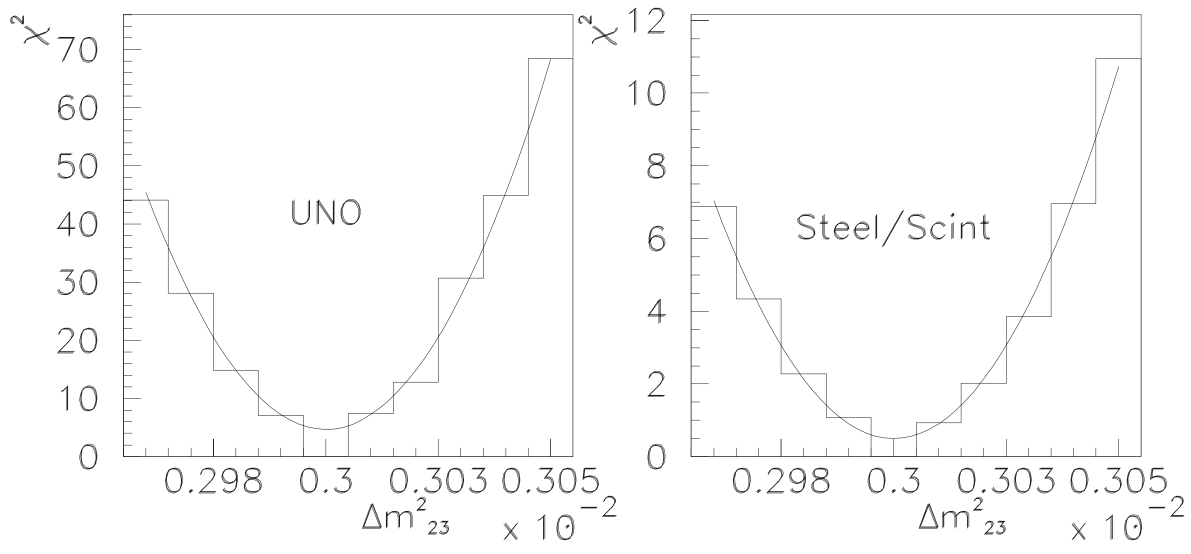

Figure 4.10: Comparison of Δm^2_{23} measurement precision for UNO and a 50 kton iron detector. The plot shows $\Delta\chi^2$ as Δm^2 deviates from its selected input value. UNO's greater size translates into a roughly a factor 3 improvement in resolution.

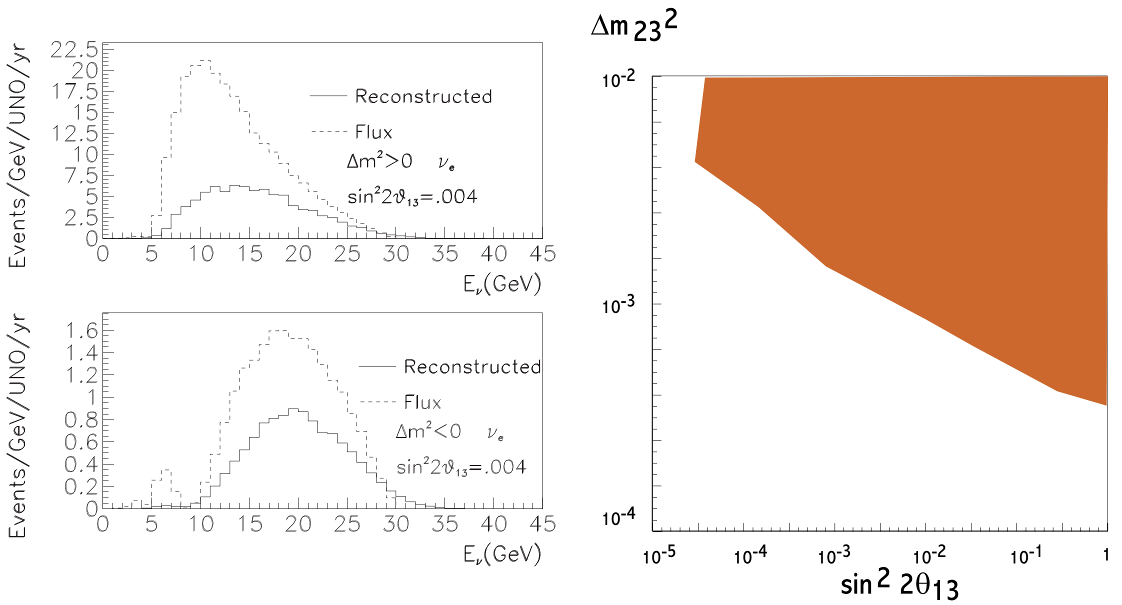

Figure 4.11: Left: UNO ν_μ appearance rates for $\sin^2 2\theta_{13} = 0.004$. "Flux" indicates the rate for a perfectly efficient detector while "Reconstructed" takes into account the acceptance of the magnetic system. Right: Estimated UNO 90% confidence level θ_{13} sensitivity vs. Δm^2_{23} for a 30 GeV muon storage ring at a distance of 7300 km, neglecting backgrounds.

	$\bar{\nu}_e(\Delta m^2 > 0)$	$\bar{\nu}_e(\Delta m^2 < 0)$	$\nu_e(\Delta m^2 > 0)$	$\nu_e(\Delta m^2 < 0)$
UNO	87	11	7	57
50 kt Fe	21	2	1	11

Table 4.7: Comparison of wrong-sign muon appearance rates (per 10^{20} muon decays) for UNO and a 50 kton iron scintillator detector, assuming $\sin^2 2\theta_{13} = 0.004$. Due to loss of acceptance at low E_μ, UNO's event rate scales less than the factor 9 expected from mass alone.

4.3.3.7 Backgrounds

The present θ_{13} sensitivity estimate does not include the effects of background. Pending a more exhaustive analysis to remedy this omission, background rates for UNO and an iron scintillator detector can be compared to gain some insight into their relative advantages.

Physics background to the $\bar{\nu}_\mu$ appearance search arises from several sources:

- Charged-current scattering in which the primary lepton lost, and a wrong-sign secondary muon from $\pi^\pm$ or $K^\pm$ decay is misidentified. This background depends on the detector's ability to distinguish primary leptons from secondaries in the shower.
- Neutral-current scattering in which *no* primary muon is present, but a wrong-sign secondary muon from $\pi^\pm$ or $K^\pm$ decay is misidentified. This background also depends on the detector's secondary vertex resolution.
- Charm production, followed by decay into an energetic muon. This background is irreducible, since no practical large-mass detector can resolve charm decay vertices from the primary interaction point.

Sensitivity studies with fine-grained detectors have shown that a cut $E_\mu > 4\,\mathrm{GeV}$ is effective at eliminating wrong-sign muon background. In UNO's case, the acceptance of the magnet system acts as a somewhat higher cut on E_μ. As Table 4.8 shows, UNO's expected background is only about twice that of a 50 kton iron detector, rather than the factor of 9 expected from mass. Recall that UNO's appearance *signal* similarly increased by a factor of about 5 rather than 9. Hence the signal to noise in UNO is actually somewhat better than for a fine-grained detector. In effect, UNO makes a tigher "cut" on the background (by virtue of its acceptance), which smaller detectors cannot afford since they begin with less signal.

While these preliminary studies are far from rigorous or conclusive, they suggest that UNO could compete with other technologies as a distant neutrino factory target — while advancing the search for nucleon decay and other physics goals simultaneously — if the considerable challenges of achieving muon charge identification can be met.

	$\nu_e \to \nu_\mu$				$\bar{\nu}_e \to \bar{\nu}_\mu$			
	Mis-ID	Charm	Signal $\Delta m^2 > 0$	Signal $\Delta m^2 < 0$	Mis-ID	Charm	Signal $\Delta m^2 > 0$	Signal $\Delta m^2 < 0$
UNO	9.3	5.7	21.8	2.8	7.6	4.0	1.8	14.3
50 kt Fe	4.0	5.7	5.3	0.5	6.3	4.0	0.25	2.8

Table 4.8: Comparison of wrong-sign muon background (per 10^{20} muon decays) for UNO and a 50 kton iron scintillator detector. Signal rates assume $\sin^2 2\theta = 0.001$. UNO's background scales by less than the factor 9 expected from mass alone. UNO's acceptance cuts events at low muon energy where the background is worst.

4.4 Supernova Neutrinos

On February 23, 1987, the first radiation from the explosion of a blue supergiant in the Large Magellanic Cloud with the unwieldy name of Sanduleak -69° 202 reached Earth and became known as supernova 1987A. An estimated 3 ± 1 supernova occur in our galaxy and its satellites every century [63] but the vast majority of stars are obscured by dust, making SN1987A the first supernova observed near our galaxy in almost 400 years. The last visible supernova was noted by Kepler in the year 1604. Estimates suggest that less than 10% of the galaxy is visible to the naked eye, making it quite likely that the next galactic supernova will be obscured as well; but the dust which obscures starlight is transparent to neutrinos.

Three hours before the light from SN1987A was observed, a handful of inverse beta decays:

$$\overline{\nu}_e + p \to e^+ + n, \tag{4.17}$$

were detected by two water Cherenkov detectors: Kamiokande II in Japan [64] and IMB in the US [65] as well as by the Baksan detector [66]. These events provided the first direct information from the interior of a supernova explosion, giving information about the temperature as well as the time evolution of the star immediately following the collapse of the core into a neutron star. The handful of events summarized in figure 4.12 have been the topic of hundreds of publications during the decade and a half since SN1987A was observed.

Although the resulting events do not provide detailed information concerning the burst, these observations nevertheless energized the field of neutrino astrophysics. Both theorists and experimentalists alike hope to see the neutrino signal from the next galactic supernova. With UNO in operation when the supernova's neutrino wave sweeps across the earth, we can gather information about nucleosynthesis, degenerate states of matter, shock wave stall and reheating, neutrino flavor mixing, neutrino mass, stellar atmospherics, and general relativity. The physics potential of UNO in the case of a galactic supernova is enormous.

The physics and astrophysics data which the next explosion could deliver is rich indeed. For just a few precious seconds, irreplaceable data will be available to those ready to receive it. Every second which passes brings the next supernova neutrino wave, already on its way

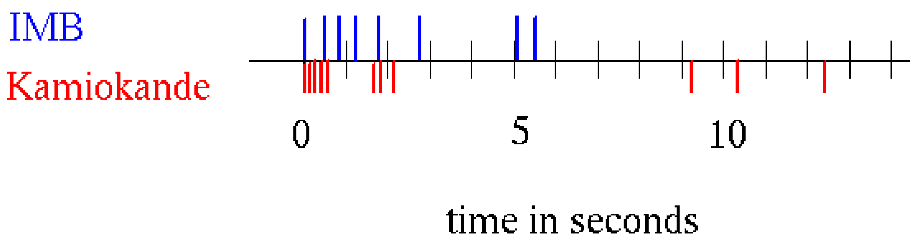

Figure 4.12: Time structure of 1987A neutrino events observed by water Cherenkov detectors in the U.S. and Japan.

Table 4.9: The number of events in all channels expected in UNO, compared to other detectors, either proposed (*), under construction (**), or running (***), for a supernova at 10 kpc.

Detector	Method	Mass	Events
UNO (*)	water Cherenkov	400 kt	140,000
Super-Kamiokande (***)	water Cherenkov	22.5 kt	9,000
OMNIS (*)	neutron capture	several kt	~2,000
SNO (***)	water Cherenkov	1 kt	1,000
KamLAND (**)	scintillation	1 kt	~500
Borexino (**)	scintillation	1 kt	~500
LVD (***)	scintillation	0.5 kt	~200

for thousands of years, closer to Earth. Its arrival will be a spectacular occurrence and UNO is an ideal detector to measure the resulting burst of neutrino interactions.

4.4.1 Supernova Neutrino Signals

The large mass of the UNO detector compared to other proposed and existing facilities means that the sample collected by UNO will outnumber that of all other detectors combined. This will likely be true until another large scale nucleon decay and neutrino detector that is sensitive to supernova neutrinos is constructed. For instance, table 4.9 summarizes the expected number of events observed for a supernova at 10 kpc.

For an explosion at the center of our galaxy, we expect ~300 events per kiloton of water. UNO would be sensitive to three main neutrino signals:

1. Weakly forward inverse beta decay events: ~89%

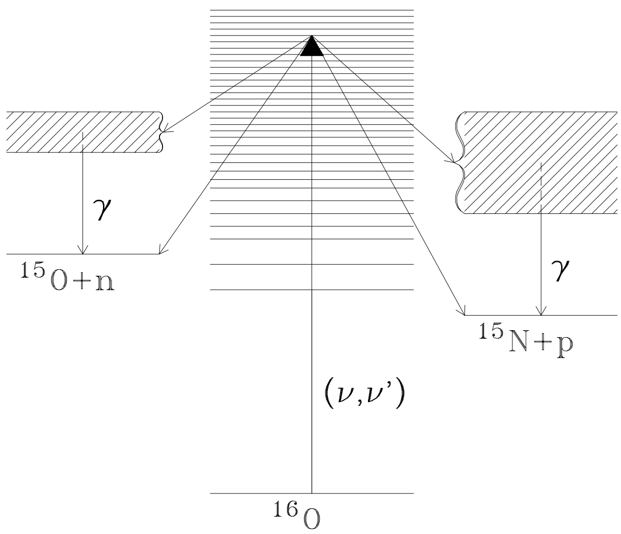

Figure 4.13: Nuclear energy level schematic for the neutral current process involving ^{16}O suggested by Langanke, Vogel, and Kolb [68].

2. Neutral current events involving ^{16}O: ∼8%, and
3. Directional elastic scattering events from $\nu_x + e^-$ and $\overline{\nu}_x + e^-$: ∼3%.

Each one of these modes will yield unique information. To illustrate, we will assume a type II supernova explosion 10 kpc (32,600 light-years) distant from Earth. This is a little past the galactic center and includes about half of the stars in the galaxy [67].

4.4.1.1 Inverse beta decay

From a type II supernova at 10 kpc, the baseline UNO design would see ∼130,000 inverse beta decay events in its entire volume, and ∼50,000 in the central (high-density PMT) region alone. This event rate dwarfs the response of any other detector, either planned or currently running. UNO will provide a fine-grained energy spectrum and time evolution of the burst, allowing a view of the dynamics and processes at work during the gravitational core collapse and resulting explosion.

4.4.1.2 Neutral current from ^{16}O

In 1996, Langanke, Vogel, and Kolbe [68] pointed out the existence of the following neutral current reaction:

$$\nu_x +^{16} O \to \nu_x + \gamma + X \tag{4.18}$$

where ν_x can be any of $\nu_\mu, \overline{\nu}_\mu, \nu_\tau$, or $\overline{\nu}_\tau$.

Higher energy supernova neutrinos can boost ^{16}O nuclei into the nuclear continuum, ejecting a nucleon and leaving either ^{15}O or ^{15}N in an excited nuclear state. These decay in

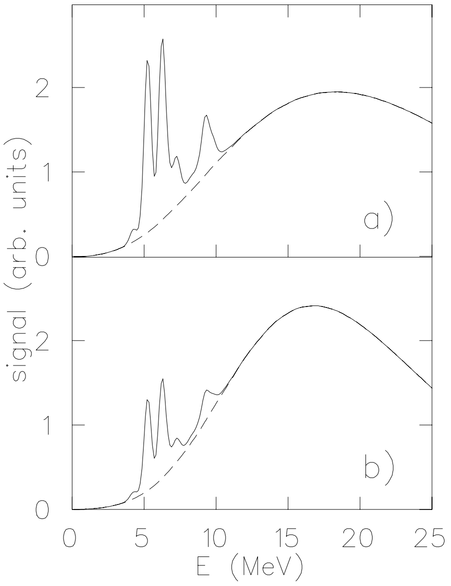

Figure 4.14: Energy spectrum showing the peaks produced by the neutral current process involving ^{16}O. The two plots assume differing average neutrino temperatures (top plot: T = 8 MeV, bottom: T = 6.3 MeV), indicating the sensitivity of this measurement.

turn, emitting gamma rays in the process. Figure 4.13 shows the energy levels which will generate these gamma rays. For a supernova at 10 kpc, this reaction alone will yield some 4,500 events in UNO's central region, a number comparable to all the other events in every other neutrino detector in the world.

These neutral current reactions produce mono-energetic photons in the energy range $5 \rightarrow 10$ MeV; the resulting events are easily identified, as shown in Figure 4.14. Since boosting ^{16}O into the nuclear continuum requires significant energy, these reactions are extremely sensitive to the temperature of the neutrino spectrum. Consequently, observation of these sharp energy lines in UNO's otherwise smooth energy spectrum should tell us a great deal about the stellar conditions which produced the heavy neutrino flavors as well as provide a handle on any flavor oscillations occurring in flight.

4.4.1.3 Elastic scattering

Neutrino elastic scattering should provide another $\sim$4,500 events in the UNO detector. These interactions preserve the direction of the incoming neutrinos and will allow us to determine the supernova's location in the sky. Using these events we could determine the position of the burst to within about $\pm 1^\circ$ which will allow astronomers to bring a variety of highly sensitive ground- and space-based instruments to bear on new supernova, facilitating collection of additional unique data about both the progenitor star and the intervening interstellar medium.

4.4.2 High Statistics Measurements

The large size of UNO makes important astrophysical measurements feasible. These measurements depend on identifying small numbers of events on top of a much larger background of supernova related signals, or simply being able to distinguish small numbers of supernova events from an uncorrelated background.

For example, about 10% of the total neutrino energy is carried away by the neutronization neutrinos from $e + p \to \nu_{\rm e} + n$. It is often assumed that these neutrinos all come within a 1 ms pulse, but they don't. These neutrinos are partially trapped, just like the thermal ones. The number of $\nu_{\rm e}$ that emerge in the 1 ms pulse is much lower, such that about 1% of the total neutrino energy is carried away in the identifiable pulse. Even in Super-Kamiokande, there might be only one event in the neutronization pulse. UNO, however, can collect a number of these neutrinos sufficient distinguish them from the later thermal signal and opening an important window on the physics of stellar collapse. Neutronization signals are also sensitive to neutrino mass (perhaps down to 1 eV) and oscillation (since if $\nu_{\rm e} \to \nu_\mu$, the number of neutrino-electron scattering events is reduced).

The size of UNO gives it an additional capability all its own: UNO is sensitive to supernovæ occurring throughout the local group of galaxies. Only UNO can detect more than a single (and hence, indistinguishable from background) event from a supernova in Andromeda. The total number of events would still be modest, comparable to the number observed during SN1987A, but having this additional reach would allow UNO to observe supernovæ three times more frequently than detectors limited to our own galactic neighborhood. Moreover, since we see Andromeda face-on, the chance of observing the optical counterpart for a neutrino burst there is about three times greater than in our own dust-obscured, obliquely-viewed Milky Way.

4.4.3 Black Hole Formation

Observationally, we know that massive stars end their lives as supernovae. Theoretically, we believe they can also form black holes; roughly half the stars whose cores collapse may end up as black holes [63]. While this would seem to preclude the detection of neutrinos, black holes form *after* neutrino generation is under way, the high-statistics samples available to UNO allow a search for direct evidence of black hole formation.

Under normal conditions (as was experimentally verified with SN1987A), the burst of neutrinos from a supernova should gradually trail off over the course of many seconds. However, if a black hole forms in the middle of a supernova explosion, the neutrino flux will be abruptly cut off as the event horizon rises up to swallow the neutrinosphere of the imploding star. Observation of such a cutoff in the supernova neutrino time structure will provide "direct" evidence for the birth of a black hole and would be incontrovertible evidence of their existence. The large size of the proposed UNO detector would give it a high neutrino sensitivity so that black hole formation, even relatively late formation in the neutrino burst could produce this signature. Smaller detectors might miss the formation signal due to a lack of event data during the critical period of the burst.

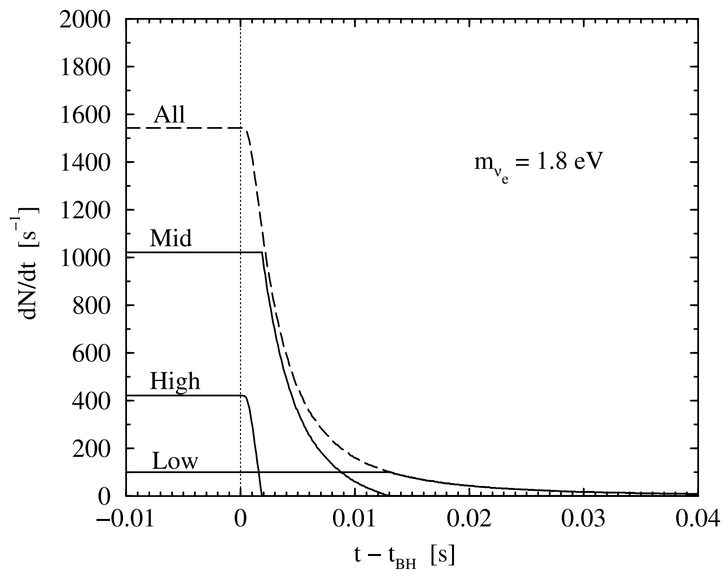

Figure 4.15: Neutrino data is broken up by energy range to provide a sharp "time zero" for the black hole formation (high energy) and well-defined delayed arrival times (middle energy). This delay is directly related to the mass of the ν_e. This figure is generated assuming the Super-Kamiokande detector.

Searching for the formation of a black hole at very late times is quite important since there are black hole formation scenarios where gravitational collapse may occur after a few or even several tens of seconds. UNO can observe the black hole cutoff after the rate has fallen to as little as 5% of other detectors' sensitivity and this will help to distinguish among equations of state [70].

Recently, the use of black hole formation during a supernova was proposed to directly determine the mass of the electron neutrino at the eV scale [69]. Their technique exploits the expected sharp cutoff in supernova neutrino luminosity discussed above. It predicts that UNO could determine the mass of the ν_e down to 1.0 eV by measuring the relationship between energy and arrival time of ν_e's straggling in after cutoff (see Figure 4.15). Further, because of mixing between the neutrino flavors, direct mass limits on ν_μ and ν_τ are also possible.

While terrestrial experiments will likely set more stringent limits on the ν_{e} mass, this exercise shows how measurements can be made using the precise neutrino-based "time zero" provided by black hole formation. This technique, especially in combination with other astronomical observations, can produce many other interesting and unique results.

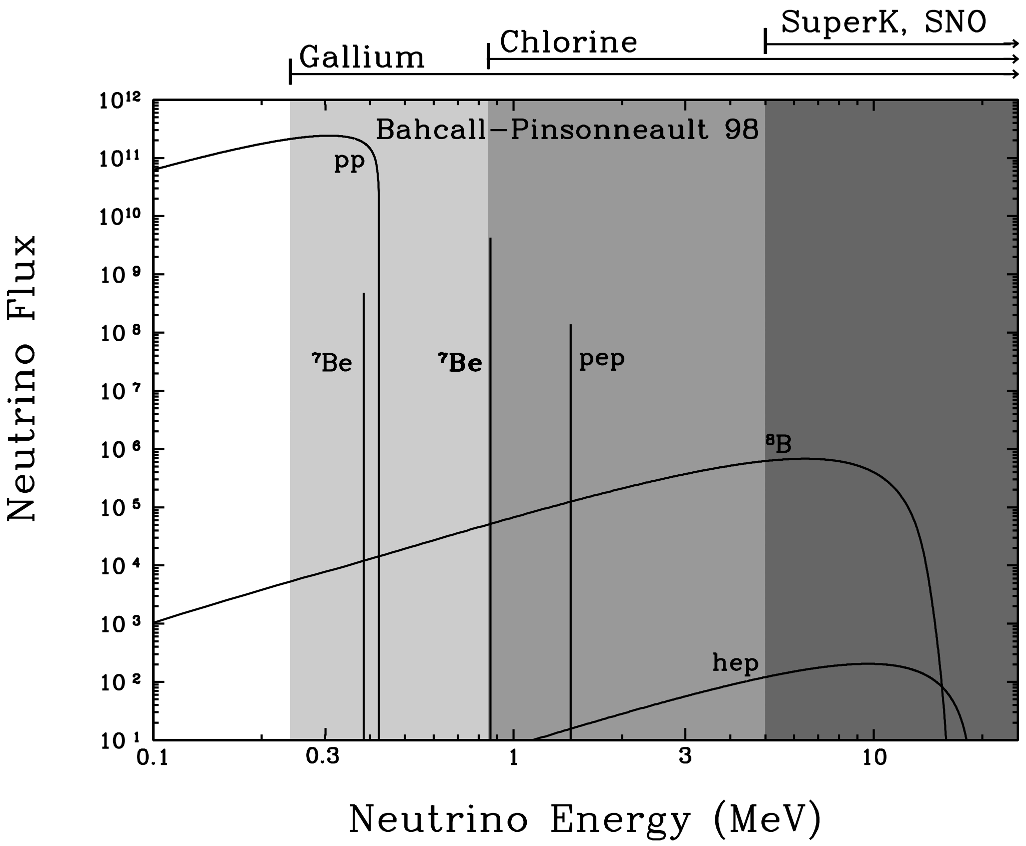

Figure 4.16: Solar Neutrino Spectrum using Standard Solar Model (BP98) Flux Predictions [73]. The dark shaded area shows the energy region covered by water Cherenkov detectors, the light shaded areas are covered by radio-chemical detectors.

4.5 Solar Neutrinos

Water Cherenkov detectors have measured the high energy tail (see Figure 4.16) of the solar ^{8}B neutrino flux using electron–neutrino elastic scattering [71, 72]. Since such detectors could record the time of an interaction and reconstruct the energy and direction of the recoiling electron, unique information of the spectrum and time variation of the solar neutrino flux was extracted (see Figure 4.17). This provided further insights into the "solar neutrino problem", the deficit of the neutrino flux (measured by several experiments) with respect to the flux expected by the standard solar models [73, 74]. It also constrained the neutrino flavor oscillation solutions in a fairly model-independent way.

The recoiling electrons from solar neutrino interactions are low in energy and produce few Cherenkov photons. However, if at least 20% of the UNO detection surface is photo-sensitive then solar neutrinos above 10 MeV could be detected even with a modest photo-sensor efficiency[2]. Due to its larger size, UNO has the potential to measure spectrum and time-variation of the high-energy solar neutrino flux more precisely, if systematic uncertainties can be kept small. For example, Super-Kamiokande's measurements (see Figure 4.17) obtained from 1258 days of data could be repeated in about half a year (the seasonal flux variation measurement requires of course a full year). In particular, a first measurement of the flux of the rare *hep* neutrinos may be possible.

4.5.1 Detector Requirements

UNO obviously needs a large fraction of its boundary area to be photo-sensitive to measure low energy recoil electrons from solar neutrino interactions. UNO also needs a low radioactivity environment, especially if it is equipped for a low energy threshold. Since a high rate of low energy radioactivity may accidentally combine with the dark noise present in photomultiplier tubes (PMTs), the dark noise rate should be as low as possible. The dark noise rate is proportional to the combined area of the photo cathodes and also depends on the temperature. In Super-Kamiokande, a single 20" PMT (operated at 15 ^{0}C) has a dark noise rate of about 3 kHz. At 30 ^{0}C about 9 kHz is expected. It may therefore be necessary to cool the water of UNO to suppress dark noise. For the following discussion we will assume that UNO is operated with 20" PMTs covering a fraction of 40% (as in Super-Kamiokande) of the total area. In this case, an energy threshold of 5 MeV can in principle be achieved. We will also assume a single dark noise rate of 3 kHz.

Since spallation events due to cosmic ray muons are an important background, a large shielding depth is also necessary. Super-Kamiokande, at a depth of about 2,700m water equivalent, controls this background by removing low energy interactions correlated (in space and time) with earlier cosmic ray muon events. Accidental correlations cause the loss of about 20% of the solar neutrino interactions at this depth. This loss should approximately scale with the muon intensity (shown in Figure 4.18 as a function of depth).

[2] This assumes a photo-sensor efficiency similar to Super-Kamiokande [72]

(a) (b) (c)

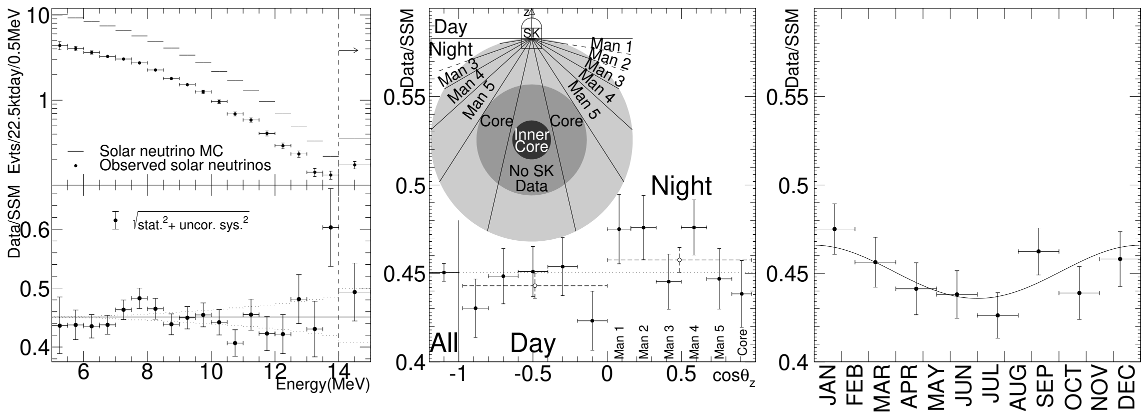

Figure 4.17: Energy Dependence (a), Solar Zenith-Angle (θ_z) Dependence (b), and Seasonal Dependence of the Solar Neutrino Flux (c) above 5 MeV from Super-Kamiokande [72] (1258 days of data). (a) The top panel shows the observed spectrum and the BP2000 [74] expectation between 5 and 14 MeV in 0.5 MeV bins. The data between 14 and 20 MeV are combined into a single bin. The bottom panel is the ratio of the observed spectrum and the BP2000 prediction. The horizontal line indicates the total flux and the band surrounding it the energy scale–related uncertainty. (b) Some models of neutrino flavor oscillation predict matter effects which enhance or reduce the apparent solar neutrino flux when passed through the earth. The left (right) dashed data point is the average day (night) flux. The solar neutrinos in the last night bin pass through the core of the earth. (c) The curve shows the flux variation caused by the eccentricity of the earth's orbit.

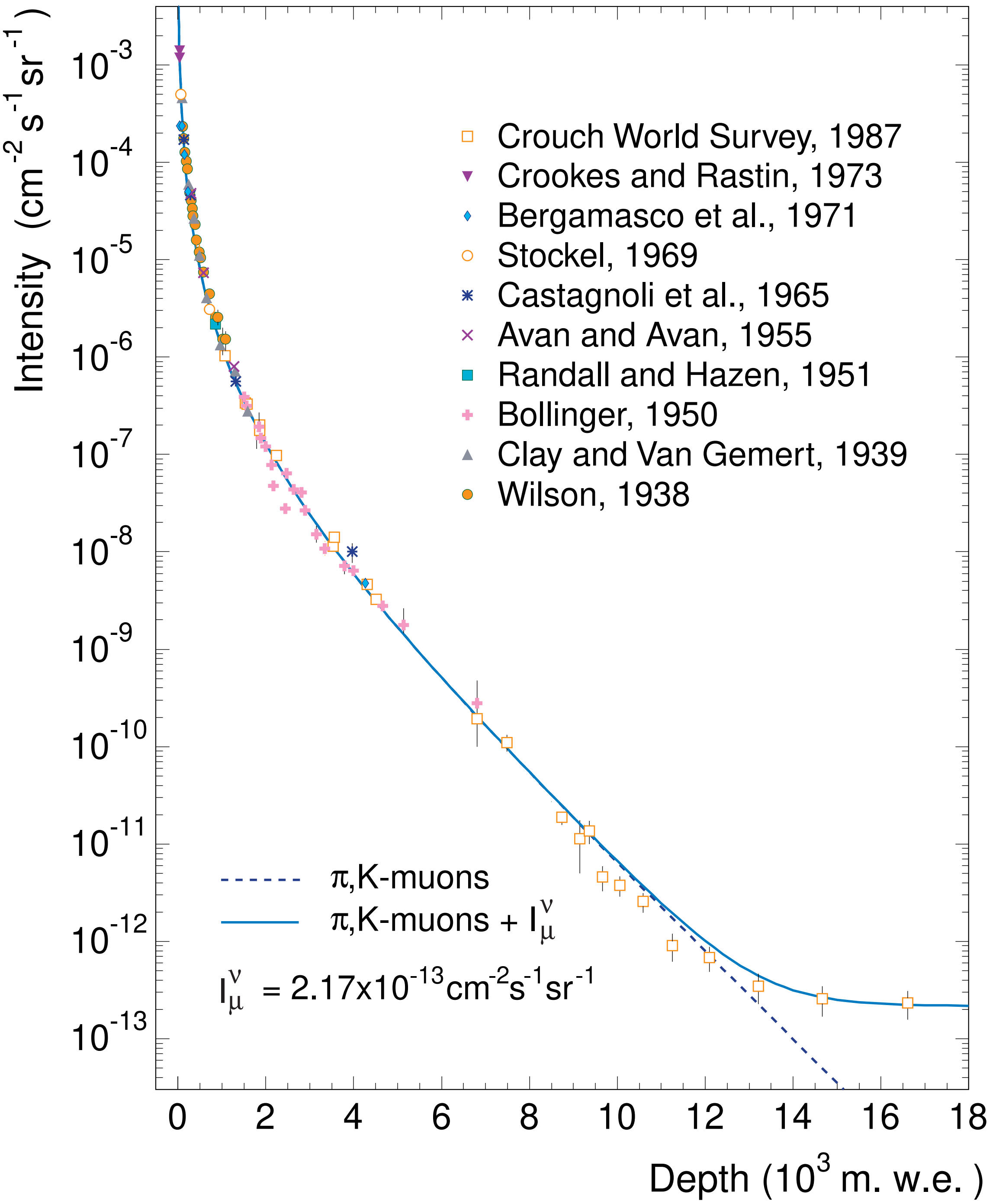

Figure 4.18: Muon Intensity vs. Depth in m water equivalent (m.w.e.) from [75].

4.5.2 Calibration

In addition to these requirements of the detector hardware, the detector calibration is very important. Super-Kamiokande (see Figure 4.17) has studied the recoil electron spectrum and the time-dependence of the solar neutrino flux. Of particular interest are the solar zenith angle dependence (day/night variation) and the sun–earth distance dependence (seasonal variation) of the flux. The systematic uncertainty of these measurements is dominated by the absolute energy scale and its directional and temporal dependence. Since Super-Kamiokande reports a systematic uncertainty of 0.64% [76] for the energy scale, the measurements are still statistically limited.

The goal for UNO is to significantly improve the total uncertainty. Due to its larger fiducial volume it will accumulate data much faster. To take advantage of this gain in statistical accuracy, the systematic uncertainties must be small. Super-Kamiokande calibrated its energy scale using an *in situ* linear accelerator [76]. The calibration was cross-checked with a portable neutron generator [77] which generates ^{16}N from ^{16}O in water. The accelerator has the advantage of producing triggered, mono-energetic electrons going from a well-defined position in a well-defined direction. The energy of the electrons can be tuned in the solar neutrino range. Its disadvantage is that the calibration requires a large amount of detector down-time and is therefore limited to only a few test points and directions. UNO would need to adopt the same strategy as Super-Kamiokande, namely to calibrate the energy scale with a linear accelerator and test directional and temporal dependence of this energy scale with a neutron generator or a similarly fast calibration device. This is especially necessary, since UNO is much larger than Super-Kamiokande and its fiducial volume has potentially a smaller degree of symmetry (e.g. a cube instead of a cylinder).

4.5.3 Low-Energy Electron Sensitivity

The Monte Carlo Simulation for low energy electrons in UNO assumes the following design for the inner part of an UNO detector: A cubic tank of side length 60 m with an optically sealed the central module of 58.8m length and 55m×55m area. The optical divider supports 38,064 20" PMTs (Super-Kamiokande style in size, dark noise, timing and charge response) spaced 70.7cm apart. This corresponds to 40% active area. A trigger is defined as coincidence of 77 PMT hits (a PMT hit is above a similar charge threshold as in Super-Kamiokande) within 400 ns. The 77 hit threshold is designed to be about 3 standard deviations higher than the average dark noise count. The resulting trigger efficiency as a function of input energy is shown in Figure 4.19a. With a light attenuation length of 83m (a typical value for Super-Kamiokande), the 50% point is reached at 5 MeV, if the electron is produced at the center of the tank. Averaged over all positions and directions the 50% point is reached at 4.6 MeV. The difference is due to light attenuation (the average path length of a Cherenkov photon is biggest at the center, if all directions are considered). For a uniform detector response a low energy threshold of about 7 MeV is implied.

Elastic neutrino-electron scattering is strongly forward peaked. To separate the solar neutrino signal from background events, this directional correlation is exploited. Angular

(a) (b)

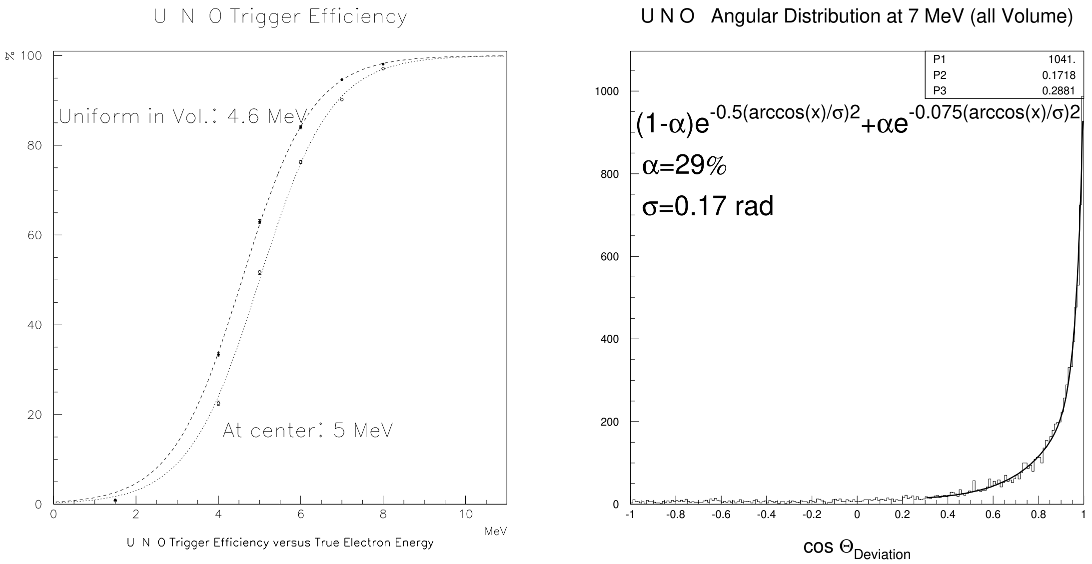

Figure 4.19: Monte Carlo Trigger Efficiency for low energy electrons as a function of input energy (a) and cosine of the deviation angle (for 7 MeV electrons) between reconstructed and input direction (b).

resolution is limited by multiple scattering. Figure 4.19b shows the deviation angle between reconstructed and input direction from Monte Carlo. The reconstruction algorithm first reconstructs the vertex from the PMT times and then the direction assuming a single Cherenkov cone originating from the reconstructed vertex. Reconstructing 7 MeV events in UNO seems not to be a problem.

'Vertex resolution' is defined as the radius of a sphere around the true electron production point which contains 68% of all reconstructed vertex points. Similarly, 'angular resolution' is the opening angle of a cone around the true direction containing 68% of all reconstructed directions. Figure 4.20 shows that vertex and angular resolution are sufficiently small above 5 MeV. Naturally, vertex resolution is the largest in the center. The angular resolution, however, is smallest in the center. (Most likely, this is a geometric effect, since the solid angle of the average tube for a near-wall event is larger than for an event in the center.)

4.6 Neutrino Astrophysics

Neutrinos offer a unique probe for investigation of the deep universe, the far side of our own Galaxy, and the interiors of astrophysical objects.

Charged cosmic ray particles are deflected by Galactic (and perhaps inter-galactic) magnetic fields and lose all memory of their original direction. Only at the highest energies ($\geq 10^{19}$ eV) are charged cosmic ray trajectories likely to correlate with their sources, and at

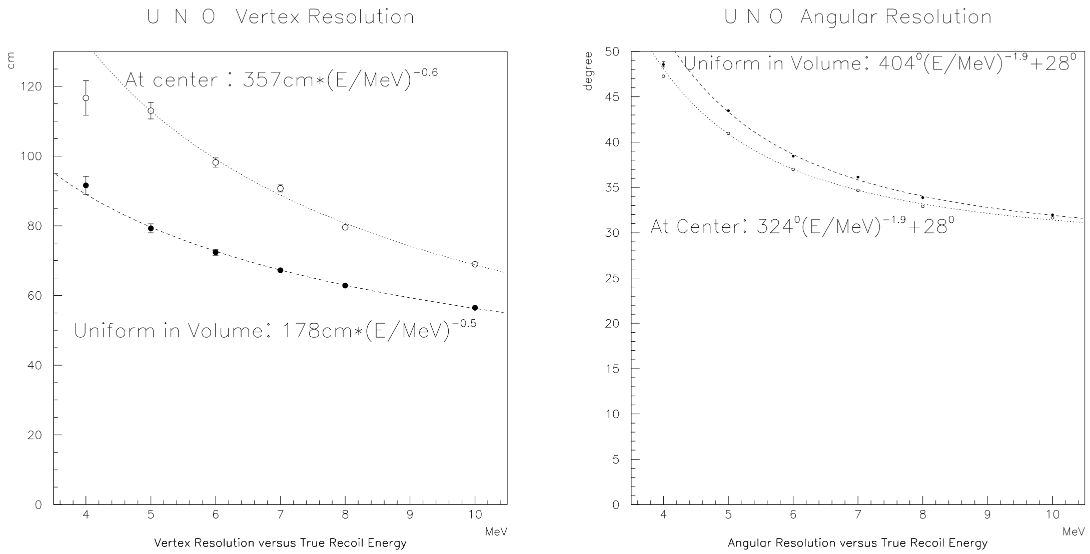

Figure 4.20: Vertex and Angular Resolution (for low energy electrons) from Monte Carlo as a function of input energy.

these extreme energies, interactions with cosmic background radiation (CBR) photons make the universe opaque beyond distances of a few 10s of Mpc.

Conventional astronomy is based on observations of photons, which are subject to a variety of absorption processes, depending upon energy. In any case, photons are emitted only by the surface layers of astrophysical source objects. Neutrinos are the only way we can directly observe objects in the nucleus of our Galaxy, or on the far side of the Galactic disk.

Huge detectors may be needed to do detailed observational neutrino astrophysics. But the field is still in the exploration phase; the fact is that no direct observation of a non-transient neutrino source more distant than the Sun has ever been made, despite the fact that neutrinos must be produced by the same meson decay processes that produce high energy gamma rays, in proportionate abundance. Furthermore, underground neutrino detectors can provide enormous effective mass by the well-developed technique of detecting upward-going muons. These must be products of neutrino interactions in the rock beneath the detector, since no other cosmic ray particle could penetrate the Earth to produce them.

The next generation of high-energy neutrino detectors can contribute also to other areas of research such as geophysics. The highest energy neutrinos observable with UNO, via upward going muon events, are significantly absorbed by the Earth, and thus may be used to map the density profiles of the Earth's mantle and core [78].

4.6.1 Sources of Astrophysical Neutrinos

Astrophysical sources of high energy gamma rays provide a list of potential sources of neutrinos. The EGRET detector aboard the Compton Gamma Ray Observatory (CGRO) satellite has cataloged sources up to 30 GeV [79]. The BATSE experiment [80] on CGRO detected thousands of gamma-ray bursts, and the Italian-Dutch BeppoSAX satellite [81] supplied position measurements with accuracy $\sim 4'$ of arc for bursts it observed. Ground based detectors can observe TeV gamma rays. The Milagrito water Cherenkov shower detector found a correlation with a BATSE-cataloged GRB [82]. Cherenkov telescopes at ground level, such as the Whipple observatory, HEGRA, Cangaroo and University of Durham Mark 6 telescopes, have so far detected several sources emitting gamma-rays well above 100 GeV.

The observation of TeV gamma rays from the sources mentioned demonstrates the possible existence of "heavenly beam dumps" [83, 84] which should be producing high energy neutrinos as well as gamma rays.

If cold dark matter the annihilation rate exists in the Galactic Center in the form of neutral particles that can annihilate, such as the supersymmetric neutralino, it can be accreted by the black hole which is almost certainly present there. Neutrinos can escape and produce observable fluxes [85].

4.6.2 Current Experimental Results

Previously, limits on point-like high energy neutrino sources were obtained by the Kolar Gold Field (KGF) experiment [86], and by the IMB [87] and Kamiokande [88] water Cherenkov detectors. Super-Kamiokande [89] [90], Baksan [91] and AMANDA [92] have presented preliminary results at conferences. The most comprehensive published results have been from MACRO [93].

Observations of PeV (10^{15} eV) and EeV (10^{18} eV) gamma rays are controversial, but cosmic rays of EeV energies certainly exist, and their origin is at present a mystery. Cosmic rays with energies up to $\sim 10^{15}$ eV are generally believed to be accelerated by supernova shocks driven into the interstellar medium. To accelerate particles to 10^{20} eV would require a 100 G magnetic field extending over thousands of light years. Such intense and extensive fields may exist near the supermassive black holes which are thought to power active galactic nuclei (AGNs). Thus the highest high-energy cosmic rays (and neutrinos) are produced in distant galaxies and can carry cosmological information.

Observations of TeV photons from the nearby (z=0.03) giant elliptical galaxy Markarian 421 [94] may be evidence for such processes. Mrk 421 is nearby, but not a particularly powerful AGN. Similarly, the Whipple observatory detected TeV emission from the blazar Mrk 501 with redshift z = 0.018, a source not found in the Compton GRO catalog. One explanation is that AGNs may have significant, very high-energy gamma ray emission, but only nearby AGNs can be detected due to photon absorption in inter-galactic space. The need for neutrino detectors is therefore obvious.

Known AGNs at distances 100 Mpc, with proton luminosities on the order of 10^{45} erg/s or higher are candidate sources of the highest energy cosmic rays. Their proton flux, propagated to the Earth, can explain the cosmic-ray spectrum in the EeV range [95]. Conservative estimates of the corresponding neutrino flux yield 300 upward-going muons per year in a neutrino detector with $10^6 \mathrm{m}^2$ effective area.

4.6.3 Point-Source Sensitivity

The Super-Kamiokande detector records about 1.4 upward going muons events (with muon track length > 7 m) per live day in its 22.5 kt fiducial volume and sets flux limits on the order of $10^{-15}\mathrm{cm}^{-2}\mathrm{sec}^{-1}$ for several potential sources [96]. For Super-Kamiokande, upward stopping muons have parent neutrino energies around 10 GeV, and through-going upward muons have mean parent neutrino energies around 100 GeV. UNO will reach comparable limits after a few months' operation, and more importantly, will reach into a higher energy range, where astrophysical sources stand out more clearly above the uniform background of atmospheric neutrinos.

UNO can make significant contributions to neutrino astrophysics by detecting upward-going muon events, caused by neutrino interactions in the Earth below the detector. These events represent the highest-energy sample of neutrino interactions the experiment can collect. Searches can be performed and new limits set for a variety of physics areas such as

- Point sources of high energy neutrinos such as AGNs,
- WIMP annihilations at the center of the Earth, the Sun and our Galaxy,
- Neutrinos from GRBs.

Similar searches can be done using lower energy neutrinos as well.

In addition, a neutrino detector the size of UNO will allow us for the first time to observe astrophysical objects at the center and on the far side of our Galaxy. Full exploitation of the physics available will eventually require a km^3-scale detector, with higher directional resolution than any existing or projected undersea or under-ice detector. However, UNO can provide a practical beginning for the long-desired exploration of UHE neutrino astrophysics.

4.7 Bibliography

[1] Kamiokande Collab., K. S. Hirata, Phys. Lett. **B205**, 416; *ibid.* **280**, 146 (1992); Y.Fukuda et al., Phys. Lett. **B335**, 237 (1994); S. Hatakeyama et al. Phys. Rev. Lett. **81**, 2016 (1998).

[2] IMB Collab., D. Casper et al., Phys. Rev. Lett. **66**, 2561 (1991); R.Becker-Szendy et al., Phys. Rev. **D46**, 3720 (1992); Phys. Rev. Lett. **69**, 1010 (1992).

[3] Y. Fukuda et al., Phys. Lett. **B433**, 9 (1998); Phys. Rev. Lett. **81**,1562 (1998); *ibid.*, **82**, 2644 (1999); Phys. Lett. **B467**, 185 (1999); H. Sobel, in Neutrino-2000, T. Toshito, in ICHEP-2000. Recent discussions of flux calculations are T. Gaisser, Nucl. Phys. (Proc.

Suppl.) **87**, 145 (2000); P. Lipari, Astropart. Phys. **14**, 153 (2000); G. Battistoni, hep-ph/0012268; G. Fiorentini, V. Naumov, and F. Villante, hep-ph/0103322.

[4] W. Allison et al., Phys. Lett. **B449**, 137 (1999), A. Mann, talk at Neutrino-2000, hep-ex/0007031.

[5] M. Ambrosio et al., Phys. Lett. **B478**, 5 (2000); B. Barish, talk at Neutrino-2000.

[6] I. Mocioiu and R. Shrock, hep-ph/0106139.

[7] M. Apollonio et al., Phys. Lett. **B420**, 397 (1998); Phys. Lett. **B466**, 415 (1999).

[8] Fits and references to the Homestake, Kamiokande, GALLEX, SAGE, and Super Kamiokande data include N. Hata and P. Langacker, Phys. Rev. **D56** 6107 (1997); J. Bahcall, P. Krastev, and A. Smirnov, Phys. Rev. **D58**, 096016 (1998); J. Bahcall and P. Krastev, Phys. Lett. **B436**, 243 (1998); J. Bahcall, P. Krastev, and A. Smirnov, Phys. Rev. **D60**, 093001 (1999); J. Bahcall, P. Krastev, and A. Smirnov, hep-ph/0103179; M. Gonzalez-Garcia, C. Peña-Garay, and J. W. F. Valle, Phys. Rev. **D63**, 013007; M. Gonzalez-Garcia, M. Maltoni, C. Pena-Garay, and J. W. F. Valle, Phys. Rev. **D63**, 033005 (2001). Recent discussions of flux calculations are in J. Bahcall, Phys. Rept. **333**, 47 (2000), talk at Neutrino-2000, and http://www.sns.ias.edu/ jnb/. Super Kamiokande data is reported and analyzed in Super Y. Fukuda et al. (SuperKamiokande Collab.), Phys. Rev. Lett. **82**, 1810, 243 (1999); S. Fukuda et al. (SuperKamiokande Collab.), hep-ex/0103032, hep-ex/0103033. For recent reviews, see e.g., Y. Suzuki, talk at Neutrino-2000, Int'l Conf. on Neutrino Physics and Astrophysics, http://www.nrc.ca/confserv/nu2000/, Y. Takeuchi at ICHEP-2000, Int'l Conf. on High Energy Physics, Osaka, http://ichep2000.hep.sci.osaka-u.ac.jp; and talks at the Fifth Topical Workshop at the Gran Sasso National Laboratory: Solar Neutrinos, Mar., 2001.

[9] L. Wolfenstein, Phys. Rev. **D17**, 2369 (1978).

[10] S. P. Mikheyev and A. Smirnov, Yad. Fiz. **42**, 1441 (1985) [Sov.J. Nucl. Phys. **42**, 913 (1986)], Nuovo Cim., **C9**, 17 (1986); S. P. Rosen and J. Gelb, Phys. Rev. **D34**, 969 (1986); S. Parke, Phys. Rev. Lett. **57**, 1275 (1986); W. Haxton, Phys. Rev. Lett. **57**, 1271 (1986); J. Pantaleone and T. K. Kuo, Rev. Mod. Phys. **61**, 937 (1989).

[11] LSND Collab., C. Athanassopoulous et al., Phys. Rev. Lett. **77**, 3082 (1996), LSND Collab., C. Athanassopoulous et al., Phys. Rev. Lett. **81**, 1774 (1998); K. Eitel, in Neutrino-2000.

[12] KARMEN Collab., K. Eitel, in Proceedings of Neutrino-2000, Nucl. Phys. (Proc. Suppl.) **91**, 191 (2000).

[13] References and websites for these experiments and future projects can be found, e.g., at http://www.hep.anl.gov/ndk/hypertext/nu_industry.html.

[14] M. Sakuda and K. Nishikawa, talks at ICHEP-2000, Osaka; S. H. Ahn et al, hep-ex/0103001.

[15] OPERA Collab., CERN-SPSC-97-24, hep-ex/9812015.

[16] ICARUS/ICANOE Collab. F. Cavanna et al., LNGS-P21-99-ADD-1,2, Nov 1999; A. Rubbia, hep-ex/0001052.

[17] Y. Itow et al. JHF Neutrino Working Group), Letter of Intent: a Long Baseline Neutrino Oscillation Experiment using the JHF 50 GeV Proton Synchroton and the Super-Kamiokande Detector (Feb. 2000).

[18] G. L. Fogli, E. Lisi, A. Marrone, and G. Scioscia. Super-kamiokande data and atmospheric neutrino decay. *Phys. Rev.*, D59:117303, 1999; Ernest Ma, G. Rajasekaran, and Ion Stancu. Hierarchical four-neutrino oscillations with a decay option. *Phys. Rev.*, D61:071302, 2000; V. Barger et al. Neutrino decay and atmospheric neutrinos. *Phys. Lett.*, B462:109–114, 1999.

[19] C. Albright et al.,"Physics at a Neutrino Factory" (April, 2000), hep-ex/0008064.

[20] Muon Collider and Neutrino Factory Collaboration, "Feasibility Study II", www.cap.bnl.gov/mumu/studyii.

[21] Z. Parsa, in Proceedings of NNN99, A.I.P. Conf. Proc. 533, pp. 181–195 (A.I.P., New York, 1999).

[22] V. Barger, K. Whisnant, S. Pakvasa, and R. J. N. Phillips, Phys. Rev. **D22**, 2718 (1980); V. Barger, K. Whisnant, and R. J. N. Phillips, Phy. Rev. Lett. **45**, 2084 (1980).

[23] L. Sulak, in *First Workshop on Grand Unification* (Math Sci. Press, 1980), p. 163; D. Ayres, T. Gaisser, A. K. Mann, and R. Shrock, in *Proceedings of the 1982 DPF Summer Study on Elementary Particles and Future Facilities*, Snowmass, p. 590; D. Ayres, B. Cortez, T. Gaisser, A. K. Mann, R. Shrock, and L. Sulak, Phys. Rev. **D29**, 902 (1984).

[24] P. Krastev, S. Petcov, Phys. Lett. **B205**, 8 (1988).

[25] A. J. Baltz, J. Weneser, Phys. Rev. **D37**, 3364 (1988).

[26] S. Petcov, Phys. Lett. **B434**, 321 (1998). M. Chizhov, M. Maris, S. Petcov, hep-ph/9810501; M. Chizhov, S. Petcov, Phys. Rev. **D63**, 073003 (2001); M.Chizhov, S.Petcov, Phys. Rev. Lett. **83**, 1096 (1999).

[27] E. Akhmedov, A. Dighe, P. Lipari, A. Smirnov, Nucl. Phys. **B542**, 3 (1999); E. Akhmedov, Nucl.Phys. **B538**, 25 (1999); hep-ph/0001264.

[28] P. Krastev, Nuovo Cimento **103A**, 361 (1990); R. H. Bernstein and S. J. Parke, Phys. Rev. **D44**, 2069 (1991).

[29] S. Geer, Phys. Rev. **D57**, 6989 (1998).

[30] De Rujula, M. B. Gavela, and P. Hernandez, Nucl. Phys. **B547**, 21 (1999).

[31] V. Barger, S. Geer, K. Whisnant, Phys.Rev. **D61**, 053004 (2000).

[32] M. Campanelli, A. Bueno, A. Rubbia, hep-ph/9905240; P. Lipari, Phys. Rev. D61, 113004; D. Dooling, C. Giunti, K. Kang, C. W. Kim, Phys. Rev. **D61** (2000) 073011.

[33] I. Mocioiu, R. Shrock, Phys. Rev. **D62**, 053017 (2000); Proceedings of NNN99, A.I.P. Conf. Proc. 533, pp. 74–79 (A.I.P., New York, 1999).

[34] V. Barger, S. Geer, R. Raja, K. Whisnant, Phys. Rev. **D62**, 013004, *ibid.* **D62**, 073002 (2000); Phys. Lett. **B485**, 379 (2000); Phys. Rev. **63**, 033002 (2001).

[35] A. Cervera, A. Donini, M.B. Gavela, J. Gomez Cadenas, P. Hernandez, O. Mena, and S. Rigolin, Nucl. Phys. **B579**, 17 (2000), Erratum-ibid. **B593**, 731 (2001).

[36] M. Freund, T. Ohlsson, Mod. Phys. Lett. **15**, 867 (2000); T. Ohlsson, H. Snellman, J. Math. Phys. **41**, 2768 (2000); Phys. Rev. **D60** 093007 (1999); Phys. Lett. **B474**, 153 (2000); M. Freund, M. Lindner, S.T. Petcov, A. Romanino, Nucl. Phys. **B578**, 27 (2000); M. Freund, P. Huber, M. Lindner, Nucl. Phys. **B585**, 105 (2000); M. Freund, M. Lindner, and S. Petcov. Nucl. Instrum. Meth. **A451**, 18 (2000); K. Dick, M. Freund, P. Huber, and M. Lindner, Nucl. Phys. **B588**, 101; Nucl. Phys. **B598**, 543 (2001).

[37] S.M. Bilenky, C. Giunti, W.Grimus, Phys.Rev.**D58**, 033001 (1998); K. Dick, M. Freund, M. Lindner, A. Romanino, Nucl. Phys. **B562**, 29 (1999); M. Tanimoto, Phys. Lett. **B462**, 115 (1999); A. Donini, M.B. Gavela, P. Hernandez, Nucl. Phys. **B574**, 23 (2000); M. Koike and J. Sato, Phys. Rev. **D61** 073012 (2000); Erratum-ibid. **D62**, 079903 (2000); M. Koike and J. Sato, Phys. Rev. **D62**, 073006 (2000); M. Koike, T. Ota, and J. Sato, hep-ph/0011387; F. Harrison, W.G. Scott, hep-ph/9912435.

[38] B. Richter, hep-ph/0008222.

[39] M.Spiro, "A low energy neutrino superbeam experiment", talk presented at the CERN Muon Plenary Week, May 7–10, 2001, see http://muonstoragerings.web.cern.ch/muonstoragerings/Events/20010507/spiro.pdf

[40] V. Barger, R. Bernstein, A. Bueno, M. Campanelli, D. Casper, F. DeJongh, S. Geer, M. Goodman, D.A. Harris, K.S. McFarland, N. Mokhov, J. Morfin, J. Nelson, F. Peitropaolo, R. Raja, J. Rico, A. Rubbia, H. Schellman, R. Shrock, P. Spentzouris, R. Stefanski, L. Wai, K. Whisnant, FERMILAB-FN-703, hep-ph/0103052.

[41] V. Barger, S. Geer, R. Raja, K. Whisnant, hep-ph/0012017.

[42] See the talk by C. McGrew in Proceeding of NOON Workshop, Kashiwa, Japan, December 2000 and in Proceeding of Workshop on Neutrino Telescope, Venice, March 2001.

[43] See, e.g., the Workshop on Physics Potentials at FNAL with Stronger Proton Beams, www-bd.fnal.gov/pdriver/.

[44] J. J. Gomez-Cadenas *et al.* [CERN working group on Super Beams Collaboration], hep-ph/0105297.

[45] A. Blondel, S. Gilardoni and M. Donega, CERN-NUFACT-NOTE-53.

[46] In this series, for NuFact01, see http://psux1.kek.jp/ nufact01.

[47] R. Becker-Szendy *et al.*, Nucl. Instrum. Meth. A **324**, 363 (1993).

[48] K. S. Hirata *et al.* [Kamiokande-II Collaboration], Phys. Lett. B **280**, 146 (1992).

[49] Y. Fukuda *et al.* [Super-Kamiokande Collaboration], Phys. Lett. B **433**, 9 (1998) [hep-ex/9803006].

[50] B. Autin *et al.*, CERN-2000-012.

[51] M. D. Messier, UMI-99-23965.

[52] M. Shiozawa [Super-Kamiokande Collaboration], Nucl. Instrum. Meth. A **433**, 240 (1999).

[53] S. Kasuga *et al.*, Phys. Lett. B **374**, 238 (1996).

[54] T. Barszczak, University of California, Irvine Ph.D thesis (to be published).

[55] We wish to thank the Super-Kamiokande collaboration for allowing use of its simulation and analysis software in this study.

[56] M. G. Catanesi *et al.*, CERN-SPSC-99-35.

[57] J. Burguet-Castell, M. B. Gavela, J. J. Gomez-Cadenas, P. Hernandez and O. Mena, hep-ph/0103258.

[58] Y. Fukuda *et al.* [Super-Kamiokande Collaboration], Phys. Rev. Lett. **81**, 1562 (1998) [hep-ex/9807003].

[59] W. A. Mann [Soudan-2 Collaboration], Nucl. Phys. Proc. Suppl. **91**, 134 (2000) [hep-ex/0007031].

[60] M. Ambrosio *et al.* [MACRO Collaboration], Phys. Lett. B **478**, 5 (2000).

[61] G. J. Feldman and R. D. Cousins, Phys. Rev. D **57**, 3873 (1998) [physics/9711021].

[62] M. Apollonio *et al.* [CHOOZ Collaboration], Phys. Lett. B **466**, 415 (1999) [hep-ex/9907037].

[63] J. F. Beacom, R. N. Boyd and A. Mezzacappa, Phys. Rev. D **63**, 073011 (2001) [astro-ph/0010398].

[64] K. Hirata *et al.*, Phys. Rev. Lett. **58**, 1490 (1987).

[65] R.M. Bionta *et al.*, Phys. Rev. Lett. **58**, 1494 (1987).

[66] P. Galeotti *et al.*, Helv. Phys. Acta **60**, 619 (1987).

[67] J. Bahcall and R. Soneira, Astrophys. J. 238 L17 (1980); J. Bahcall and T. Piran, Astrophys. J. 267 L77 (1983).

[68] K. Langanke, P. Vogel, and E. Kolbe, Phys. Rev. Lett. **76**, 2629 (1996).

[69] J.F. Beacom, R.N. Boyd, and A. Mezzacappa, Phys. Rev. Lett. **85**, 3568 (2000).

[70] J. A. Pons, J. A. Miralles, M. Prakash and J. M. Lattimer, astro-ph/0008389; J. A. Pons, S. Reddy, M. Prakash, J. M. Lattimer and J. A. Miralles, Astrophys. J. **513**, 780 (1999)

[71] Y. Fukuda et al., Phys. Rev. Lett. **77**, 1683 (1996).

[72] S. Fukuda et al., hep-ex/0103032.

[73] J. N. Bahcall et al., Phys. Lett. **B433** 1–8 (1998), astro-ph/9805135.

[74] J.N.Bahcall et al., astro-ph/0010346: $\phi_{^8\mathrm{B},\ \mathrm{Hep}} = (5.15, 0.0093) \times 10^6/\mathrm{cm}^2\mathrm{s}$

[75] E. V. Bugaev et al., Phys.Rev. D58 (1998) 054001

[76] M. Nakahata et al., Nucl. Instrum. Methods Phys. Res. Sect. A 421, 113 (1999).

[77] E. Blaufuss et al., Nucl. Instrum. Methods Phys. Res. Sect. A 458, 636 (2001).

[78] P. Bosetti, et al., (DUMAND Collaboration), Proc. XXII ICRC, 4 (1991) 670.

[79] R. C. Hartman et al., ftp://gamma.gsfc.nasa.gov/pub/THIRDCATALOG/.

[80] W.S. Paciesas et al., The fourth BATSE Gamma-Ray burst Catalog, astro-ph/9903205 (1999); the latest BATSE Catalog can be downloaded from http://gammaray.msfc.nasa.gov/batse/.

[81] F. Frontera, Proc. XXV ICRC, 8 (1997) 307.

[82] J. E. McEnery et al., astro-ph/9910549 (1999).

[83] V. S. Berezinsky, C. Castagnoli and P. Galeotti, Il Nuovo Cimento 8C (1985) 185.

[84] T. K. Gaisser, F. Halzen and T. Stanev, Phys. Rep. 258 (1995) 173.

[85] P. Gondolo and J. Silk, Phys. Rev. Lett. 83 (1999) 1719.

[86] H. Adarkar et al., KGF Collaboration, Astrophys. J. 380 (1991) 235; Proc. XXIV ICRC, 1 (1995) 820.

[87] R. Svoboda et al., IMB Collaboration, Astrophys. J. 315 (1987) 420; R. Becker-Szendy et al., Astrophys. J. 444 (1995) 415, R. Becker-Szendy et al., Nucl. Phys. B (Proc. Suppl.) 38 (1995) 331.

[88] Y. Oyama et al., Phys. Rev. D39 (1989) 1481.

[89] J.G. Learned for the Super-Kamiokande Collaboration, Proc. XXV ICRC, 7 (1997) 73.

[90] The Super-Kamiokande Collaboration, Phys.Lett. B467 (1999) 185.

[91] M. M. Boliev et al., Baksan Collaboration, Proc. XXIV ICRC, 1 (1995) 722.

[92] K. John for the AMANDA Collaboration, Proc. XXVI ICRC, 2 (1999) 196.

[93] M. Ambrosio, et al. (The MACRO Collaboration), Astrophys.J. 546 (2001) 1038.

[94] M. Punch et al., Nature 358, 477 (1992).

[95] K. Mannheim and P.L. Biermann, Astron. Astrophys. 253, L21 (1992) and 22, 211 (1989).

[96] S. Matsuno, for the Super-Kamiokande Collaboration, to be published in Proc. XXVII ICRC (2001).

Chapter 5

Site Studies

Since the NNN99 Workshop, there has been considerable progress in the search for UNO detector sites. The WIPP (Waste Isolation Pilot Plant) at Carlsbad, New Mexico was the first to emerge, both as a potential site for UNO and as a national underground laboratory. The site is owned and operated by United States Department of Energy, and has extensive established infrastructure which can be exploited for underground scientific research.

The Homestake mine that has been home for Ray Davis' solar neutrino experiment for the last three decades became a potential site for UNO and a national underground laboratory when in the fall of year 2000 the mine company announced closure of the mine for mining gold. This site has advantage of the existing mine shafts and tunnels, as well as extraordinary depth (as deep as 8,000 feet). This depth makes it a favored location for solar neutrino and neutrinoless double beta-decay experiments which are very sensitive to cosmic ray-related backgrounds.

The San Jacinto mountain site, about 20 miles from Palm Springs, California is currently undeveloped. It was first considered for a national underground laboratory in the early 1980's due to its steep gradient and proximity to major research universities and services. This site's advantages are the possibility of horizontal access as well as an exordinary depth of up to 8,000 feet.

In the following we survey the characteristics of these sites in more detail. In addition to these sites, the Fréjus tunnel in France is under consideration. In conjunction with the addition of a safety tunnel at this site, the possibility of building a cavern for an UNO-sized water Cherenkov detector has been discussed [1]. The Fréjus site combines the advantages of several others (horizontal access and great depth) with proximity to CERN, facilitating a sensitive long-baseline neutrino oscillation experiment with a low-energy beam to UNO, as described in Section 4.3.2.1.

5.1 Homestake Mine

On September 11, 2000, the Homestake Mining Company announced that all gold mining would cease by the end of 2001 at its Lead, South Dakota mine. This mine is the deepest in the United States with over 50 separate levels between the surface of the Earth and a depth of 8000 ft. At a meeting in Berkeley on March 3–4, 2001, the National Underground Laboratory Advisory Committee decided that the depth of the mine, the strength of the rock, the absence of seismic activity, the existing infrastructure and immediate availability of the site, made the Homestake mine an excellent choice as the site of the National Underground Science Laboratory. This recommendation has been forwarded to both NSF and DOE.

The Homestake Laboratory will be operated as a pure science national facility. Barring unforeseen developments, it is expected that construction of underground laboratory chambers will begin early in 2002 and useful occupancy of the first chambers will be possible later that year.

5.1.1 Homestake Characteristics

Since Homestake is an operating mine, it has a complete operational infrastructure that is in full compliance with MSHA regulations. There is multiple (two shaft and/or ramp) access to all levels. The mine has an excellent ventilation system, 20 megawatts of AC power, T3 fiber optic cable connecting the surface to many underground locations, mine rails and associated rolling stock on most levels, and about 40,000 sq. ft. of office and potential laboratory space on the surface. The mine has a highly skilled and experienced group of miners and mine engineers. It is expected that a significant fraction of these people will remain to construct and operate the underground laboratory.

The two main elevator shafts, the Yates and the Ross-Winze6, are separated by about 3000 ft. There are horizontal connecting tunnels between these shafts at a number of levels, in particular at the 4850 ft level. One of the first construction plans for the laboratory is to build a similar connecting tunnel at the 7400 ft level. The main connecting tunnels at the 4850 ft and 7400 ft levels will serve as the access tunnels to laboratory chambers at these levels. Fresh air will flow into the laboratory chambers through these access tunnels and then be exhausted via a set of tunnels at the far end of each of the laboratory chambers.

In addition to the laboratory chambers, each of these levels will have local support facility rooms such as lounges for meetings and snacks, local machine shops, etc. It is anticipated that the elevator system, the access tunnels and the laboratory and lounge rooms will be maintained as clean facilities similar to those in normal surface laboratories.

Present plans are to modify the Yates shaft so that it can transport a standard 20 ft by 8 ft by 8 ft shipping container from the surface to any underground level. Depending on availability of funds, this shaft modification may take several years to complete. Until then, dimensions of detector components that can be taken underground will be limited by the aperture of the present mine elevators, 4.5 ft wide by 12 ft deep. The height is flexible.

There are plans to augment the existing surface facilities with a new laboratory/office building that will be designed to support the underground research activities. This building will include a large, high bay assembly and test area in which experiments can be set up and tested before underground deployment. There will also be a variety of electronic, chemical and computing facilities.

The Homestake mine is in the town of Lead. Lead is in the middle of the Black Hills and is surrounded by the Black Hills National Forest. There are skiing facilities within 10 minutes of Lead, numerous lakes are nearby, and there are wonderful hiking and biking trails throughout the area. Since the nearby town of Deadwood has legalized gambling, the area has numerous motels and restaurants.

The Black Hills State University is 15 miles away in Spearfish and the South Dakota School of Mines and Technology is 50 miles away in Rapid City.

The Rapid City airport is about 55 miles (1 hour) away. Rapid City is served by United, Northwest and Delta airlines with 19 to 25 flights per day to Denver, Minneapolis and Salt Lake City.

5.1.2 UNO Chamber Construction

In the fall of 2000, mining engineers at the Spokane Laboratory of NIOSH, the successor to the Bureau of Mines, evaluated the construction of a 200 ft diameter by 400 ft long cylindrical chamber at 4850 ft and 6800 ft, in the Homestake Mine. At that time of this study, the depth of the deep laboratory site had not been decided.

The NIOSH study used measured Homestake rock strengths and included appropriate safety factors. Their conclusion was that this excavation would be safe and stable at either depth. Of course, this is only a preliminary study. A much more careful evaluation that includes local rock structure must be carried out before actual excavation begins. Since the Homestake Company has excavated large caverns below 7000 ft and NIOSH was involved in the pre-excavation planning for these excavations, it is reasonable to assume that the NIOSH evaluation is reliable.

Although it is difficult to make reliable cost predictions for this excavation, a crude estimate is between \$70 and \$100M. At this level of estimation, there is no difference in cost between the two Homestake levels, although it is quite likely that construction at the deeper level will cost more.

The measured angle integrated cosmic ray muon flux at the 4850 ft level is 4 muons /m^2 day. It is anticipated that the corresponding flux at the 7400 ft level will be a factor 10 smaller.

The construction time is unlikely to be less than 3 years and may be considerably longer.

5.1.3 Vertical Cylinder Design

One of the low cost and efficient mining techniques used at Homestake is Vertical Crater Retreat (VCR). This involves excavating a vertical cylinder between two levels (150 ft high) by drilling blasting holes through the excavation region from above and then blasting out pancake sections from the bottom up. A rock chute is first created at the bottom so the blasted rock can be easily removed.

The VCR technique is very efficient and relatively inexpensive. A 50 meter high by 50 meter diameter vertical cylinder could be excavated by this technique. After the excavation is completed, the rock chute would be sealed and the excavation lined with a water tight rubber or plastic bladder.

The resulting 100,000 m^3 cylinder would result in a detector that is about twice the volume of Super-Kamiokande. Although no estimates for the construction cost have been made, it may be possible to carry out this excavation for about $10M and carry out the construction in a year or so. Construction of this detector on the 4850 ft level would be particularly efficient since the waste rock could be conveyed directly to a nearby rock dump.

5.1.4 Next Steps

We hope to have an engineering planning meeting at Homestake in the fall of 2001. The goal of that meeting will be to acquaint the mine engineers with the specific requirements of potential underground experiments. This planning process will help the experimentalists in specifying the requirements for their chambers and help the mining engineers in formulating the plans for underground construction. This session will also help the underground safety group formulate operating procedures for dealing with experimentalists and formulation of their policies and procedures. It would be most useful to have a set of preliminary UNO chamber specifications available in time for that meeting.

5.2 San Jacinto Mountain

The San Jacinto escarpment is one of the steepest and tallest fault bluffs in the United States. This unusual geologic formation allows deep underground access via a modest horizontal bore into the mountain. The maximum available overburden at San Jacinto is over 2,500 m of hard rock (7000 m water equivalent). The resulting reduction in penetrating cosmic rays leads to cosmogenic background rates so low that all manner of low-rate, low-background physics experiments could be performed at this site. Furthermore, as one drills into mountain, overburdens of all intermediate thickness become available for less sensitive, larger-volume projects such as nucleon decay searches and long-baseline neutrino oscillation studies.

In addition to ready access to a range of overburdens, there are numerous reasons why horizontal access is always favored over vertical shaft access for an underground facility: excavation, detector construction, and continuing operations are not tied to nor constrained by a hoist schedule; the size of experimental components are not limited by a critical lift's dimensions or its weight capacity; operating costs are low and are virtually independent of depth; safety is enhanced since emergency egress is not compromised by concurrent power failure.

Located in populous and high-tech southern California, San Jacinto enjoys close proximity to many important assets essential in the creation and ongoing support of a world-class scientific facility. Nowhere else in the world are so many major research and teaching universities, with their supplies of researchers, students, and trained support staff, concentrated so close to a proposed underground laboratory. The city of Palm Springs, a well-known resort destination, is just 20 minutes away from the portal area. Collaborators and equipment can

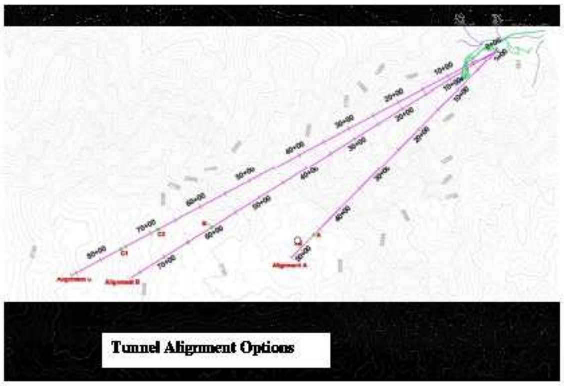

Alignment	Tunnel Length (m)	Grade (%)	Ground Elevation at Cavern Complex (m)	Shielding (mwe)
A	4650	1	2543	5000
B	6000	1	2906	6000
C	7600	1	3173	6510
	6850	-5	3010	7000

Figure 5.1: Tunnel alignment options.

travel to and from the site via several nearby international airports and well-maintained highways, while hotels, apartments, office buildings, construction companies, and other necessary resources are available in abundance in the surrounding vicinity.

5.2.1 Proposed Facilities and UNO Site

The San Jacinto National Underground Science Laboratory (NUSL) facilities consist of administration, warehouse and assembly buildings located in or near Palm Springs at the base of San Jacinto Mountain, and the underground laboratory located beneath the Mountain. Access to the underground laboratory complex is via a portal near the Valley Station of the Palm Springs Aerial Tramway. One tunnel provides access from the portal to the underground cavern complex.

One of the many advantages offered by the San Jacinto site is the range and magnitude of shielding available. Four shielding options are offered, although many intermediate options are possible. Shielding of 5,000 mwe, 6,000 mwe and 6,510 mwe are possible with access tunnels that have a 1% up grade from the portal to the cavern complex. Shielding of 7,000 mwe is possible with a down grade tunnel. Tunnel lengths for these shielding options are 4.6 km to 7.6 km. Figure 5.1 shows the possible tunnel options and a table that summarizes characteristics of each option.

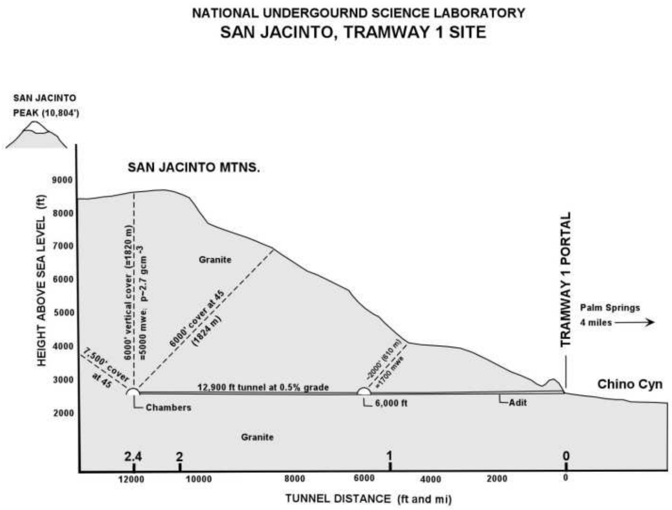

Figure 5.2: A cut-out view of one of the tunnel options.

A cross section of one of the tunnel options is shown in Figure 5.2.

The underground cavern complex proposed for the San Jacinto NUSL would have ready access from parking, storage and common areas to the experimental caverns, large-scale tunnel access to center of caverns, room for expansion, and the capability to expand by constructing new caverns without significantly impacting ongoing experiment (See Figure 5.3). Three experimental caverns, each 20m×20m×100m, are provided. In addition, there is a parking and storage cavern located off the main tunnel at the entrance to the complex. A common area cavern provides space for common functions and services, and is high enough for four stories. The refuge cavern and a combination drainage pump and fire reservoir complete the layout of the basic complex.

The expected stability of the granite monolith from which the mountain is built should allow the construction of the large chamber needed by UNO. Our estimate of the cost of a chamber 50m×50m×200m is approximately \$82M, competitive with current estimates in other hard rock locations. This location is across the road from the other caverns, and is also below the grade of the main complex. This cavern is accessed during the construction by a short tunnel from the main tunnel to the upper level, and by a long, inclined tunnel to the bottom. The inclined tunnel would likely be sealed after experiment construction or allowed to fill during cavern filling. A 20m×20m×50m support cavern for the large UNO cavern is also provided.

5.2.2 Schedule

Construction of the access tunnel and the basic infrastructure of the San Jacinto NUSL is estimated to be about five years for the date of approval. Excavation of the UNO chamber

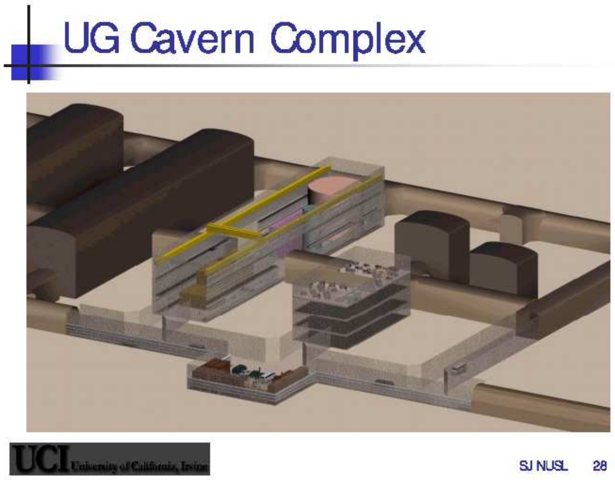

Figure 5.3: Underground cavern complex.

would begin four years into this period and would take three to five years.

5.3 WIPP (Waste Isolation Pilot Plant)

The Waste Isolation Pilot Plant (WIPP) is located about 30 miles from Carlsbad, New Mexico at a depth of 655 m in halite of the Permian Salado formation. This formation is a bedded evaporite deposit of nearly pure salt, with a thickness of about 650 m, and is underlain by more salt and anhydrite beds of the Castile formation, down to a depth of about 1300 m. The WIPP has been developed as a repository for Transuranic waste from the U.S. Defense Programs, and is centered on a 16 sq. mile tract permanently withdrawn and owned by the U.S. Department of Energy (DOE). The facility has been open since the late 1980's, and has been receiving waste since 1998. Currently two of the planned eight waste panels have been mined—others will be mined as needed over the next 35 years. In addition to the underground workings, the WIPP includes a full complement of surface facilities for waste handling, laboratory and office space and maintenance facilities.

Currently the WIPP is host to a number of physics experiments being fielded by various organizations. It is also proposed as an ideal site for the UNO facility, given its lack of water, ease of construction and the existence of infrastructure owned and operated by the US Government.

5.3.1 Advantages and Disadvantages of the Site

The following are the principal advantages of siting UNO at the WIPP:

- The 650 m of rock overlying the repository absorbs most of the cosmic rays that continuously bombard Earth. Going to a deeper horizon would increase this shielding.

- The salt contains lower concentrations of naturally occurring radioactive elements than most rocks that compose the Earth's crust. The natural abundance of U/Th is typically 1/50 that found in rock. The abundance of airborne Rn is at the level of surface air, and can be reduced by about a factor of 30 by simply filtering the input air stream.

- The salt is dry, can be mined easily in nearly any cavity/drift configuration, and the cost of mining (approx. $20/m^3 based upon current costs at the site) is quite low.

- The WIPP is a federal project with a sophisticated infrastructure and work force, and will have a lifetime of at least 35 years. The scientific community will not have to bear the majority of the costs associated with maintenance and operation of the mine or available infrastructure; the science program will obviously have to cover its own expenses.

- Safety and mine rescue, training, ES&H, security, etc. already exist at the site, as do facilities for handling and maintaining mining equipment and materials

There has already been a large investment to support "underground science" in this facility. About 1.5 acres of space underground is now being refurbished with lighting and power installed throughout the area. This "north experimental area" is soon to be available to the science community. An Environmental Assessment concluded these projects can go forward without concern. There is also support for installation of some prototype projects that are described below.

The primary perceived disadvantage to the WIPP is the creep behavior of the host salt materials which lead to closure of any underground openings over time. However, the behavior of WIPP salt is well understood, and very predictable, so this behavior is viewed more as a design issue rather than a particular disadvantage. On the other hand the predictable nature of the closure, and the lack of sudden catastrophic failures in this material gives advantages in terms of cavity maintenance.

5.3.2 Conceptual Layout of an UNO Facility at the WIPP

Current concepts for UNO at WIPP call for the host cavity being sited either close to the WIPP horizon (at a depth of the order of 700 m), deeper at the base of the Salado (about 1100 m) or in the Castile (at depths down to 1300 m). Access to the facility would be developed by driving access drifts from the WIPP. In the event that a deep horizon was chosen, the access ramps would be supplemented by a raise from the WIPP level to the experimental level. If the deeper location was chosen it might also be necessary to provide a new shaft dedicated to the experiment leading directly to the UNO cavity area. This would allow for proper ventilation of the facility, and would provide the second egress and ingress points required by the mining regulations. For either the shallower or deeper options

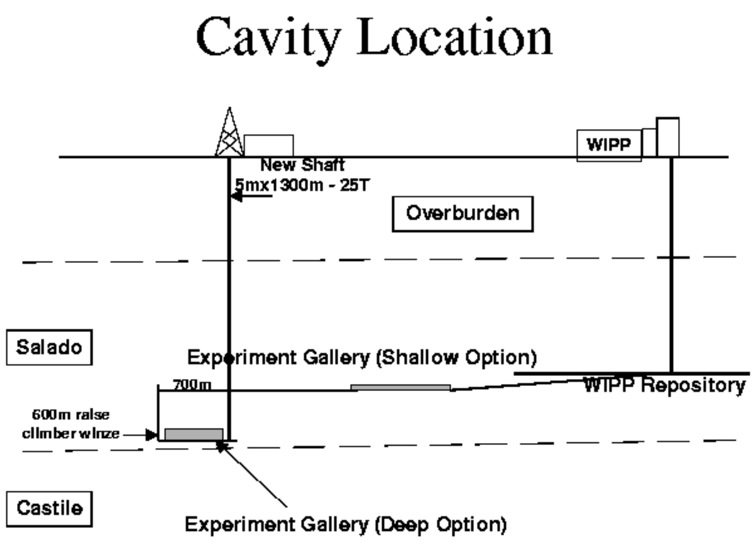

Figure 5.4: Conceptual layouts for the shallow and deep options for the UNO site.

an additional shaft would be of great value in handling the large quantities of salt needed to be mined for the UNO cavity, as well as providing easy access for experimenters during operation of the facility. Conceptual layouts for the shallow and deep options are shown in Figure 5.4.

The UNO cavity itself is conceptually a "mail-box" configuration, with the cavity being designed to contain a free-standing water containment structure 60m x 60m x 180m in dimension. The cavity would be oversized to accommodate creep closure of the salt roof, walls and floor, and the roof would be arched to provide stability and to allow ease of access to the containment structure. Ancillary cavities would be situated off the access drifts for water circulation and purification systems, ventilation, machine shops and data handling facilities.

5.3.3 Cavity Stability

Salt is a visco-plastic material, and openings in this material at depth close over time through creep deformation. Preliminary calculations indicate that a cavity at the WIPP level might close by several meters over the expected life of the experiment: at a deeper horizon the closure would be greater. To allow for this closure the cavity will be oversized, while overall closure will be reduced through the use of techniques such as pre-mining of the cavity.

This visco-plastic nature of salt has several advantages. Firstly the material tends to be quite stable over large spans, since unlike hard-rock the yield of the salt leads to a reduction in stresses, while the visco-plastic nature prevents fractures from existing which can lead to local instability and support problems, including unexpected failures and dangerous roof collapse. Finally the plasticity of salt makes it an easy material to mine, with continuous

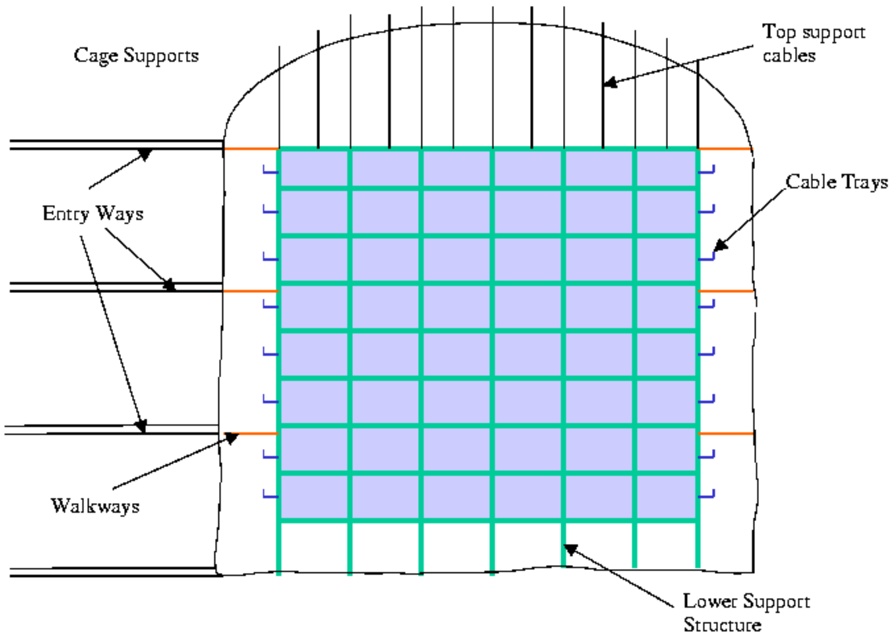

Figure 5.5: A sketch of the UNO containment structure.

miners being very efficient, and the use of more expensive drill and blast techniques not being required.

WIPP salt is probably one of the best understood rock materials due to the extensive research and laboratory and field measurement carried out in support of the waste disposal mission. Long-term prediction over the expected life of an underground experimental facility is feasible. The rate of closure of underground rooms is a function of the depth, the size and geometry of the rooms, and the overall local extraction ratio (the fraction of material mined out in the local vicinity). Rooms in producing mines, where extraction is optimized but long-term stability is not needed, are designed to close quickly. Special purpose openings, such as the planned UNO cavity, will be designed for slower closure by minimizing the extraction ratio and optimizing the geometry. Preliminary calculations have been performed on conceptual cavities at all likely depths, up to the deepest feasible location at 1300m. These show that with appropriate design, acceptable closures (in any case, $< 25\%$) can be achieved at the deep horizon over an expected design lifetime of 30 years.

5.3.4 Water Containment

As currently envisaged, the water containment structure would consist of a free-standing steel frame supporting a steel plate liner as shown in Figure 5.5. This liner would be bolted to the frame and sealed with gaskets: commercial feed-thru's would be inserted in each plate for the PMT power and signal lines as shown in Figure 5.6. The frame work would be supported on the bottom on a series of hydraulic mining props which would allow adjustment of the support

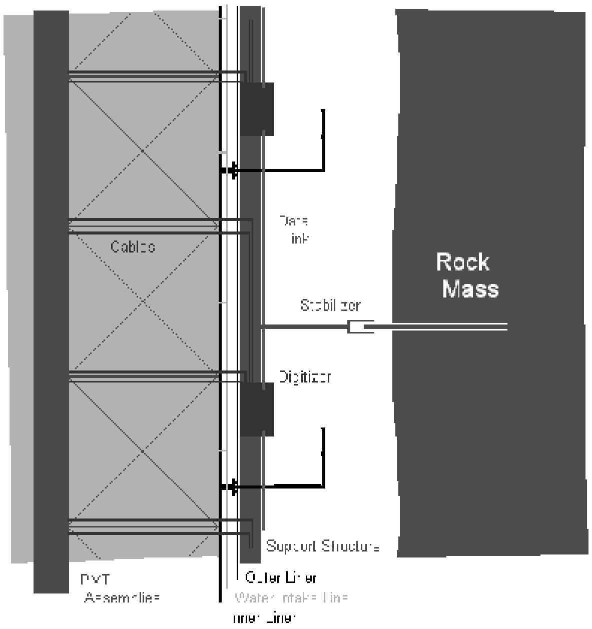

Figure 5.6: Side water containment structure.

to accommodate slow creep of the cavity floor as shown in Figure 5.7. Although the frame would be free-standing, friction braces would be used on the sides to provide additional "sway" support. The upper surface would allow access to the structure for maintenance, signal processing and calibration, and would be supported off the roof by cables.

The use of a free-standing structure (which could also be used in a hard-rock cavity) would have many advantages. Primary among these are the ability to have continuous access to the sides of the structure for maintenance, repair of any minor leaks, and updating of electronics and cables. The primary inner liner would be backed up by an outer liner made of either thin gage steel or geotextile which would act as a splash-guard in the event of minor leaks and a protective cover for the electronics.

PMTs would be mounted on pre-fabricated units which would be supported off the main containment frame using cables and braces and a conceptual sketch is shown in Figure 5.8. Buoyancy of the PMT units would be set to reduce loads on the supports either during operation, or in the event of emptying of the system being required. As noted above the PMTs would be connected electrically through a series of pre-fabricated pass-thrus into the external cable system. The water containment structure will be divided into three optically independent units, with internal PMT structures as appropriate.

5.3.5 Other Facilities

The WIPP is a working facility with all necessary mining, maintenance and support facilities available, including mine safety and rescue, security systems and computer capabilities. All

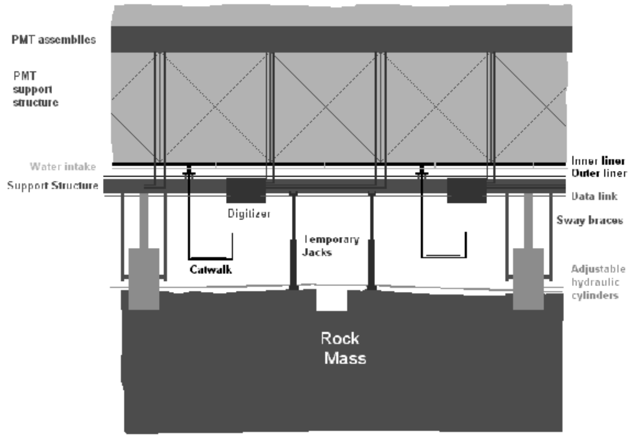

Figure 5.7: Bottom water containment structure.

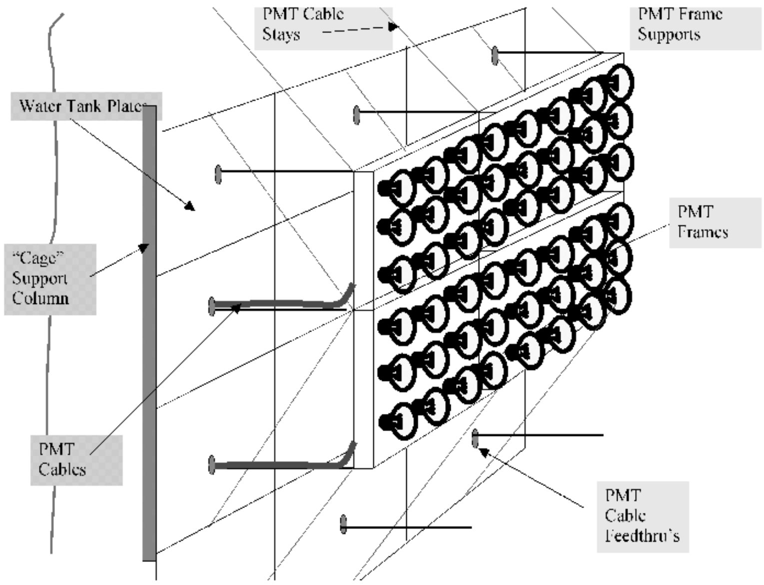

Figure 5.8: Mounting scheme of pre-fabricated PMT unit.

of these facilities would be available to the UNO collaboration as a basis for that facility. This being the case, a need for extensive buildings devoted to the science program on the surface at WIPP is not envisioned, and the ongoing safety, health and maintenance costs would be minimized by leveraging off the existing facilities. At most a few modest scale trailers (at least one of which is already available) might be needed to provide on-site space for example for detector operation and monitoring. It may also be useful to have space on the surface to store detector components before they are moved underground.

5.3.6 Costs

Any cost estimates made at this time are subject to considerable uncertainty since the design is still very conceptual. However some estimate of the order of magnitude of costs is of value in assessing the feasibility of the conceptual design. Our initial estimates for construction costs are based on mining costs of $7.25/tonne for simple access openings and for the detector cavity. This is a relatively firm cost based on actual experience at the WIPP and at local potash mines. For a 60m$\times$60m$\times$180m cavity close to the WIPP horizon the total tonnes mined would be of the order of 2.8 million tonnes for a cost for excavation and roof bolt support of the order of $33 million. As noted this is based on actual mining costs in the basin and as such is quite firm: we estimate it is within 25% of the final cost, and does include all mining outside of the current WIPP footprint, and includes mining: access entries, the detector cavity, and cavities for ancillary systems including water treatment, workshops, electrical alcoves and clean rooms, as well as: additional ventilation needs, and electrical subs.

In our opinion a new shaft will be required to expedite removal of mined material, and to provide additional access and ventilation. This shaft would add a cost of about $36 million, this being a reasonably firm cost based on recent detailed estimates for adding a waste shaft to the WIPP. This would include all fittings for the shaft, including power, hoist and internal furniture. Thus mining, access and basic ancillaries for a shallow (WIPP level) detector would be around $70 million. Costs for a deeper detector might be about $500,000 more for the access entries and ramps, and an additional $6 - $7 million for a deeper shaft, for a total cost of the order of $77 million.

Costs have also been estimated for the Water Tank and support structure as laid out in this section, but here it must be cautioned that the costs are more uncertain than for the mining. Based upon the conceptual design presented here, it is estimated that the tank and support structure would cost of the order of $50 million. This cost has been developed using the estimated weight of steel and a cost of $2,200 per tonne for material and fabrication. This cost per tonne is based on the standard estimating costs used in structural engineering in the US. It must be cautioned that this figure is very approximate, and no cost-saving design features have been included.

The order of magnitude costs for a detector chamber, access and water tank at the WIPP level are therefore estimated to be $120 million, with an additional cost of the order of $7 to $10 million for a deep detector. These costs include mining and rock support for all access entries and ramps, for the detector, and rooms and alcoves for all ancillary equipment, shaft sinking and outfitting, ventilation and power, and the construction of the water tank and support structure. They do not include the costs for PMTs, PMT support structure, radon removal systems, water treatment and pumping systems, cabling, or data acquisition. These items will add significant cost. However it should be noted in making comparisons that the costs for these items will be the same for the WIPP location, or for any other site, and will be the same for shallow or deep options.

5.4 Bibliography

[1] M.Spiro, "A low energy neutrino superbeam experiment", talk presented at the CERN Muon Plenary Week, May 7–10, 2001, see http://muonstoragerings.web.cern.ch/muonstoragerings/Events/20010507/spiro.pdf

Chapter 6

Detector R&D

6.1 Overview

The choice of the underground water Cherenkov detector technique for UNO minimizes the number of critical R&D items and allows the detector to be built within a reasonable time scale (about ten years) while keeping an excellent physics program. Thus, at this preproposal stage our R&D efforts are concentrated on a cost effective and structurally sound design for the detector. The main areas of the R&D work are:

- Cavity excavation,
- Water containment method,
- PMT mounting structure
- PMT
- New photodetectors
- Large scale magnets for neutrino factory applications

Mining techniques for large cavity excavation are well developed. However, because of the extraordinary size of the cavity needed for UNO, there must be detailed studies of the geological composition, mining feasibility, long term stability of the cavity and cost of the excavation. Since these issues strongly depend on the particular site geology, environment and existing infrastructure, there are independent studies for each candidate site. Some of the results from the studies are reported in the previous chapter.

The water containment method also depends somewhat on the characteristics of each candidate site. It appears that in a salt rock environment it will be difficult to have a water containment system that utilizes the rock surface because of the creep of the rock and the possibility of a water leak which will damage the rock surface. However, our initial study shows that a free standing containment system using commercially available components and methods is possible. This was described in the previous chapter. In a hard rock environment, it may be possible to utilize the same water containment method used for SNO and KamLAND where the hard rock surface was sprayed with MineGard (produced by Urylon) for a water and radon seal after proper treatment of the rock surface. This is potentially a very inexpensive solution, but the lifetime of the containment system needs to be evaluated carefully so that it will be guaranteed to last for a minimum of 30 years. A technique similar to that used by Super-Kamiokande which employs a stainless steel water tank back filled with concrete can be also used in hard rock environment.

We also have begun to look into various PMT mounting systems. With our experience with the IMB, Kamiokande and Super-Kamiokande detectors, we do not foresee any major difficulties, however, we are seeking cost effective ways to mount PMTs.

The cost of PMTs comprises about 30% to 40% of the total detector costs. For the UNO baseline design we will need about 56,000 20" PMTs and 15,000 8" PMTs. The initial quote from Hamamatsu company is $2,775 per 20" PMT and $1,200 per 8" PMT assuming an 8 year delivery time. This cost includes a $50/PMT transportation cost and a 100 m cable cost. We assumed an exchange rate of $1.00 = 100 yen. It is possible to shorten the delivery time, but that will incur additional costs (few hundred dollars/PMT). In the following sections, we discuss R&D on PMT and other photo-detectors in order to explore possibility of lowering PMT costs and/or improving photo detection efficiency, timing etc.

All of the above work requires engineering expertise, and thus it is necessary for us to hire independent consultants. We are looking into various ways to secure funding for this work (such as Japan-US Cooperative Research Grant) in collaboration with the Hyper-Kamiokande working group in Japan, and to collaborate with interested engineers in national laboratories and universities.

6.2 PMT R&D

The performance of the 20" diameter PMTs used in Super-Kamiokande is certainly excellent and is good enough for the physics goals of UNO. So, we concentrate most of our effort on PMT R&D on the cost reduction aspect. One possibility of cost reduction is to make larger PMTs than Super-Kamiokande 20" PMTs. Based on the comparison of the 8" PMT and 20" PMT costs, we can assume that the PMT cost increases approximately linearly with the diameter of the PMT while the photocathode coverage increases quadratically with the diameter. Thus, by making larger PMTs we may be able to reduce the PMT cost while maintaining the same photocathode coverage. Then, the next obvious question is what is the largest PMT size we can make with the current technology. Our initial probe to this question yielded that it appears to be possible to make 30" PMTs, but there appears to be some difficulties of making 40" glass bulbs at this time.

Another area of PMT R&D can be done on improving the PMT glass manufacturing process. Currently the glass bulbs are manufactured by manual blowing. This should be changed to automatic mechanical procedure.

If the above R&D is realized, potentially we will have about 30% reduction in the PMT costs (about \$50M in savings). We can also consider using 20" or larger PMTs for the outer detector (veto) region rather than 8" PMTs as assumed in the baseline design. While this will require a detailed MC simulation study, it has a potential of about \$10M in savings.

There are, however, potential drawbacks of using larger PMTs. They are: loss of granuality, and degradation in the photon position and timing resolutions. The exact effect of these possible degradations in the PMT performance on physics capability of UNO needs to be evaluated using detailed detector simulations. And such a study is being carried out presently. A possible option to avoid such degradations in the larger PMTs is to design a multi-anode (possibly 4 channels) structure which can effectively gain back the lost granuality, photon position and timing resolutions. We are discussing these possiblities with PMT manufacturers.

6.3 New Photo-detector R&D: The Novel Photo-sensor ReFerence

The key element of the UNO experiment is efficient Cherenkov photon detection. High quantum efficiency (e.g. twice higher than PMTs), single-photon sensitivity, single-photon resolution, excellent time resolution, extremely low thermionic noise, very low sensitivity to magnetic fields, intrinsic angular sensitivity, small dead area, conceptual simplicity, low cost, and the possibility of industrial mass production, are the key features of an ideal, previously nonexistent photo-sensor.

The novel photo-sensor concept ReFerence [6, 7, 8, 9] presents a long awaited breakthrough in this field. It enables photocathodes to operate in reflection mode, for the first time without any adverse effects, which grants many important advantages over the PMT technology. The ReFerence photo-sensor should in fact comprise all the features of the hypothetical photo-sensor presented above, as argued in the following subsection.

Particularly important for UNO, the ReFerence photo-sensor will offer the following unique features:

- Very high quantum efficiency (more than 50%) with simultaneous single-photon resolution.
- Diminished thermionic noise, thanks to the physical decoupling of the photocathode from the environment (water in UNO), and its active cooling.
- Single-photon color sensitivity without destructive filtering—a unique feature introduced by the novel TransReFerence configuration that will allow precise tracking through the time-of-flight measurements of Cherenkov photons of different wavelengths, and in addition it will extend the range of spectral sensitivity.
- Uniquely efficient protection against stray magnetic fields.

- Intrinsic angular resolution (without mirrors or lenses), which offers precise particle tracking.
- New production technique that will allow inexpensive industrial mass production of large-area multi-pixel panels.

The basic principle of the ReFerence photo-sensor is described in the following subsection. Some expected benefits for the UNO project are discussed, and finally our R&D efforts are summarized.

6.3.1 ReFerence Concept

Classical PMTs, the present photo-sensor choice in the majority of high-energy physics projects, in general combine affordable (though high) cost with good timing properties, but still with two very important drawbacks: the poor single-photon resolution and the low quantum efficiency. Hybrid Photon Detectors (HPDs) comprise excellent single-photon resolution, thanks to the electron signal amplification in a semiconductor sensor, but fail to offer higher quantum efficiency, since they have mostly been based on the same photocathode materials as PMTs. The exceptions are the two small-sized HPDs by Intevac [10] and Hamamatsu [11] based on GaAsP photocathodes grown in the expensive Molecular Beam Epitaxy process. These photo-sensors offer peak quantum efficiency of almost 50%, but at an extremely high cost. The novel photo-sensor concept ReFerence offers a possibility to use a photocathode in the so-called reflection mode, instead in the traditional transmission mode. Reflection photocathodes provide much higher quantum efficiency with the same photocathode material, as elaborated in more detail below. Equally important, they are much simpler and cheaper to produce.

In reflection-type photocathodes the electrons are emitted through the same surface the photons have entered. The majority of the electron-hole pairs is created very close to the photon entrance surface (the Lambert- Beer exponential law) and therefore has high chance of reaching the same surface and escaping through it into vacuum. As a consequence, reflection photocathodes offer quantum efficiency nearly twice that of transmission photocathodes [12]. The sensitivity to UV light is enhanced even much more, since the short wavelength photons are absorbed closer to the surface.

Apart from a considerable increase in quantum efficiency and an important widening of the spectral response into the short wavelength range, reflection photocathodes offer also other very important advantages. The most important one is the significant simplification of the photocathode manufacturing process, and a consequent price reduction. The production of a reflection-type III-V photocathode (like GaAs, GaAsP, InGaAs and others) is much simpler than that of transmission phtocathodes since there is no need to fuse the grown photocathode structure with the glass window and to remove the growth substrate. This leads to a very significant cost reduction that is likely to bring the III-V photocathodes into an affordable price range, with unprecedented high quantum efficiency (for GaAsP about three times higher than of traditional transmission bialkali photocathodes). Reflection photocathodes may even benefit from the conductive layer underneath, since it may serve as a mirror reflecting transmitted light back through the photocathode layer, providing thus the photon with another conversion chance.

6.3.2 The ReFerence Photo-sensor

ReFerence phototube is based on the recent discovery that a Winston cone, which provides the most efficient non-imaging light concentration in one direction [13, 14], may simultaneously act as an ideal focusing electron lens in the opposite direction. In most general terms, the ReFerence phototube, shown in Figure 6.1, is a Compound Parabolic light Concentrator (CPC) or Winston cone [13, 14] which concentrates all the light entering the cone from the left side through the entrance aperture (2), at an incidence angle smaller than a given design cutoff angle (30 degrees in Figure 6.1), to the light collection surface (3) covered by a reflection photocathode (6), and simultaneously focuses and accelerates photoelectrons (7) emerging from the photocathode in the opposite direction, onto a point-like electron sensor (8) placed in the middle of the entrance aperture. This electron sensor may be a P-i-N diode, an Avalanche Photo Diode (APD), or any other suitable sensor. It is enclosed in a positive-ion feedback protection electrode (10) [1]-[5].

While the light concentration is provided by the tube shape that assumes a standard Winston cone mirror (4) and (5), electron focusing is facilitated by the electron lens formed from the electrodes that follow the same Winston cone shape, but with the insertion of a single narrow non-conductive gap (9) that divides the cone into two electrodes (4) and (5). The existence and the position of this gap are of crucial importance for the functionality of the ReFerence photo-sensor. Electrodes (4) and (5) have to be kept at different electric potentials: U4 and U5. From electron optics simulations it follows that a correct electron focusing may be achieved with a continuous multitude of combinations of U4 and U5.

The example presented in Figure 6.1 is optimized for a cutoff incidence angle of 30 degrees. Equivalent results may be achieved also with other acceptance angles, ranging approximately between 10 and 50 degrees. Further, the example in Figure 6.1 provides a theoretical maximum light concentration factor (factor 2 in diameter and 4 in area) for the accepted light with incidence angle smaller than 30 degrees, and the angular spread at the collection surface being maximal, i.e. 90 degrees [13, 14]. The ReFerence tube concept is not limited to CPCs with maximum concentration and may be practiced equivalently with CPCs of a lower concentration factor and a narrower angular spread of light at the collection surface [9]. That may be of certain advantage in avoiding light reflections from the photocathode surface, but inevitably leads to the increase of the photocathode surface.

Of particular importance for the UNO project is the unique feature of ReFerence to diminish thermionic noise, thanks to the fact that the photocathode is not in thermal contact with the water and may be cooled in vacuum to very low temperatures, e.g. by Peltier cells. Thermionic electron emission rises nearly exponentially with the photocathode temperature, and at a temperature of around 35 C reaches very high levels, which may be hardly tolerable in an experiment devoted to the study of very weak or rare phenomena, like solar neutrinos,

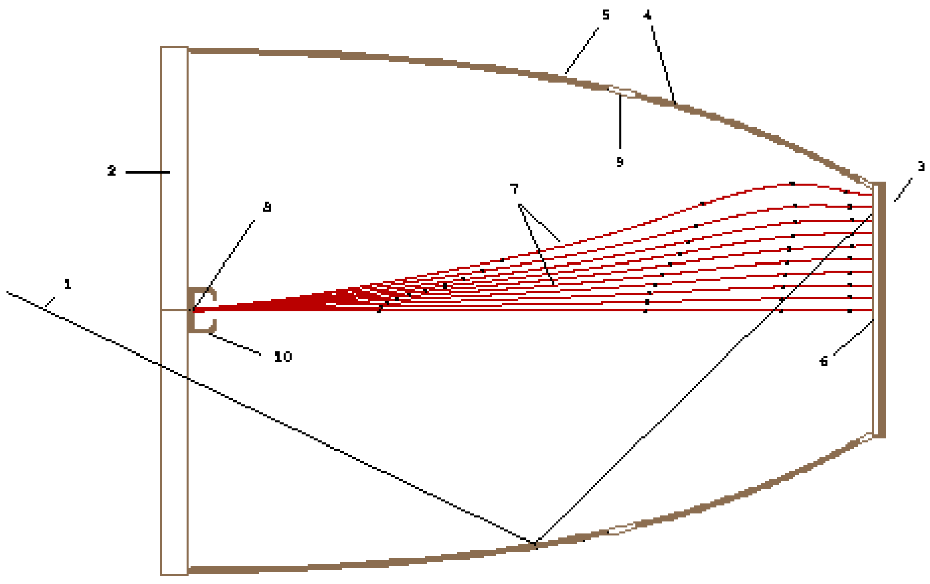

Figure 6.1: ReFerence photo-sensor presents an ideal light concentrator (Winston cone), from left to right, and at the same time an optimal point-focusing electron lens in the opposite direction. Electron trajectories are shown as emerging from the reflection photocathode on the right side and reaching a small electron sensor in the middle of the entrance window.

or the proton decay.

Uniquely efficient shielding against external magnetic fields may be applied to a ReFerence phototube. In contrast to PMTs and other transmission photocathode devices, in ReFerence the electron velocities are highest in the vicinity of the entrance window, and lowest at the opposite side, where they are well protected by the shield. The electrons are therefore less sensitive to magnetic deflection, and there is no need for a magnetic shield to extend beyond the front window, which used to lead to the important acceptance-shadowing problems with PMTs in many applications. Moreover, the magnetic shield, in a form of cylinder or a cone may be completely closed behind the photocathode, providing thus an unprecedented efficient magnetic shielding. This feature is very important for the UNO project, not only because of the need to screen the geomagnetic field, but even more because certain considered UNO configurations require relatively strong magnetic fields for momentum analysis and charge identification.

6.3.3 Outline of the ReFerence Prototype Development

The construction of the ReFerence prototype is already under way at UC Davis, and the plan is to construct an entire prototype family in order to explore all the important design variations. The ultimate goal of this effort is to develop technology for inexpensive mass production of flat large-area multi-pixel panels.

The targets for the prototype development are: (1) Design of the photocathode cooling system, (2) Color sensitivity without destructive filtering, (3) Optical CPC Reflector, (4) Development and implementation of new super-sensitive reflection-mode photocathodes, (5) Coulomb back-scattering of electrons from the silicon sensor, (6) Electron multiplication, gain and time resolution, and (7) Parallel studies of other promising concepts.

6.4 Large External Magnet Systems for the UNO Detector

The possibility of using UNO as the far detector for a long-baseline neutrino oscillation experiment, in conjunction with a future muon storage ring (neutrino factory) has been discussed in Section 4.3.3. To fully exploit the potential of the neutrino factory, UNO must be able to distinguish the charge of high-energy μ^+ and μ^-. This capability would require adding one or more large magnet systems to the detector as shown in Figure 6.2 and Figure 6.3.

These magnets could be either solenoidal or toroidal. A preliminary study of the solenoidal design has been carried out [16] and is described below in some detail.

The magnet system must produce a magnetic field of approximately 0.1 T transverse to the neutrino beam direction. The field should be moderately uniform over a large volume, approximately $40\,\mathrm{m}\times 40\,\mathrm{m}$ transverse to the beam and 5 m along the beam direction. Outside the magnet volume, it is critical to limit the magnetic field to a level at or below that of the Earth (approximately 50 mT). A solenoidal design that addresses these requirements is shown in Figure 6.4. It has an interior volume of $5 \times 40 \times 40\,\mathrm{m}^3$ and single-layer winding with just over 3.4 MA-turns.

A straightforward construction option for this solenoid would use turns constructed of standard aluminum bus-bar stock, $300 \times 20\,\mathrm{mm}^2$, welded end to end. Turns would be constructed in a simple configuration with right-angle bends at the corners. Transitions between turns would be accomplished by the insertion of bars with pre-bent joggles as shown in a close-up, detailed view of a portion of the winding in Figure 6.5. The turn spacing is 70 mm (50-mm gaps) and the nominal operating current is 6 kA for a conductor current density of 1 A/mm^2, a level that is quite reasonable for cooling by natural convection in ambient air. Each face of the solenoid is approximately 71% open. The stored energy of the solenoid at full field is approximately 32 MJ and the power requirement is approximately 140 kW. Approximately 860 metric tons of aluminum bus bar would be required for the winding.

The large, flat sides of this solenoid experience appreciable magnetic pressure, approxi-

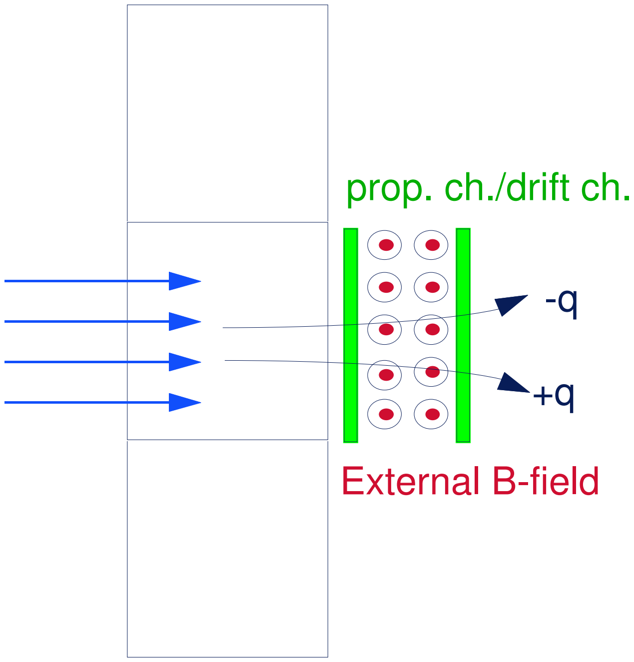

Figure 6.2: Conceptual layout of UNO as a far detector for a neutrino factory beam: External Magnet Option

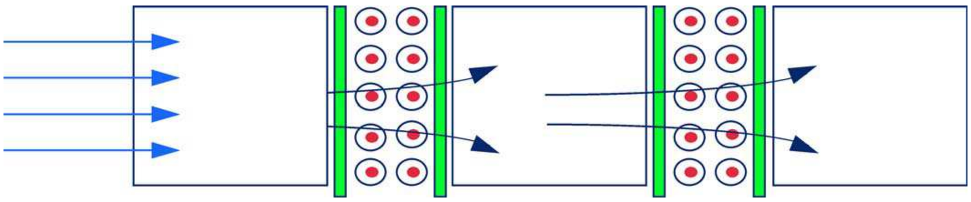

Figure 6.3: Conceptual layout of UNO as a far detector for a neutrino factory beam: Inter-Module Magnet Option

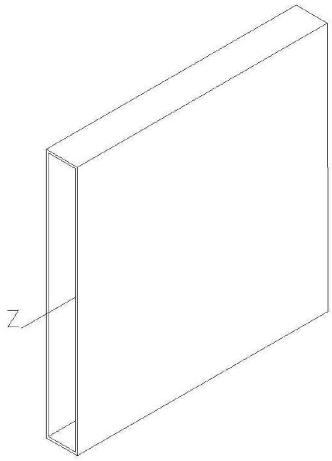

Figure 6.4: Solenoid geometry, z-axis transverse to beam, $5 \times 40 \times 40\,\mathrm{m}^3$ interior volume.

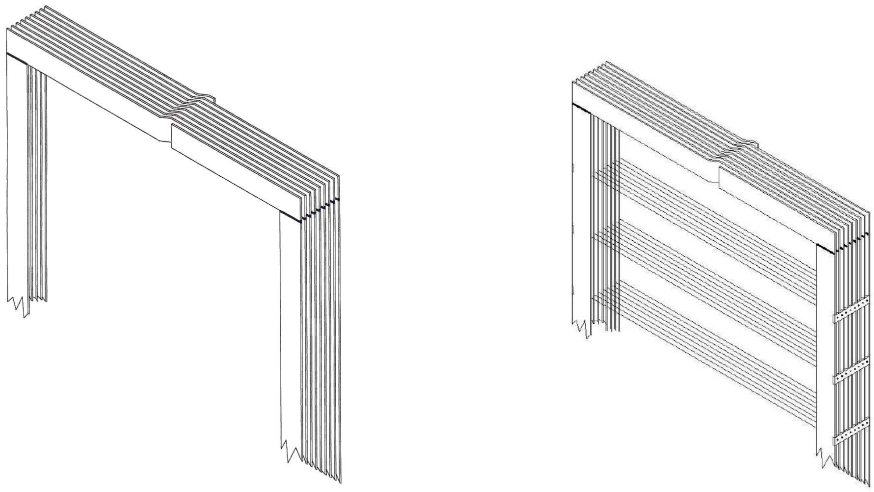

Figure 6.5: The right view is a close-up of windings showing separation of turns and turn-to-turn transitions. The right view is a portion of the windings showing the installation of horizontal guy wires to control outward deflection of turns at full field.

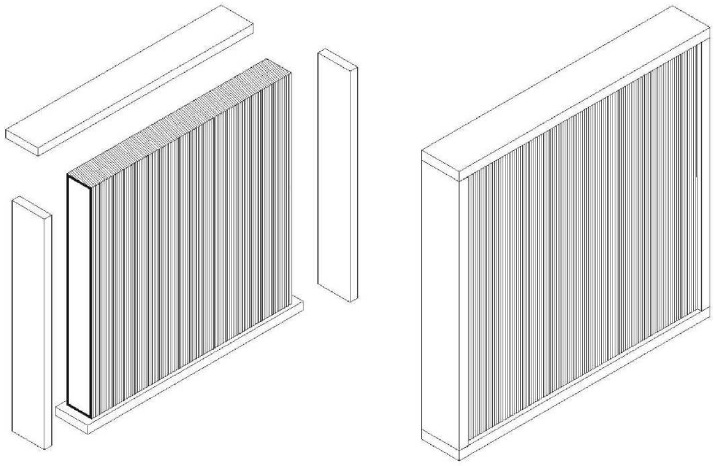

Figure 6.6: Exploded and normal view of the solenoid with iron end caps and flux-return bars for suppressing stray field outside the solenoid.

mately 4 kPa, which translates to a nearly uniform running load of approximately 280 N/m on the straight legs of the solenoid turns. If these turns have no additional support: the shear and membrane stresses are very small, the bending stresses in the long, vertical legs are appreciable (though manageable), but the deflections of these sections are huge -0.6 to 3.0 m by simple estimates, depending on how the end supports are modeled. Therefore, some means of additional support for the turns will be required. An option is illustrated in Figure 6.5. Using 43, 2-mm diameter, stainless-steel guy wires per turn (39 horizontal plus 4 vertical) deflections are controlled with only a modest 100 MPa (estimated maximum) added to the lightly pre-tensioned wires.

A simple option to reduce stray field outside the solenoid is to add iron end caps and flux-return bars along the narrow, top and bottom edges of the turns as shown in Figure 6.6. In this configuration, the iron does not add to the obstruction in the beam direction. With a total flux in the solenoid of approximately 20 Wb, an estimated thickness for both the end caps and bars is 1.2 to 1.3 m for full saturation of the iron. This simple geometry is moderately effective in reducing the stray field as shown in the contour plots of B_z in Figure 6.7. These show the field levels at distances of 5, 8, and 10 m from the center of the solenoid in the beam direction. Contours with magnitude greater than 100 mT (twice the Earth's field) have been suppressed for clarity. As yet, no detailed study of shaping or positioning the iron components for further reductions has been carried out, but the results displayed in Figure 6.7 are encouraging that a region near the solenoid with acceptably low field can be produced. The presence of the iron end caps and flux-return bars also improves uniformity of the field within the solenoid as can be seen in the plots of Figure 6.8. There is also a modest enhancement of the interior field, which is also obvious in the Figure.

Although very large, the system described here is quite simple and there is a manufacturing-experience base for the materials, components and subsystems assumed in this conceptual

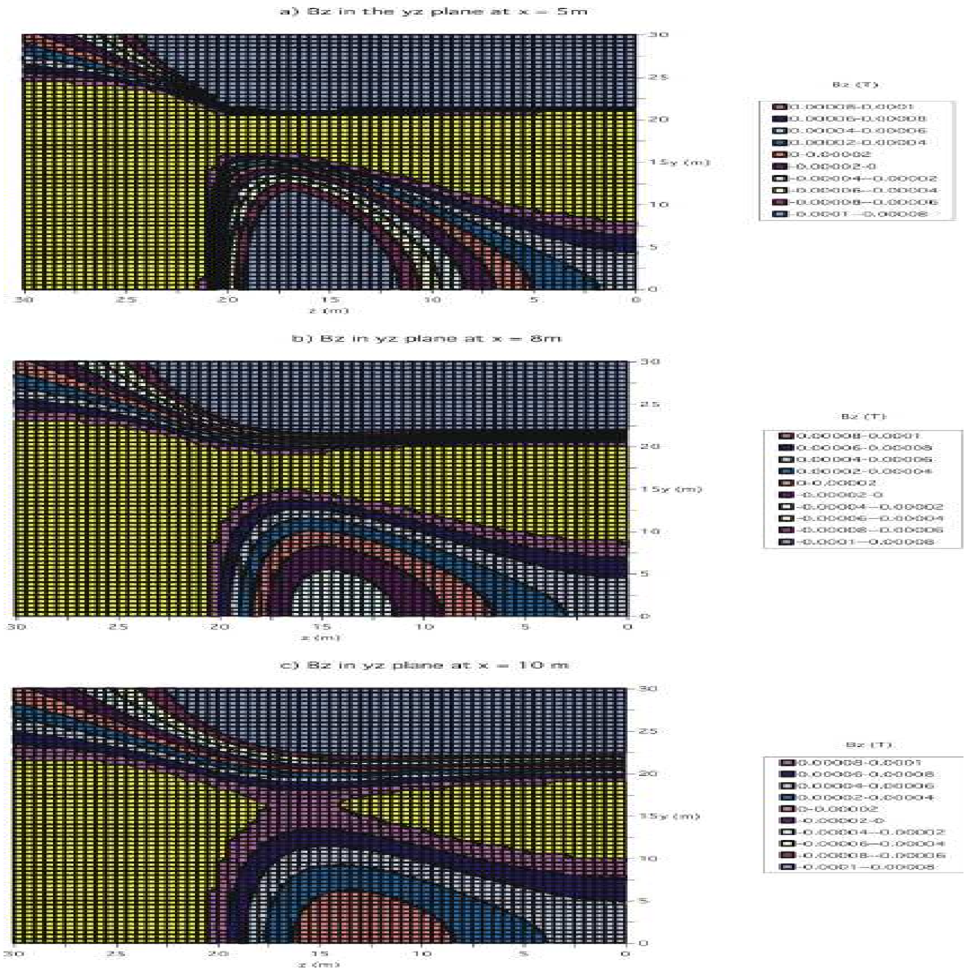

Figure 6.7: Contours of the axial component of field at distances of a) 5 m, b) 8 m, and c) 10 m from the solenoid axis in the direction of the neutrino beam.

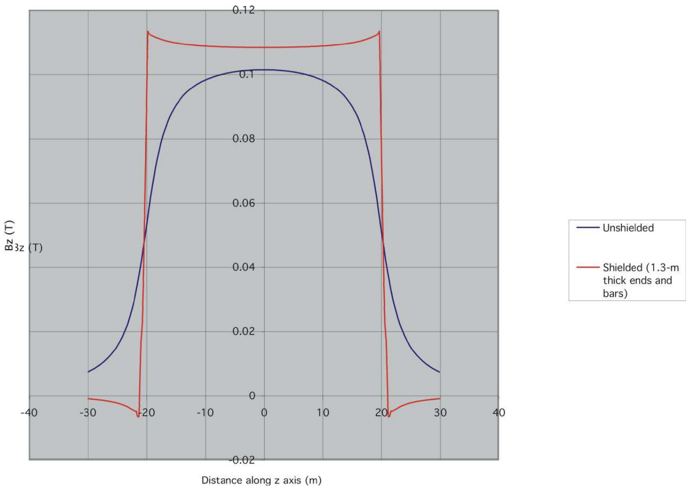

Figure 6.8: Plots of field on axis with and without iron end caps and flux-return bars (1.3 m in thickness for this case).

Materials and components			**14,008 k$**
Material	Weight (tons)	Unit price	Cost
Shielding iron	9,211	1$/kg	9,211 k$
Aluminum busbar	859	5$/kg	4,296 k$
Structural steel	5	25$/kg	127 k$
Insulation	37	10$/kg	373 k$
Power system			**113 k$**
Item	Power and current	Unit price	Cost
Power supply	137 kW	200$/kW	27 k$
Cooling system	137 kW	200$/kW	27 k$
I&C			50 k$
Buswork	360 kA-m	24$/kA-m	9 k$
Design			**2,824 k$**
Assembly			**2,824 k$**
Grand total			**19,770 k$**

Table 6.1: Estimate of magnet system cost with breakdown by materials/components and subsystem.

design. Therefore, the overall system cost can be reasonably estimated from a summation of typical costs for these including value added for adaptation to the present design. These are provided in Table 6.1, broken down by appropriate quantities and rates. Estimates for design and assembly of the system are included as simple fractions (20%) of the sum of other costs. Not included in Table 6.1 are such items as site preparation, transportation of the magnet to the site, or the possible construction of a magnet-fabrication facility near the site. These are potentially costly issues that will have to be decided as a detailed magnet design is carried forward. In conclusion, a magnet system meeting the requirements for the UNO detector appears to be feasible, although there are structural issues that will have to be dealt with in the detailed design. These include a means of support for approximately 9000 t of shielding iron against both gravitational and magnetic loads and provisions for stabilizing a structure that is very tall and thin and installed on its narrow edge. Magnetic shielding also remains an issue, although there is potential for a simple solution through careful design of iron end caps and flux-return bars.

6.5 Bibliography

[1] Daniel Ferenc, New developments in Hybrid Photon Detectors. Presented at New Detectors, Erice, Trapani, Sicily, Italy. November 1–7, 1997. World Scientific 1999, p. 131–140, Editors C. Williams and T. Ypsilantis.

[2] D. Ferenc, Imaging Hybrid Photon Detectors with Minimized Dead Area and Protection Against Positive Ion Feedback. Nucl.Instrum.Meth. **A431** (1999) 460–475.

[3] D. Ferenc, D. Hrupec and E. Lorenz. Solution to the Ion Feedback Problem in Hybrid Photon Detectors and Photomultiplier Tubes. Nucl.Instrum.Meth. **A427** (1999) 518–523.

[4] D. Ferenc, E. Lorenz, R. Mirzoyan. A "LEGO" Hybrid Photon Detector— assembled from standard mass-produced vacuum components. Nucl. Instr. Meth. **A442** (2000) 124–127.

[5] D. Ferenc. Imaging Hybrid Photon Detectors with a Reflective Photocathode. Nucl. Instr. Meth. **A442** (2000) 150–153.

[6] Daniel Ferenc, Patent Application, UC Case /No. 2000–466.

[7] Daniel Ferenc, A Novel Photo-sensor Concept, Presented at the Conference Imaging 2000, Stockholm, June 28 July 2, 2000. To appear in Nucl. Instr. Meth. A.

[8] Daniel Ferenc, A new concept of HPD with reflective photocathode, presented at the IEEE Conference, Nuclear Science Symposium and Medical Imaging Conference, in Lyon, France, October 2000.

[9] D. Ferenc, The ReFerence Photo-sensor, to appear in Nucl. Instr. Meth. A.

[10] Intevac, US Patent-US5374826: Hybrid photomultiplier tube with high sensitivity.

[11] R. Mirzoyan, D. Ferenc and E. Lorenz. An Evaluation of the New Compact Hybrid Photodiodes R7110U-07/40 from Hamamatsu in High-Speed Light Detection Mode. Nucl. Instr. Meth. **A442** (2000) 140–145.

[12] Silvano Donati, Photodetectors, Prentice Hall PTR, 2000.

[13] W.T. Welford and R. Winston, The optics of Nonimaging Concentrators, Academic Press 1978.

[14] R. Winston, J. Opt. Soc. Amer. **60** (1970) 245–247.

[15] M.F. Weber et al., The 3M Film/light Management Technology Center, Giant Birefringent Optics in Multilayer Polymer Mirrors, Science Vol.287 No.5462 (2000) 2451.

[16] This work is carried out by J. Miller, J. Toth, and S. Prestemon at the National High Magnetic Field Laboratory, Tallahassee, Florida